**JÜLICH** FORSCHUNGSZENTRUM

**Final Report**

# Technical assistance for the deployment of an advanced hyperspectral imaging sensor during

# FLEX-EU
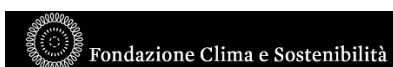
**ESA Contract No. 4000107143/12/NL/FF/If**

Issue 2 – Revision 2

26 September 2017

*Final version*

imaa Consiglio Nazionale delle Ricerche
Istituto di Metodologie per l'Analisi Ambientale

University of Zurich UZH

UNIVERSITÀ DEGLI STUDI DI MILANO BICOCCA

CzechGlobe

Fondazione Clima e Sostenibilità

Uniwersytet Przyrodniczy w Poznaniu
Poznań University of Life Sciences

**Table of Content**

**Acronyms and Abbreviations**

| | |
|---|---|
| CCN | Contract Change Notice |
| DAR | Data Acquisition Report |
| DAT | Days after treatment |
| DEM | Digital Elevation Model |
| ESA | European Space Agency |
| ESTEC | ESA Technical Centre |
| ETR | Electron Transport Rate |
| $F_{687}$ | Fluorescence at 687 nm |
| $F_{760}$ | Fluorescence at 760 nm |
| Fc | Fractional covers |
| FLEX | FLuorescence EXplorer |
| FOV | Field-of-View |
| FWHM | Full Width at Half Maximum |
| G | Ground flux |
| GPP | Gross Primary Productivity |
| H | Sensible heat flux |
| HYFLEX | HYperspectral FLuorescence EXperiment |
| *HyPlant* | Hyperspectral Plant imaging spectrometer |
| iFLD | Improved Fraunhofer Line Discrimination |
| LE | Latent heat flux |
| LUE | Light Use Efficiency |
| MERIS | Medium Resolution Imaging Spectrometer |
| MTCI | MERIS Terrestrial Chlorophyll Index |
| NDVI | Normalized Difference Vegetation Index |
| NEE | Net Ecosystem Exchange |
| NIR | Near Infrared (spectral range) |
| APAR | Absorbed Photosynthetic Active Radiation |
| PRI | Photochemical Reflectance Index |
| PSF | Point Spread Function |
| Reco | Ecosystem Respriration |
| ROI | Region of Interest |
| SFM | Spectral Fitting Method |
| SVD | Singular Vector Decomposition |
| SWIR | Short Wave Infrared |
| TOC | Top-Of-Canopy |
| u* | Friction velocity |
| VI | Vegetation Indices |
| VIS | Visible (spectral range) |
| WP | Workpackage |
| $APAR_{chl}$ | radiation that is absorbed in green, photosynthetically active plant tissue |

**Reference Documents (RD)**

[RD-1]  ESA, 2015: Report for Mission Selection: FLEX, ESA SP-1330/2, European Space Agency, Noordwijk, The Netherlands.

[RD-2]  EOP-PI/2008-05-83, An analysis of the synergy between FLEX and Sentinel-3.

[RD-3]  FLEX/S3 Tandem Mission Photosynthesis Study, Final Report, ESA ESTEC ITT AO/1-7088/12/NL/AF, July 2014.

[RD-4]  FLEX/Sentinel-3 Tandem Mission FLEX Bridge Study, Final Report, ESA ESTEC Contract No. 4000112341/14/NL/FF/gp, January 2016.

[RD-5]  HYFLEX Final Report, ESA Contr. No. 4000107143/12/NL/FF/If, issue 8, 19 April 2014.

[RD-6]  FLEX-EU Data Acquisition Report (DAR), ESA Contr. No. 4000107143/12/NL/FF/If (CCN2), issue 1, 29 March 2015.

[RD-7]  FLEX-US Final Report, ESA Contract No. 4000109199/13/NL/FF/lf, (Technical Assistance for the Deployment of the Airborne HyPlant Imaging Spectrometer during 2013 ESA/NASA Joint FLEX-US (FLuorescence EXplorer experiment in USA) Campaign, September 2016.

# 1 Summary of main findings

## 1.1 The FLEX airborne demonstrator *HyPlant*: A high-performance imaging spectrometer to measure reflectance and sun-induced fluorescence

The *HyPlant* sensor showed a good and reliable technical performance throughout the whole measurement period. For both modules (DUAL and FLUO module), the most recent calibration files acquired in spring 2014 were applied for the data pre-processing, including the Point Spread Function (PSF) deconvolution of the FLUO module data.

## 1.2 Mapping of study sites – building a continuous data set to understand the spatio-temporal variations of fluorescence across ecosystems

Two experimental sites, the forest area of Bílý Kříž (Czech Republic) and the agricultural, anthopogenical influenced sites around Jülich (Germany), were mapped with the *HyPlant* sensor for the second and third year, respectively. Those maps are part of a continuous data set to better understand the spatio-temporal variations of fluorescence across ecosystems. The maps of red and far-red fluorescence were calculated with the most recent, improved Fraunhofer Line Discrimination (iFLD) method for the agricultural sites, while the forest maps were calculated using the Singular Vector Decomposition (SVD) method. Additionally, a set of classic vegetation indices were calculated from atmospherically corrected reflectance data.

## 1.3 Relationship between fluorescence signal and fractional soil / vegetation cover

A 'mixed pixel experiment' was designed to investigate the role of fractional cover on the fluorescence signal using experimental data collected with *HyPlant.* The results of this experiment indicated that the far-red fluorescence signal scales linearly with vegetation fractional cover. Moreover, we demonstrated that a simple unmixing model, with two classes, is suitable to model fluorescence in mixed pixels. These results may have implications for large-scale mapping in the context of the FLEX mission.

## 1.4 Better understanding of the relationship between fluorescence, photosynthetic energy dissipation, and canopy gas exchange

Photosynthetic energy dissipation was altered by applying two physical and two chemical agents on a homogeneous grassland (turf) site:

i) A highly reflective powder (Kaolin) was used to reduce the absorbed Photosynthetic Active Radiation (APAR) by increasing leaf surface reflectance. This simulates the building of reflective leaf substances that is known to be an ecological acclimation to high light conditions. The expected changes in reflectance signal in the spectral range of the APAR was clearly detectable in canopy reflectance. However, the reduced APAR only led to the expected reduction in the red fluorescence. The far-red fluorescence signal cannot be interpreted due to the signal's the high dependence on the changed reflectivity of the vegetation surface.

1. An anti-transpirant agent (Vapor Gard) was used to produce a waxy layer on the leaves that sealed stomata and as consequence reduced transpiration. The treatment simulates the stomatal closure during drought periods. Chamber gas-exchange measurements revealed a reduction of $CO_2$ uptake and transpiration a day after the Vapor Gard treatment, proving the closure of the stomata. Ground and airborne fluorescence measurements revealed a slight but measurable reduction of the far-red fluorescence signal due to the reduced photosynthetic activity the day after the treatment.

ii) Two chemical agents were applied to block electron transport at photosystem I (Paraquat) and at photosystem II (Dicuran). Both treatments should result in an immediate and great increase of the fluorescence signal due to the limited electron transport of the photosystems.

Unfortunately, the Paraquat treatment proved to be too severe, and hours after application clear signs of destruction of the photosynthetic machinery occurred. No clear dynamics of the fluorescence emission could be derived from this experiment

iii) The experiment with Dicuran was very successful. A reduction of the electron transport at photosystem II resulted in a great increase of fluorescence emission (more than twofold). This increase was reproducibly detectable from ground an airborne measurements. The increase in fluorescence was coupled to a decrease in photosynthetic $CO_2$ uptake rate. Different doses of Dicuran were applied to investigate quantitatively the relationship between photosynthetic electron transport rate and intensity of the fluorescence emission. For all doses, an increase of fluorescence was detected; however, the increase of the absolute fluorescence signal was not directly (linearly) related to the doses of the application. Fluorescence measurements from the ground could reveal that areas treated with lower doses recovered faster than areas treated with higher doses. This result could not be confirmed from the airborne measurements.

## 1.5 How to include fluorescence into models – first recommendations towards a mechanistic modelling framework

We use the conceptual model that is presented in the FLEX report for mission selection and that was used in different publications (Drusch *et al*. 2016). In this model we can clearly separate two steps: (i) a part driven by light absorption and light reaction that is mainly governed by the biophysical properties of the canopy and the efficiency of the photosynthetic electron transport; and (ii) a biochemical part that is mainly driven by the efficiency of carbon fixation, i.e. the efficiency of the biochemical fixing of the enzyme RUBISCO.

We proposed a conceptual framework how FLEX measurements can be used to conceive such a forward model. The forward modelling of the canopy electron transport rate is in in an initial state but should be feasible, whereas for modelling canopy $CO_2$, uptake rates and GPP are more advanced and have already been proposed in former studies, such as the FLEX/S3 Tandem Mission Photosynthesis Study.

## 1.6  Relationship tree age and fluorescence

We combined three data sets to better understand the relationship between tree age and fluorescence emission: (i) mapping data from Bílý Kříž (Czech Republic) 2012; (ii) mapping data from Bílý Kříž 2014; and (iii) mapping data from Parker Track forest (USA) 2013. The analysis showed that data quality was best in the 2013 Parker Track data (managed Loblolly pine forest) and thus an analysis of the relationship between tree age and fluorescence emission was conducted on these data.

It could be shown that red fluorescence diminished with stand age, while far-red fluorescence remained rather constant. This decline with ageing is interpreted as an effect of age-dependent photosynthetic limitation or as a decline of stomatal conductance due to hydraulic limitations and opens a promising path with regard to how fluorescence measurements can be used for forest age mapping.

# 2 Introduction and background

Vegetation monitoring has been one of the key objectives of many different satellite missions in the past. The FLuorescence EXplorer (FLEX) is the first satellite mission to be designed specifically for the measurement of passive, sun-induced, chlorophyll fluorescence in terrestrial vegetation [RD-1]. FLEX was selected in November 2015 as ESA's 8th Earth Explorer, to be launched in 2022 and to operate for 3 to 5 years in tandem with ESA's Sentinel-3 (S-3) (Drusch *et al*. 2016). The FLEX/S-3 tandem mission will support both the retrieval of sun-induced fluorescence and its interpretation through the acquisition of complementary and synergistic data [RD-2]. Sun-induced fluorescence and associated biophysical data products derived from the FLEX/S-3 mission will be used as additional information to quantify actual photosynthetic performance and stress responses for a range of applications spanning the fields of agriculture, forestry, and environmental science [RD-1]. Previous studies, such as the FLEX/S3 Tandem Mission Photosynthesis Study [RD-3], developed a consolidated leaf-canopy SIF-photosynthesis model based on SCOPE (Van der Tol *et al*. 2009). In addition, stress indicators were analyzed, and a conceptual framework was proposed to guide stress detection using FLEX.

The HYFLEX campaign in 2014 ('*Technical assistance for the deployment of an advanced hyperspectral imaging sensor during FLEX-EU';* Contract No. 4000107143, CCN2) aimed to investigate how stress influences the fluorescence signal and the photosynthetic response of vegetation canopies by dedicated treatment experiments on a grassland canopy in Italy. Data acquired during the FLEX-EU campaign were used in complementary ESA studies such as the FLEX/S3 Tandem Mission FLEX-BRIDGE [RD-4].

Furthermore, additional *HyPlant* data over Germany and the Czech Republic were acquired, as part of multi-temporal recording, to assess the spatio-temporal changes of the fluorescence signal across different ecosystems.

# 3 Campaign objectives

The overall objectives of the FLEX-EU activity were (objectives are reordered to reflect the structure of this report):

1. Acquire and process high-quality hyperspectral datasets of fluorescence in conjunction with extended correlative data

2. Perform initial analyses of data quality and generate first estimates of fluorescence.

3. Explore if the fluorescence signal scales proportionally when the fraction soil cover changes.
4. Assess how changes in energy dissipation pathways caused by different factors modulate changes in photosynthetic rates and fluorescence.
5. Explore if major stress or soil amendment practices do have a detectable effect on fluorescence
6. Understand if fluorescence enables the detection of differences in canopy gas exchange of different crop species and at different times of the day.
7. Provide feedback for existing state-of-the-art fluorescence models. The dataset shall be utilized in the framework of this activity to test and evaluate different modelling approaches that simulate and retrieve top-of-canopy fluorescence.
8. *Additional objectives added in the course of the activity*: Explore the functional relationship between tree height and age and sun-induced fluorescence.

The abovementioned objectives are used to structure this report:

- Objective 1 + 2 (data acquisition and processing) were accomplished by the experimental components of this campaign. An overview of the data and an evaluation of the data quality is given in the data acquisition report. Additionally, an extensive data set of vegetation indices from the study sites is presented in this final report (chapter 6.1). This data set contributes to the recording of a long-term data set of selected study sites across various biomes.
- Objective 3 (scaling) is addressed in chapter 6.2. We performed a manipulative experiment in which fractional soil/vegetation cover was altered in a controlled manner. The results show conclusively that fluorescence scales linearly with fractional soil/vegetation cover
- Objectives 4, 5, and 6 (fluorescence and gas-exchange) are addressed in chapter 6.3. We performed an extensive experiment in which selected functional properties of the photosynthetic machinery were manipulated using specific biochemical agents (chapter 6.3.4 and 6.3.5). The results show complex variations in the functional parameters $F_{685}$, $F_{760}$, and PRI. However, the temporal dynamics of the physiological reaction of the photosynthetic apparatus to the manipulation is extremely complex and has been only partly understood.
- Objective 7 (contribution to the modelling) is addressed in chapter 8. Based on the findings above, a conceptual framework is developed regarding how fluorescence, PRI and other biophysical parameters can be included into models. The evaluation of different models cannot be concluded in this activity.
- Objective 8 (Relationship between tree height/age and fluorescence). Unfortunately the insufficient, geometric precision of the *HyPlant* data in this year made the investigation of the relationship between tree age and fluorescence impossible (inaccuracy in spatially co-registering the digital surface model and fluorescence data). The further investigation of the relationship was done on the FLEX-US dataset, even though it was not an objective in the FLEX-US study. Some aspects of these results will be included in the report (Appendix).

# 4 Instrumentation, material, and methods

This chapter gives a short summary of the main instrumentation, materials, and methods used during the measurements in 2014. Table 1 summarizes the equipment, and chapters 4.1 to 4.3 give a detailed description about the airborne sensor, the hyperspectral ground reference measurements, and the correlative ground measurements.

**Table 1: Main instrumentation used during FLEX-EU campaign 2014.**

| | Germany | Italy | Czech Republic |
|---|---|---|---|
| **Airborne** | *HyPlant,* Variocam | *HyPlant,* Variocam Tasi-600 | *HyPlant,* FLIR |
| **Atmospheric** | | | Sun photometer (Microtops) |
| **Ground reference (Cal/Val)** | ASD Field Spec | ASD Field Spec | ASD Field Spec |
| **Top-of-canopy reflectance and fluorescence** | ASD FieldSpec | Ocean Optics spectrometers S-FLUO Box, ASD FieldSpec | S-FLUO Box, ASD FieldSpec |
| **Correlative ground measurements** | | Canopy Chlorophyll Content (Chlorophyll extraction) gas exchange (chamber) Eddy Covariance | Eddy Covariance |

## 4.1 Airborne sensors

### 4.1.1 *HyPlant*: A high-performance imaging spectrometer for vegetation monitoring

The *HyPlant* sensor is a hyperspectral imaging system for airborne and ground-based use. It consists of two sensor heads. The DUAL module is a line-imaging, push-broom hyperspectral sensor, which provides contiguous spectral information from 370 to 2500 nm in one device utilizing a common fore objective lens with 3 nm spectral resolution in the VIS/NIR spectral range and 10 nm spectral resolution in the SWIR spectral range. The vegetation fluorescence signal is measured with a separate push-broom sensor, the FLUO module, which produces data at high-spectral resolution (0.25 nm) in the spectral region of the two oxygen absorption bands. The Data Acquisition and Power Unit contain two rack modules. The first module includes the data acquisition computer with system control and data acquisition software and the power supply and control electronics for the DUAL module and GPS/INS sensor. The second module includes the same equipment for the FLUO module. The Position and Altitude Sensor (GPS/INS sensor) provides, synchronously with the image data, aircraft position and altitude data for image rectification and georeferencing. Both imagers (DUAL and FLUO module) are mounted on a single platform with the mechanical capability to align the field of view (FOV) (Figure 1).
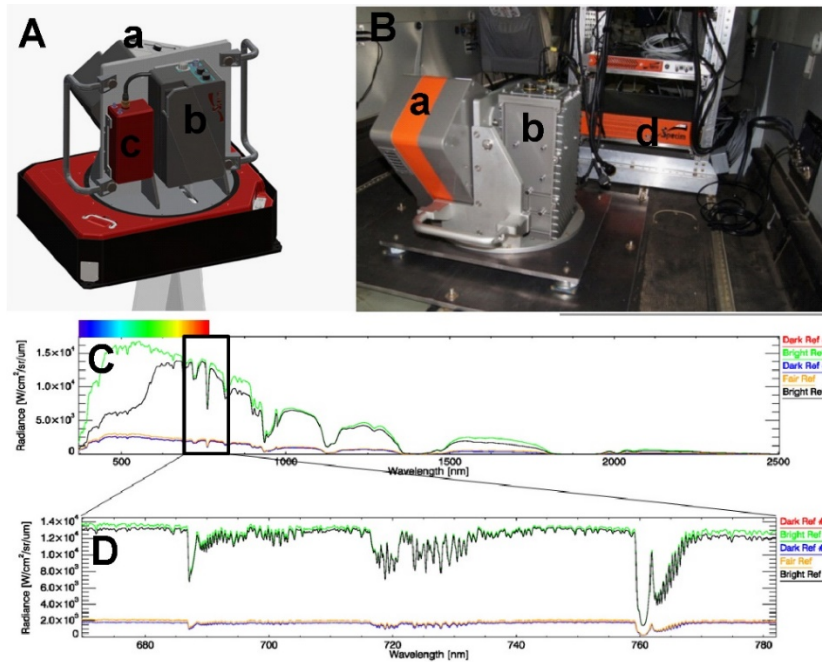
**Figure 1:** Schematic drawing of the *HyPlant* sensor consisting of the broadband DUAL module (a) and the high-resolution FLUO module (b).
Additionally, the GPS/IMU positioning unit that is attached to the rack is shown (c).
B: Installation of HyPlant within a Cessna aircraft. In the back the data acquisition unit is visible (d)
C, D: Representative radiance measurements from different surfaces from the DUAL and the FLUO module, respectively.

The *HyPlant* system (*HyPlant_0*) was employed during the HYFLEX 2012 campaign and intensively tested [RD-5]. The sensor performed fine under airborne operation, but some technical problems were identified. The DUAL module showed a clear mirror image. The FLUO module had `flickering' pixels and a slightly lower signal-to-noise ratio (SNR) than specified. Those issues were solved with the technical upgrade of the sensor in the beginning of 2013. The optical path of the DUAL module was aligned to remove the mirror image. The camera of the FLUO module was exchanged to remove the `flickering` pixels, and the SNR was improved from improved from 14 to 16 bit.
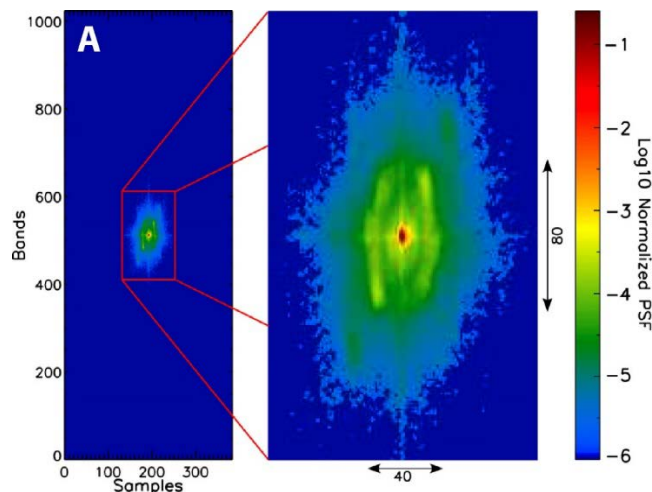


**Figure 2: Point spread functions (PSF) of FLUO the sensor for the calendar years 2013 and 2014. The PSF is normalized to the total energy and represented in log scale. On the left is the full**

**sensor frame. On the right is the magnified extension of the PSF. Note that typical sensor noise is in the order of $10^{-5}$ in this scale.**

**Table 2: Sensor characteristics evaluated in 2013 in flight data (the nominal/specified performance values are given in parentheses).**

| Sensor | Dual module | | FLUO module |
|---|---|---|---|
| **Spectral Performance** | | | |
| Range [nm] | 370–970 | 970–2500 | 670–780 |
| Bands # | 350 | 272 | 1024 |
| Sampling interval [nm] | 1.7 (1.75) | 5.5 (6.0) | 0.11 (0.11) |
| Resolution (FWHM) [nm] | 4.0 (<3.5) | 13.3 (<10) | 0.25 at $O_2$-A (<0.26) 0.23 at $O_2$-B (<0.26) |
| Band broadening [nm] | 0.2 | 0.2 | 0.1 at $O_2$-A(-) 0.3 at $O_2$-B (-) |
| Spectral shift | 1.2 | 2.4 | <0.04 (-) |
| Smile [nm] | 0.4 (<0.42) | 1.2 (<0.66) | <0.01 at $O_2$-A(-) 0.01 at $O_2$-B (-) |
| **Radiometric Performance** | | | |
| SNR with full-scale signal | - (510) | - (1100) | - (240) |
| Stray light and pixel cross talk [%] | - (<0.5) | - (<0.6) | - (<0.5) |
| **Spatial Performance** | | | |
| Spatial pixels | 384 | 384 | 384 |
| FOV [deg] | 32.3 | | 32.3 |
| IFOV* [deg] | 0.0832 | | 0.0832 |
| Swath [m] | 380 @ 600m AGL | | 380 @ 600m AGL |
| Spatial sampling interval (across track) [m] | 0.98 @ 600m AGL | | 0.98 @ 600m AGL |
| Keystone [µm] | - (<3.925) | - (<3.925) | - (<3.925) |
| **Sensor Type** | | | |
| Type | CMOS | MCT | sCMOS |
| Dynamic range | 12 bit | 14 bit | 16 bit |

The technically upgraded *HyPlant_1* system was operated in the 2013 and 2014 ESA campaigns. The radiometric performance of the modules showed values according to the specifications (Table 2). The additional measurements and calibration at the Specim calibration facility in the beginning of 2014 revealed a wide PSF (Figure 2). To correct for this PSF, a deconvolution algorithm based on the PSF characterization was implemented as a pre-processing step in the *HyPlant* processing chain (Figure 3).

### 4.1.2  *HyPlant* data processing
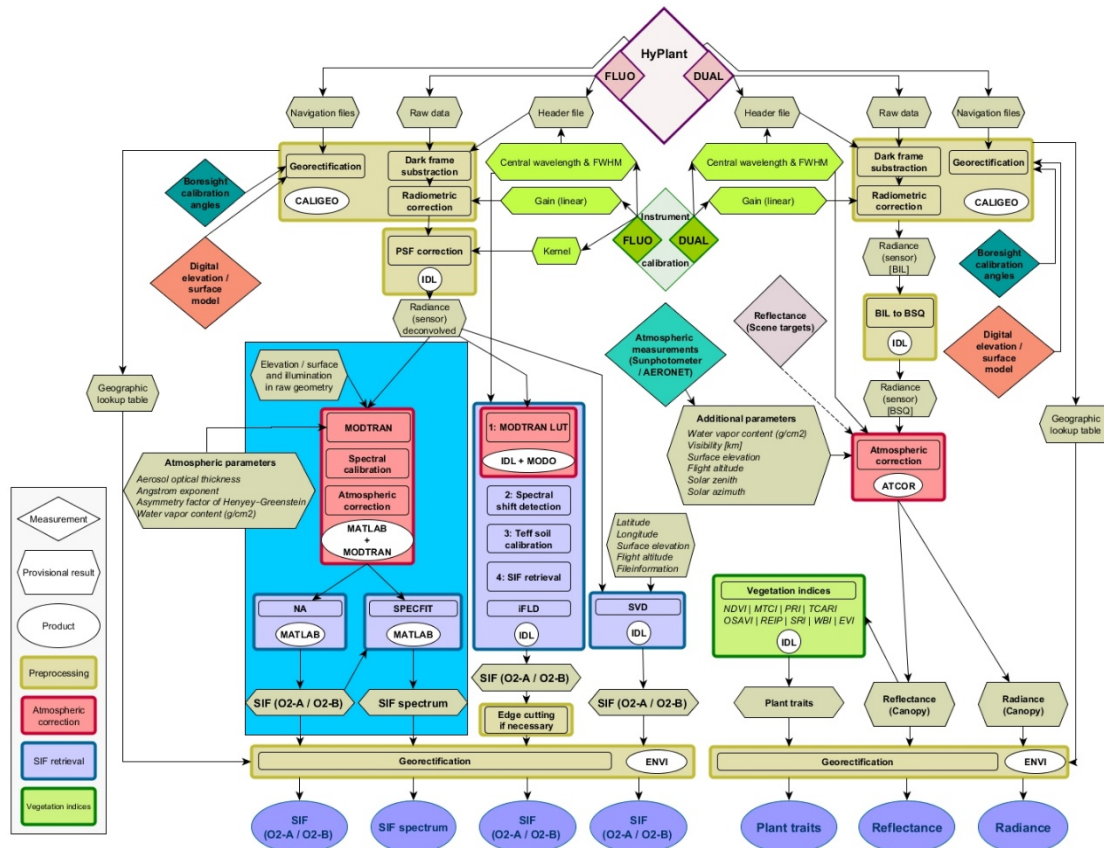


**Figure 3: Flowchart of the *HyPlant* processing chain.**

The *HyPlant* processing chain (Figure 3) gives an overview of the single processing steps of the FLUO and DUAL module, from raw data to final products, such as vegetation indices and fluorescence maps. The main processing steps are labelled with an appendix in the file name of the flight line (Table 3). Each file name contains the acquisition date, area, and time, as well as information about the flight altitude from which the ground pixel size can be concluded. As basic information, the name of the flight line, heading of the aircraft during the acquisition, and from which module (DUAL or FLUO) the flight line was recorded is given as well. When the radiometric and wavelength calibration are applied to the flight line, the appendix *radiance* is added. The atmospheric correction of the DUAL data is done using ATCOR. Top-of-canopy (TOC) radiance files are stored with the *img_surfrad*; TOC reflectance files where additional spectral polishing and smile correction was applied are labelled with *img_atm_polish_smcorr*. From the TOC reflectance data, different vegetation indices (see chapter 4.1.2.2) are calculated and labelled with the appendix *indices_up*. For the FLUO module, the label *deconv_i1* indicated the deconvolution of the spectra to correct the point spread function. The label *Fs_linear_v2*, indicates the fluorescence maps that were calculated with the SVD method. The label *FIXDEM_V5* shows that the maps were calculated with the iFLD method (see chapter 4.1.2.1). *HyPlant* modules with the label *rect* indicate that the calculated product was georectified.

**Table 3: The file name for each flight line recorded of the HyPlant has the following format. Final products are marked as bold.**

| Acquisition date | Acquisition area | Recording time (local) | Flight altitude | Flight line name | Heading | Module of the sensor | Processing steps DUAL | Processing steps FLUO |
|---|---|---|---|---|---|---|---|---|
| YYYYMMDD | -fluomap (Figure 34) | -hh:mm | -1800 (3m x 3m pixel) | L1, 2… | S, N… | -DUAL | -radiance (radiometric calibration file of SPECIM was applied) | -radiance (radiometric calibration file of SPECIM was applied) |
| | -MEZ (Figure 25) | | -0600 (1m x 1m pixel) | | | -FLUO | **-img_surfrad (atmospherically corrected radiance data)** | -deconv_i1 (deconvolution of the spectra to correct the point spread function) |
| | -SEL (Figure 25) | | | | | | **-img_atm_polish_smcorr (atmospherically corrected reflectance data, with applied spectral polishing and smile correction)** | **-FIXDEM_V5 (fluorescence maps calculated with the iFLD method)** |
| | -CKA (Figure 26) | | | | | | **-indices_up (calculation of selected vegetation indices)** | **-Fs_linear_v2 (fluorescence maps calculated with the SVD method)** |
| | -CAR (Figure 28) | | | | | | **-rect (georectification using the GLT file)** | **-rect (georectification using the GLT file)** |
| | -LAT (Figure 29) -BK (Figure 30) -STI (Figure 32) | | | | | | | |
| | -VIN (Figure 27) | | -0350 (0.5m x 1m pixel) | | | | | |

#### 4.1.2.1 Fluorescence retrieval

The processing scheme of *HyPlant*–FLUO is given in Figure 3. All FLUO module flight lines acquired within the FLEX-EU campaign were processed to georectified, at-sensor radiance data using the most recent wavelength and radiometric calibration file provided by the Specim in 2014. The Point Spread Function (PSF) as presented in Figure 2 was corrected for each flight line of the fluorescence flight lines and is also based on calibration measurements of 2014. The deconvolution follows the Van-Cittert approach that consists of an iterative algorithm.

For the fluorescence retrieval, three different retrieval algorithms are available. The most advanced algorithm is the Spectral Fitting Method (SFM), after Cogliati *et al.* (2015). It permits decoupling sun-induced fluorescence and surface reflected radiance from total at-sensor signal. The retrieval method uses a physically-based approach for deriving downward/upward surface radiances, therefore it strongly depends on overall accuracy of atmospheric correction. Unfortunately such proper characterization is not available for the experiments in Italy (chapter 5.2). In addition, this algorithm can so far only be applied to flat terrain. Therefore, the SFM is also not applicable in the mountain area in Bílý Kříž.

**Improved Fraunhofer Line Discrimination**

Fluorescence maps of red and far-red fluorescence of the agricultural areas of Germany (chapter 5.1) and the main experimental field in Latisana, Italy (chapter 5.2) were calculated using the improved Fraunhofer Line Discrimination (iFLD). The method is based on the 3-FLD approach by Maier *et al.* (2003) and the iFLD method of Alonso *et al.* (2008). The method was adapted to the high spectrometers, complemented with the simulations of atmospheric components using MODTRAN (Berk *et al.* 2005).

Emitted fluorescence must be analytically separated from the reflected radiance flux measured with ground and airborne based spectrometers. We applied the Fraunhofer Line Depth (FLD) approach (Plascyk, 1975), which serves as a de facto standard for fluorescence retrievals using medium resolution instruments (Meroni *et al.*, 2009). The FLD method uses atmospheric absorption bands, characterized by lower incident light compared to wavelength regions outside of these bands. This configuration increases the spectral information and allows the separation of fluorescence from reflected radiation. In this study, we used the broad $O_2$-A oxygen absorption band around 760 nm and quantified the infilling of $F_{760}$ using radiance measurements inside (subscript i) and outside (subscript o) of the $O_2$-A band.

For the airborne case, only atmospheric components can be simulated with MODTRAN5 assuming perfect knowledge of the acquisition conditions. The reflectance terms for diffuse and direct irradiance as well as the SIF contribution are usually unknown. Assuming Lambertian surface reflectance behavior, which introduces some inaccuracies but allows formulating the radiative transfer (RT) for radiance measurements at sensor level ($L^{AtS}$), both measurements inside and outside of the absorption band, can be expressed as:

$$L_j^{AtS} = \frac{\langle E_j^0 \cos\theta_{il}\rangle}{\pi}\left[\langle\rho_{so}^j\rangle + \frac{(\langle\tau_{ss}^j\tau_{oo}^j\rangle + \langle\tau_{sd}^j\tau_{oo}^j\rangle + \langle\tau_{ss}^j\tau_{do}^j\rangle + \langle\tau_{sd}^j\tau_{do}^j\rangle)R_j}{1-R_j\langle\rho_{dd}^j\rangle}\right] + \frac{F_j(\langle\tau_{oo}^j\rangle + \langle\tau_{do}^j\rangle)}{1-R_j\langle\rho_{dd}^j\rangle}, \begin{cases} L_i = L_i^p + \frac{\left(E_i^0\frac{R_i}{\pi}+Fs_i\right)\cdot T_i}{1-S_i\cdot R_i} \\ L_o = L_o^p + \frac{\left(E_o^0\frac{R_o}{\pi}+Fs_o\right)\cdot T_o}{1-S_o\cdot R_o} \end{cases} j = i, o$$

$$(3)$$

where $E_j$ is the surface irradiance including diffuse and direct components, $\theta_{il}$ is the illumination zenith angle, $\rho_{so}$ is the path scattered radiance, $\tau_{ss}$ is the direct transmittance for sunlight, $\tau_{oo}$ is the direct transmittance in view direction, $\tau_{sd}$ is the diffuse transmittance of the atmosphere for sunlight, $\tau_{do}$ is the

hemispherical-directional transmittance in view direction, and $\rho_{dd}$ is the spherical albedo. If these atmospheric components are obtained from MODTRAN5 simulations (Damm *et al.,* 2015), the radiative transfer equation (Eq. 3) only contains four unknowns, namely $R_i$, $R_o$, $F_i$, and $F_o$. The iFLD method (Alonso *et al.,* 2008), an adaptations of the original FLD method proposed by (Plascyk, 1975), was used to non-linearly (spline) relate R and F inside and outside of the $O_2$-A absorption band. F can be finally retrieved with:

$$F_i = \frac{B\left[\frac{X_i\left(E_o + X_o\langle\rho^o_{dd}\rangle\right) - AX_o\left(E_i + X_i\langle\rho^i_{dd}\rangle\right)}{B\left(E_o + X_o\langle\rho^o_{dd}\rangle\right) - A\left(E_i + X_i\langle\rho^i_{dd}\rangle\right)}\right]}{\langle\tau^i_{oo}\rangle + \langle\tau^i_{do}\rangle} \tag{4}$$

$$X_j = \left(L^{AtS}_j - \frac{\langle E^o_j \cos\theta_{il}\rangle}{\pi}\langle\rho^j_{so}\rangle\right), \qquad j = i, o \tag{5}$$

$$E_j = \frac{\langle E^o_j \cos\theta_{il}\rangle}{\pi}\left(\langle\tau^j_{ss}\tau^j_{oo}\rangle + \langle\tau^j_{sd}\tau^j_{oo}\rangle + \langle\tau^j_{ss}\tau^j_{do}\rangle + \langle\tau^j_{sd}\tau^j_{do}\rangle\right) = \left[E^{dir}_j + E^{dif}_j\right], \quad j = i, o \tag{6}$$

$$R_i = AR_o$$
$$F_i\left(\langle\tau^i_{oo}\rangle + \langle\tau^i_{do}\rangle\right) = BF_o\left(\langle\tau^o_{oo}\rangle + \langle\tau^o_{do}\rangle\right) \tag{7}$$

where B is the factor relating $F_i$ and $F_o$ and was fixed to a value of 0.8, justified by simulations and experiments (Rascher *et al.,* 2009, Alonso *et al.,* 2008), $X_j$ equals the at-sensor radiance (reflected plus emitted radiation) without path radiance contribution and $E_j$ expresses surface irradiance as measured at the sensor level. The A is the factor relating $R_i$ and $R_o$, and was derived from linear 3rd order polynomial interpolation of R of the left (758 nm) and right (771 nm) $O_2$-A band shoulder with

$$A = \frac{R\omega_1 + R_{771}\omega_2}{R_{758}} \tag{8}$$

$$\omega_1 = \frac{771-760}{771-758}, \text{ and } \omega_2 = \frac{760-758}{771-758} \tag{9}$$

In addition, an empirical constraint based on non-vegetation reference surfaces is used after Damm *et al.* (2014). The improvement of the estimation of the atmospheric parameters in particular are more theoretical and in unstable atmospheric conditions, and therefore do not always yield a proper path scattered radiance, which is determined by the aerosol optical thickness. An underestimation of the path scattered radiance results in an underestimation of the fluorescence in bright targets and a false fluorescence in dark target and shadows. In case of the Latisana treatment experiment (chapter 6.3), the pseudo-invariant reference tarps, which were placed in the flight line and the dark areas, were used to correct empirically this scatter path radiance as an additional brightness correction.


**Singular Vector Decomposition (SVD)**

In the mountain and forest area of Bílý Kříž, the only applicable fluorescence retrieval so far is the Singular Vector Decomposition (SVD) to obtain fluorescence values at 680 nm and 740 nm. The method is based on a semi-empirical radiative transfer formulation and was first developed by Guanter *et al.* (2012, 2013). The method was previously used for fluorescence retrieval from *HyPlant* recordings in Rossini *et al.* (2015). The data-driven fluorescence retrieval approach represents the measured at-sensor radiance spectrum as a linear combination of reflected solar radiance and fluorescence emission spectra. The reflected solar radiance is formulated as a linear combination of singular vectors (SVs), which are

derived after performing a Singular Vector Decomposition of a set of reference (fluorescence-free) spectra. The combination of the derived SVs is able to reproduce any fluorescence-free spectra. This data-driven formulation of the forward model avoids the explicit modeling of atmospheric radiative transfer and the instrument's spectral and radiometric responses, which are typically prone to errors larger than the fluorescence signal itself. The SVs are derived using non-fluorescence training pixels, which are determined by a threshold on the Normalized Difference Vegetation Index (NDVI). We typically used 4–5 SVs to model the 'at-sensor' radiance signal. A few adjustments were applied to improve the inversion results, such as the removal of the strongest absorption features or the spectral normalization (continuum removal) of canopy and reference radiances.

### 4.1.2.2  Top-of-canopy reflectance and vegetation indices

Data from the DUAL module was also processed to georectified a-sensor radiance using Caligeo and the Specim provided calibration files (Figure 3). Subsequently, data were atmospherically corrected using ATCOR and top-of-canopy (TOC) radiance and reflectance was stored. From the TOC reflectance data selected vegetation indices were calculated according to formula (1)-(12).

**Indices related to chlorophyll content and leaf area index**

*Simple Ratio (SR)*

The simple ratio (SR, formula (10)) shows a ration between near infrared and the red spectral region and enhances the contrast of soil and vegetation (Asrar *et al*. 1984).

$$SR = \frac{R_{<795-810>}}{R_{<665-680>}} \tag{10}$$

The spectral windows correspond to 9 bands in *HyPlant* (centre wavelength ± 4 bands).

*Normalized Difference Vegetation Index (NDVI)*

The Normalized Difference Vegetation Index (NDVI, formula (11)) can theoretically accept values from -1 to 1. Green and dense forest vegetation shows high NDVI values. It should be noted that the NDVI saturates with high Leaf Area Index (LAI< 5) (Rouse *et al*. 1973).

$$NDVI = \frac{R_{<795-810>} - R_{<665-680>}}{R_{<795-810>} + R_{<665-680>}} \tag{11}$$

The spectral windows correspond to 9 bands in *HyPlant* (centre wavelength ± 4 bands).

### Red-edge Normalized Difference Vegetation Index (NDVI$_{re}$)

The Red-edge Normalized Difference Vegetation Index (NDVI$_{re}$, formula (12)) is a modification of the traditional broadband NDVI. This VI differs from the NDVI by using bands along the red edge, instead of the main absorption and reflectance peaks. It capitalizes on the sensitivity of the vegetation red edge to small changes in canopy foliage content, gap fraction, and senescence. The value of this index ranges from -1 to 1. The common range for green vegetation is 0.2 to 0.9 (Gitelson and Merzlyak 1994; Sim *et al*. 2002).

$$NDVI_{re} = \frac{R_{<735-750>} - R_{<695-710>}}{R_{<735-750>} + R_{<695-710>}} \tag{12}$$

The spectral windows correspond to 9 bands in *HyPlant* (centre wavelength ± 4 bands).

### Enhanced Vegetation Index (EVI)

The Enhanced Vegetation Index (EVI, formula (13)) is a VI that is more sensitive to areas with high biomass and should minimize the influence of the background signal and atmospheric influences (Huete *et al*. 2002).

$$EVI = 2.5 \left[ \frac{R_{<795-810>} - R_{<665-680>}}{R_{<795-810>} + 6 \cdot R_{<665-680>} - 7.5 \cdot R_{<475-490>} + 1} \right] \tag{13}$$

The spectral windows correspond to 9 bands in *HyPlant* (centre wavelength ± 4 bands).

### Red-Edge Position (REP)

This Red-Edge Position (REP, formula (14, 15)) index is a narrowband reflectance measurement that is sensitive to changes in chlorophyll concentration. Increased chlorophyll concentration broadens the absorption feature and moves the red edge to longer wavelengths (Dawson and Curran 1998).

$$R_i = \frac{R_{<665-680>} + R_{<795-810>}}{2} \tag{14}$$

The spectral windows correspond to 9 bands in *HyPlant* (centre wavelength ± 4 bands).

$$REP = 700 + 40 \frac{R_i - R_{700}}{R_{740} - R_{700}} \quad \text{[nm]} \tag{15 with (14)}$$

The result is a wavelength that indicates the position of the inflection of the red edge.

### *MERIS Terrestrial Chlorophyll Index (MTCI)*

The MERIS terrestrial chlorophyll index (MTCI, formula (16)) provides information on the chlorophyll content of vegetation. This is a combination of information on leaf-area index. The MTCI correlates strongly with chlorophyll content when using model, laboratory, and field spectrometry data (Dash and Curran *et al.* 2007).

$$MTCI = \left(\frac{R_{754\pm7.5}-R_{709\pm10}}{R_{709\pm10}-R_{681\pm7.5}}\right) \tag{16}$$

This index is developed for MERIS; therefore, we give here the central wavelengths and the widths that correspond to the MERIS bands. We aim to represent the spectral resolution of MERIS and thus propose using 9 bands (centre wavelength ± 4 bands) for the 681 and 754 nm (app. 15 nm spectral window) and 11 bands (centre wavelength ± 5 bands) for the 709 nm (app. 20 nm spectral window) in *HyPlant*.

### *Transformed Chlorophyll Absorption in Reflectance Index (TCARI)*

The Transformed Chlorophyll Absorption in Reflectance Index (TCARI, formula (17)) indicates the relative abundance of chlorophyll. It is affected by the underlying soil reflectance, particularly in vegetation with a low LAI (Haboudane *et al.* 2002).

$$TCARI = 3\left[(R_{700\pm4}-R_{670\pm4}) - 0.2\cdot(R_{700\pm4}-R_{550\pm4})\cdot\frac{R_{700\pm4}}{R_{670\pm4}}\right] \tag{17}$$

TCARI is developed to use a smaller spectral window for the single bands and various definitions are available in the literature. Thus, we propose to use smaller spectral windows corresponding to 5 bands (app 8 nm spectral window) in *HyPlant* (centre wavelength ± 2 bands).

### **Indices related to photosynthesis and non-photochemical quenching**

### *Photochemical Reflectance Index (PRI)*

The photochemical reflectance index (PRI, Formula (18)) is related to the non-photochemical quenching (NPQ) of the vegetation and should therefore be positively related to the light use efficiency of the vegetation canopy. The interpretation of the PRI sometimes remains difficult because, as the VI is sensitive to structural and illumination effects.

$$PRI = \frac{R_{<570\pm2.5>} - R_{<531\pm2.5>}}{R_{<570\pm2.5>} + R_{<531\pm2.5>}}$$ (18)

This is the original formula as proposed by Gamon *et al.* (1992). In this expression, the PRI correlates positively with NPQ. For the reference wavelength at 570 nm, we propose to use a spectral window of app. 5 nm (3 bands in *HyPlant*, centre wavelength ± 1 bands). For $R_{531}$, we propose to use a similar spectral window of app. 5 nm (3 bands, centre wavelength ± 1 band).

The motivation comes from the study in FLEX-Bridge [RD-4]. There it became clear that the spectra are noisy and spectral binning seems to be an appropriate option to compensate for noise because the reflectance change caused by NPQ around 531 nm are relatively 'broad'. However, the reference wavelength (570 nm) seems to be affected by certain features as well, meaning it is spectrally less stable than expected. Therefore, we recommend using only 3 bands (centre +/- 1 band) to avoid further sensitivities of the PRI for pigment pool sizes, for example.

Additionally to the formulation of the PRI in formula (18), we also calculated the PRI to the later formulation of Gamon *et al.* (1997). With this formulation the PRI and NPQ are negative correlated. This additional PRI calculation was only done for the core dataset of the Latisana treatment experiment (chapter 6.3) because those PRI maps were already used for the FLEX Bridge study [RD-4].

### *Canopy Photochemical Reflectance Index (cPRI)*

According to the FLEX-Bridge study [RD-4], Wu *et al.* (2015) has the most promising canopy PRI index, which is less sensitive with regard to pigment pool sizes, and structural and atmospheric effects. Thus, we calculate the cPRI (modified after Wu *et al.* 2015).

$$cPRI = PRI - 0.15(1 - e^{-0.5 \cdot LAI})$$ (19) with (18)

In the original formulation (eq. 19), the LAI needs to be known. We propose to use the Simple Ratio (eq. 10) as approximation for LAI. Thus, the formula that should be finally included in the processing module is eq. 20. The additive term of 0.2, originally proposed by Wu *et al.* (2015), is sensor specific and thus is omitted in the formula to be implemented for *HyPlant*.

$$cPRI = \frac{R_{<570\pm2.5>} - R_{<531\pm2.5>}}{R_{<570\pm2.5>} + R_{<531\pm2.5>}} - 0.15\left(1 - e^{-0.5\cdot\frac{R_{<795-810>}}{R_{<665-680>}}}\right) \qquad \text{(20) with (18)}$$

Again, for both PRI wavelengths at 530 nm and 570 nm, we propose to use a spectral window of app. 5 nm (3 bands in *HyPlant*, centre wavelength ± 1 bands). For the SR, both spectral windows (i.e., 795–810 and 665–680) correspond to 9 bands in *HyPlant* (centre wavelength ± 4 bands).

## **Indices related to canopy water content**

### *Water Band Index (WBI)*

The Water Band Index (WBI, formula (21)) is a simple ratio index that is sensitive to differences in canopy water status. An increase in the canopy water content is reflected as a higher absorption at 970 nm relative to the 900 nm reference band (Peñuelas *et al.* 1993).

$$WBI = \frac{R_{<955-970>}}{R_{<890-905>}} \qquad (21)$$

The spectral windows correspond to 9 bands in *HyPlant* (centre wavelength ± 4 bands). These spectral windows are at the very edge of the VIS/NIR module; the last waveband of the VIS/NIR module of *HyPlant* is at 969.1 nm. Therefore, we propose to use the last 9 bands of the VIS/NIR camera for calculating the spectral window <955–970>.

### 4.1.2.3  Airborne platforms

In 2014, *HyPlant* was operated on two different aircraft platforms. A Cessna Grand Caravan C208B from CAE Aviation (www.cae-aviation.com) with dual camera hatches (Figure 4). *HyPlant* was installed in the front hatch, and a simple thermal camera was also mounted on the same aircraft in the second hatch. For thermal imaging, a VarioCAM® hr head (Infratec, Germany) was used (weight 1.3 kg). The spectral range of this camera is 7.5 µm to 14 µm. The standard objective has a field of view (FOV) of 30° by 23°. The uncooled focal-plane-array sensor has a resolution of 640 by 480 pixels, with a measuring accuracy of ± 1K and a thermal sensitivity of lower than 30 mK. At 1 m distance, the FOV is 0.533 m by 0.4 m. One pixel has a size of 0.833 mm, so that the smallest detectable object for this distance has a size of about 2.5 mm. The camera is connected to a laptop via GigaEthernet and approached with the IRBIS® 3 software (Infratec, Germany), which allows real-time tracking of the measurements and correction of the absolute temperature by setting of emissivity, background temperature, ambient air temperature, air

humidity, and the object's distance. Additionally, the frame rate can be set manually up to 50 Hz. This setup was employed for the campaigns in Germany and Italy.

As a second airborne platform, the structurally identical C208B of CzechGlobe was used during the Czech Republic campaign (Figure 5).



**Figure 4: Cessna Grand Caravan C208B with dual camera hatches (CAE Aviation) with *HyPlant* and VarioCam.**



**Figure 5: Cessna Grand Caravan C208B (CzechGlobe) with *HyPlant* and FLIR Camera.**

### 4.1.2.4 Georectification of *HyPlant* data

*HyPlant* has an integrated OXFORD GPS/IMU unit. The georectification of the *HyPlant* data for the FLUO and DUAL module are done with the software tool CaliGeoPro provided by the *HyPlant* manufacturer Specim (Finnland) and the data recorded from the Oxford unit. On 22 May 2014, after the installation of *HyPlant* on the CAE aircraft (Figure 4), a boresight flight with the pattern given in Figure 6 was performed.

After the installation of *HyPlant* on the aircraft of Czech Globe in July 2014, a new boresight flight was performed in above Modřice according to the following pattern Figure 7.
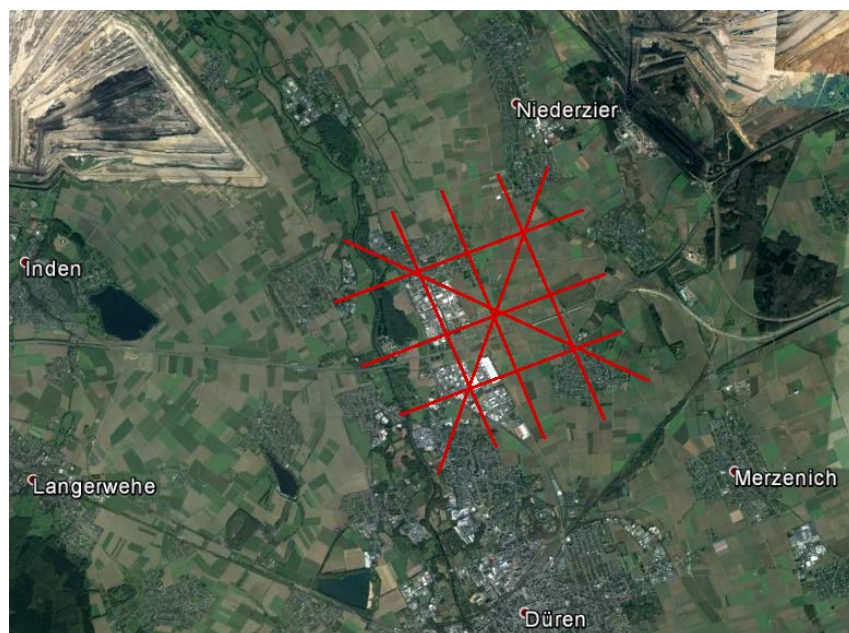
**Figure 6: Boresight pattern of eight flight lines in the Jülich area in Germany.**
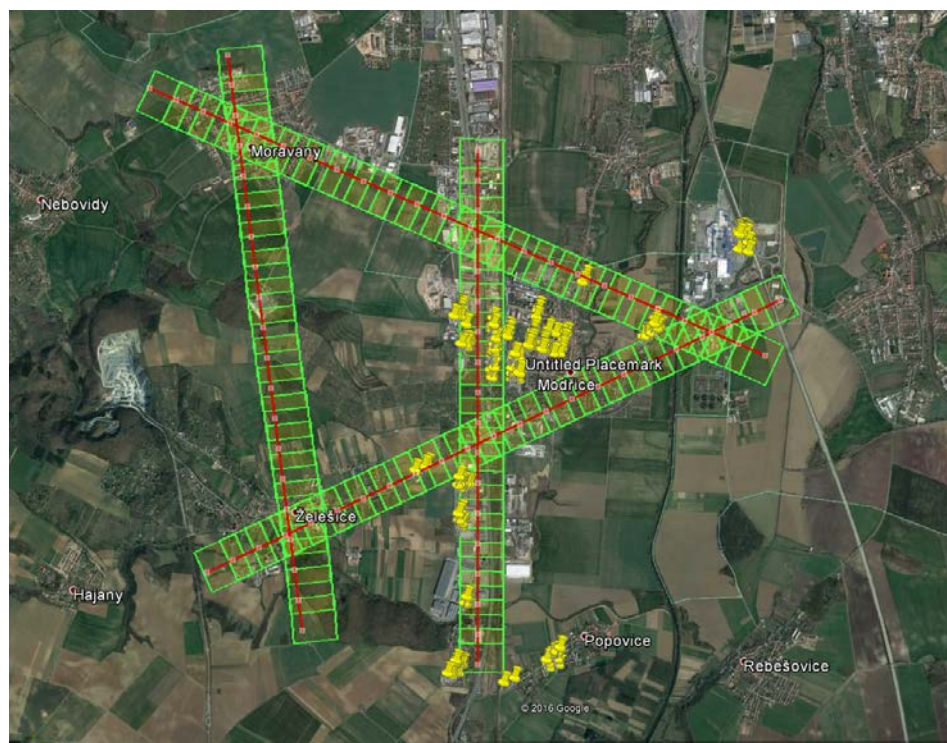


**Figure 7: Boresight pattern of 4 flight lines in Modřice, Czech Republic. The yellow pins indicate the position of available ground control points (GCP).**

For Germany, the boresight evaluation was done only with Tie points as no GCPs were available. For Modřice, Czech Republic boresight evaluation was done with the available GCP´s for this area. The implementation of the boresight angles showed an improvement compared to the georectification of the flight lines without the boresight angles but an inaccuracy of up to 7 pixels remained (Figure 8).

**Without boresight angles**     **With boresight angles**
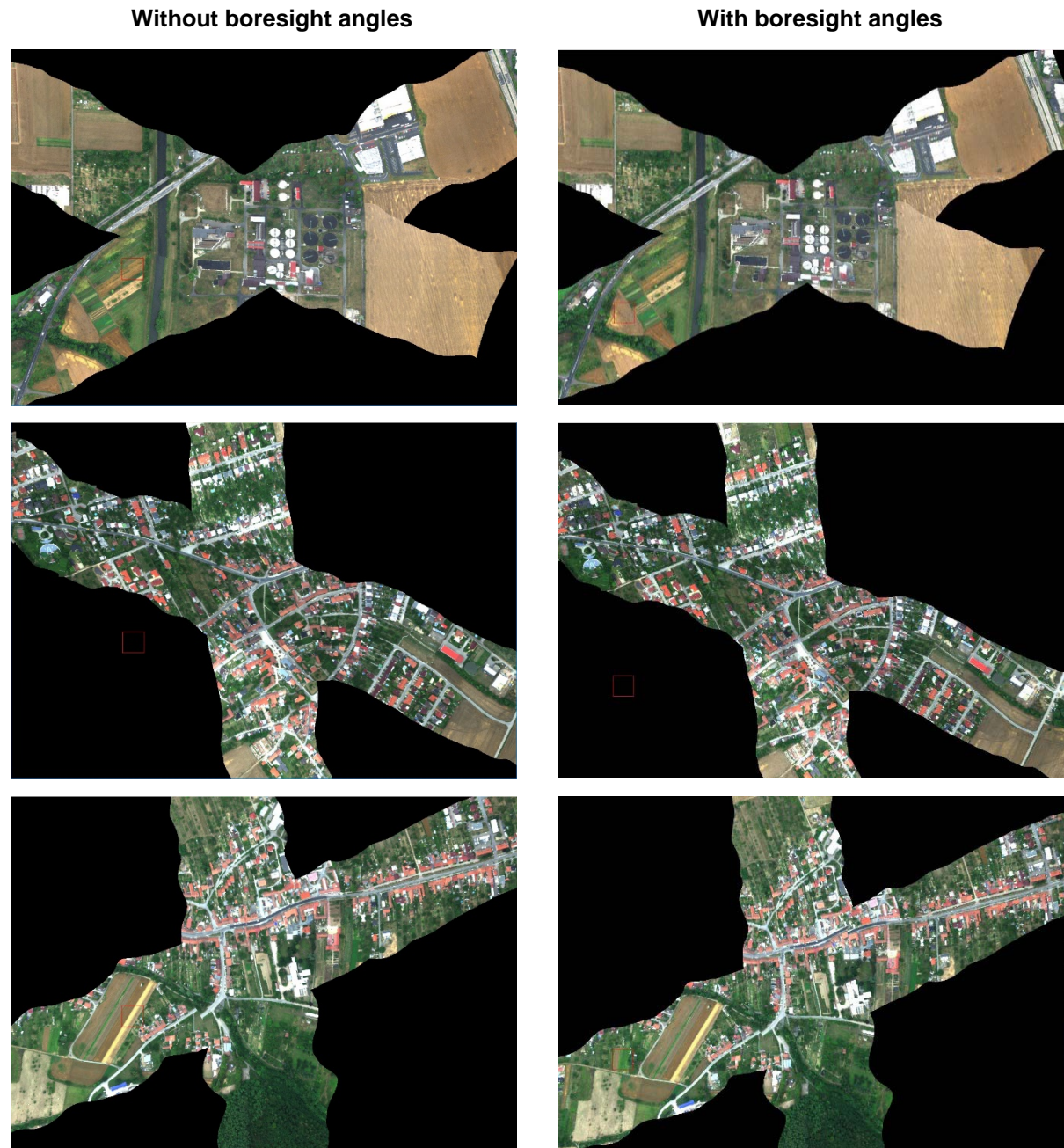


**Figure 8: Left: Overlap of the flight lines without boresight angles. Right: Overlap of the flight line with calculated boresight angles including the GCPs.**

The remaining inaccuracy provides some challenges for the further analyses of the data. For the direct comparison of the plots of the treatment experiment (chapter 6.3.1), the *HyPlant* core data sets (Table 24) were manually warped to enable pixel-by-pixel comparison of different flight lines in the same region of interest.

Additional manual georectification was not done for the large maps of the agricultural area in Selhausen and the forest in Bílý Kříž, and the maps may show some spatial inaccuracy between the recorded lines. The geometric correction of the Bílý Kříž area is critical. The available information of the DEM of the area was used for the georectification. Nevertheless, the mountain terrain in Bílý Kříž enhances the inaccuracy, and the shift between the different flight lines increases. An object-based analysis of single tree crowns, in combination with additional dataset is therefore not possible.

### 4.1.3  TASI-600

The Thermal Airborne Spectrographic Imager (TASI) by ITRES© is a pushbroom hyperspectral sensor with a 40º Field-Of-View operating in the thermal infrared spectral region. The photons are focused on a two-dimensional (2-D) sensor array (focal plane—FP) that records 640 across-track pixels at 60 different wavelengths (rows of the FP). Thermal IR photons emitted from the scene are focused on a plane through two curved slits generating hyperspectral images with 640 across-track pixels with 6% overlapping. Only about 40 rows contain a sufficient amount of information from the recorded scene and contribute to provide 32 bands at the system nominal wavelengths at the end of the ITRES processing chain (radiometric calibration, spectral alignment, and preliminary removal of anomalous pixels). The nominally acquired 32 bands with 109.5 nm of spectral width provide continuous spectral coverage in the wavelength range of 8.0–11.5 µm (ITRES ®, 2010).

Bands are calibrated radiometrically, aligned spectrally, and filtered to remove blinking pixels. At the end of the processing chain, 32-band hyperspectral data at the system-nominal wavelengths are provided.

The following Table 4 resumes the main TASI sensor characteristics:

**Table 4: TASI-600 main optical characteristics.**

| TASI-600 SN#5506 | |
|---|---|
| Spectral range (nm) | 8,000–11,504 |
| Across track pixel | 600 |
| Spectral channels | 32 |
| FHWM (nm) | 109.50 |
| FPA pitch | 30 x 30 micron |
| FOV | 40.27° |
| IFOV | 1.13 mrad |
| Foreoptics | f/1.5 |

The TASI sensor is supported by a calibration certificate (#486) and assesses the Noise Equivalence Delta Radiance NE$\Delta$R in mWm$^{-2}$sr$^{-1}$um$^{-1}$, for 300K, 0.30 ms integration time, 120 knots at 1,000 m ASL, and square pixels. The sensor is presented in Table 5.

**Table 5: NE$\Delta$R as derived from the valid ITRES certification.**

| Wavelength (um) | NE$\Delta$R 600 across-track pixels |
|---|---|
| 8.038 | 29.681 |
| 10.015 | 33.493 |
| 11.034 | 49.582 |

The TASI sensor #5506 that was used in this campaign has 32 bands with a FHWM of 109.50 nm and centred according to the characteristics presented in Table 6.

The calibration stability (ration between retrieved radiance by DN and certified radiance of the calibration source) was assessed in terms of the percentage of error along all the wavelengths. For column 143, the percentage error ranges from 0.662 @ 8.055 $\mu$m to 0.116 @11.340 $\mu$m, whereas for column 349 the percentage of error ranges between 0.701 @ 9.150 $\mu$m and 0.006% @ 10.972$\mu$m.

**Table 6: Centre wavelengths for TASI #5506 channels.**

| Band # | Centre Wavelength (nm) | Band # | Centre Wavelength (nm) |
|---|---|---|---|
| 1 | 8054.75 | 17 | 9806.75 |
| 2 | 8164.25 | 18 | 9916.25 |
| 3 | 8273.75 | 19 | 10025.75 |
| 4 | 8383.25 | 20 | 10135.25 |
| 5 | 8492.75 | 21 | 10244.75 |
| 6 | 8602.25 | 22 | 10354.25 |
| 7 | 8711.75 | 23 | 10463.75 |
| 8 | 8821.25 | 24 | 10573.25 |
| 9 | 8930.75 | 25 | 10682.75 |
| 10 | 9040.25 | 26 | 10792.25 |
| 11 | 9149.75 | 27 | 10901.75 |
| 12 | 9259.25 | 28 | 11011.25 |
| 13 | 9368.75 | 29 | 11120.75 |
| 14 | 9478.25 | 30 | 11230.25 |
| 15 | 9587.75 | 31 | 11339.75 |
| 16 | 9697.25 | 32 | 11449.25 |

For the FLEX-EU campaigns, the TASI sensor was mounted on board of a P68 Partenavia aircraft (see Figure 9). The main specifications of Partenavia P68 Observer2 are summarized in Table 7:

**Table 7: Specifications of Partenavia P68 Observer2.**

| | |
|---|---|
| Typical speed | 52 m/s |
| Service ceiling | 19,200 ft |
| Typical operating height | 18,000 ft |
| Empty weight | 1,420 kg |
| Max. takeoff weight | 2,084 kg |
| Max payload | 660 kg |
| Total electrical power | 1.925 kW |
| Electrical power available | 1 kW at 27.5 V +/-0.5 V |

Aircraft altitude sensor was used with the TASI sensor. The IMU sensor was installed on the same mounting plate as the sensor head to ensure a precise sensor altitude definition (Figure 9). The aircraft sensor altitude presented in Table 8 was used for this.



**Figure 9: ITRES TASI-600 (left); Partenavia P68 Observer2 (right)**

**Table 8: Characteristics of the aircraft sensor altitude applied for the FLEX-EU deployment.**

| GPS/IMU | |
|---|---|
| L1/L2 GPS receiver (Novatel) | SPAN-SE-S-RT2-J |
| Data Rate (position) | 20 Hz |
| IMU(iMAR) | IMU-FSAS-E-EI-O |
| Data Rate (IMU) | 200 Hz |

## 4.1.4  TASI data processing

**TASI Data Acquisition**

In the FLEX-EU trial over the Italian test sites (Latisana, Carlino, and Spilimbergo/Vinyard), TASI-600 acquired images from 6 June (UTC 12:41 first strip) to 21 June (UTC 15:23 last strip) at a flight altitude varying from 500 to 1000 m a.s.l.

**TASI Filenames**

The filenames are defined according to the following criteria and have three parts identifying:

1. the sensor name: e.g. TASI

2. the date of the acquisition (yyyy_mm_dd): e.g. 2014_06_21

3. the time of the data recording (hhmmss): e.g. 142701

In accordance with the flight plan, the following TASI data were recorded (Table 9).

**Table 9: TASI-600 dataset over the Italian test site**

| Date | File name/date/time | Site | Average flight height a.s.l. (m) | Pixel size (m) | Integration time (ms) | Date | File name/date/time | Site | Average flight height a.s.l. (m) | Pixel size (m) | Integration time (ms) |
|---|---|---|---|---|---|---|---|---|---|---|---|
| **Flight 1** 11/06/2014 Local time | TASI_2014_06_11_144100 | Latisana 1 | 850 | 1 | 290 | **Flight 7** 17/06/2014 Local time | TASI_2014_06_17_135352 | Latisana | 500 | 0.5 | 340 |
| | TASI_2014_06_11_144706 | Water 1 | 850 | 1 | 290 | | TASI_2014_06_17_135822 | Latisana | 500 | 0.5 | 340 |
| | TASI_2014_06_11_145213 | Carlino line 1 | 850 | 1 | 290 | | TASI_2014_06_17_140325 | Latisana | 650 | 0.75 | 340 |
| | TASI_2014_06_11_145801 | Carlino line 2 | 850 | 1 | 290 | | TASI_2014_06_17_140804 | Latisana | 650 | 0.75 | 340 |
| | TASI_2014_06_11_150224 | Carlino line 3 | 850 | 1 | 290 | | TASI_2014_06_17_141330 | Latisana | 900 | 1 | 340 |
| | TASI_2014_06_11_150908 | Water 2 | 850 | 1 | 290 | | TASI_2014_06_17_141819 | Latisana | 900 | 1 | 340 |
| | TASI_2014_06_11_151442 | Latisana 2 | 850 | 1 | 290 | **Flight 8** 18/06/2014 UTC time | TASI_2014_06_18_130617 | Latisana | 900 | 1 | 300 |
| | TASI_2014_06_11_151910 | Latisana 3 | 850 | 1 | 290 | | TASI_2014_06_18_131418 | Latisana | 900 | 1 | 300 |
| **Flight 2** 12/06/2014 UTC time | TASI_2014_06_12_081425 | Latisana 1 | 850 | 1 | 320 | | TASI_2014_06_18_132034 | Latisana | 900 | 1 | 300 |
| | TASI_2014_06_12_082113 | Latisana 2 | 850 | 1 | 290 | | TASI_2014_06_18_132714 | Latisana | 900 | 1 | 300 |
| | TASI_2014_06_12_082723 | Latisana 3 | 850 | 1 | 290 | | TASI_2014_06_18_133350 | Latisana | 900 | 1 | 300 |
| | TASI_2014_06_12_083246 | Latisana 4 | 850 | 1 | 290 | | TASI_2014_06_18_134039 | Latisana | 900 | 1 | 300 |
| | TASI_2014_06_12_083811 | Latisana 5 | 850 | 1 | 290 | | TASI_2014_06_18_134737 | Latisana | 900 | 1 | 300 |
| | TASI_2014_06_12_084358 | Latisana 6 | 850 | 1 | 290 | **Flight 9** 19/06/2014 UTC time | TASI_2014_06_19_093256 | Mixed | 900 | 1 | 320 |
| | TASI_2014_06_12_084948 | Latisana 7 | 850 | 1 | 290 | | TASI_2014_06_19_093815 | Mixed | 900 | 1 | 320 |
| | TASI_2014_06_12_085514 | Latisana 8 | 850 | 1 | 290 | | TASI_2014_06_19_094429 | Mixed | 900 | 1 | 320 |
| | TASI_2014_06_12_090020 | Latisana 9 | 850 | 1 | 290 | | TASI_2014_06_19_095015 | Mixed | 900 | 1 | 320 |
| | TASI_2014_06_12_090542 | Latisana 10 | 850 | 1 | 290 | | TASI_2014_06_19_095544 | Mixed | 900 | 1 | 320 |
| | TASI_2014_06_12_091139 | Latisana 11 | 850 | 1 | 290 | | TASI_2014_06_19_100159 | Latisana | 900 | 1 | 320 |
| | TASI_2014_06_12_091735 | Latisana 12 | 850 | 1 | 290 | | TASI_2014_06_19_100806 | Latisana | 900 | 1 | 320 |
| | TASI_2014_06_12_092356 | Latisana 13 | 850 | 1 | 290 | | TASI_2014_06_19_101421 | Latisana | 900 | 1 | 320 |
| | TASI_2014_06_12_093020 | Latisana 14 | 850 | 1 | 290 | | TASI_2014_06_19_102016 | Latisana | 900 | 1 | 320 |
| | TASI_2014_06_12_093705 | Latisana 15 | 850 | 1 | 290 | | TASI_2014_06_19_102552 | Latisana | 900 | 1 | 320 |
| | TASI_2014_06_12_094332 | Latisana 16 | 850 | 1 | 290 | | TASI_2014_06_19_103246 | Latisana | 900 | 1 | 320 |

| | | |
|---|---|---|
| Doc.: Final Report | | |
| Date: 15-05-2016 | Issue: 1 | Revision: 0 |
| Ref.: ESA Contract No. 4000107143/12/NL/FF/lf CCN2 | | Page: 32 / 132 |

JÜLICH FORSCHUNGSZENTRUM

| | | | | | | | | | | | |
|---|---|---|---|---|---|---|---|---|---|---|---|
| | TASI 2014 06 12 094906 | Latisana 17 | 850 | 1 | 290 | | TASI 2014 06 19 103828 | Latisana | 900 | 1 | 320 |
| | TASI 2014 06 12 095505 | Latisana 18 | 850 | 1 | 290 | | TASI 2014 06 19 104439 | Latisana | 900 | 1 | 320 |
| | TASI 2014 06 12 100127 | Latisana 19 | 850 | 1 | 290 | | TASI 2014 06 19 105022 | Latisana | 900 | 1 | 320 |
| | TASI 2014 06 12 100700 | Latisana 20 | 850 | 1 | 290 | | TASI 2014 06 19 105648 | Latisana | 900 | 1 | 320 |
| | TASI 2014 06 12 101315 | Latisana 21 | 850 | 1 | 290 | | TASI 2014 06 19 110259 | Latisana | 900 | 1 | 320 |
| | TASI 2014 06 12 101925 | Latisana 22 | 850 | 1 | 290 | | TASI 2014 06 19 110922 | Latisana | 900 | 1 | 320 |
| | TASI 2014 06 12 102449 | Swimming pool | 850 | 1 | 290 | | TASI 2014 06 19 111541 | Latisana | 900 | 1 | 320 |
| | TASI 2014 06 12 142306 | Latisana 1 | 900 | 1 | 290 | | TASI 2014 06 19 112145 | Latisana | 900 | 1 | 320 |
| | TASI 2014 06 12 142858 | Latisana 2 | 900 | 1 | 290 | | TASI 2014 06 19 112756 | Latisana | 900 | 1 | 320 |
| | TASI 2014 06 12 143541 | Latisana 3 | 900 | 1 | 290 | | TASI 2014 06 19 113357 | Latisana | 900 | 1 | 320 |
| **Flight 3** | TASI 2014 06 12 144122 | Latisana 4 | 900 | 1 | 290 | | TASI 2014 06 21 084135 | Latisana | 900 | 1 | 340 |
| **12/06/2014** | TASI 2014 06 12 144656 | Latisana 5 | 900 | 1 | 290 | | TASI 2014 06 21 084742 | Latisana | 900 | 1 | 340 |
| **Local time** | TASI 2014 06 12 145252 | Latisana 6 | 900 | 1 | 290 | | TASI 2014 06 21 085353 | Latisana | 900 | 1 | 340 |
| | TASI 2014 06 12 145848 | Latisana 7 | 900 | 1 | 290 | | TASI 2014 06 21 090013 | Latisana | 900 | 1 | 340 |
| | TASI 2014 06 12 150500 | Latisana 8 | 900 | 1 | 290 | | TASI 2014 06 21 090631 | Latisana | 900 | 1 | 340 |
| | TASI 2014 06 12 151044 | Latisana 9 | 900 | 1 | 290 | | TASI 2014 06 21 091246 | Latisana | 900 | 1 | 340 |
| | TASI 2014 06 12 151715 | Latisana 10 | 900 | 1 | 290 | | TASI 2014 06 21 091934 | Latisana | 900 | 1 | 340 |
| | TASI 2014 06 13 095400 | Latisana 1 | 900 | 1 | 310 | | TASI 2014 06 21 092608 | Latisana | 900 | 1 | 340 |
| | TASI 2014 06 13 100045 | Latisana 2 | 900 | 1 | 310 | **Flight 10** | TASI 2014 06 21 093213 | Latisana | 900 | 1 | 340 |
| | TASI 2014 06 13 100636 | Latisana 3 | 900 | 1 | 310 | **21/06/2014** | TASI 2014 06 21 093828 | Latisana | 900 | 1 | 340 |
| | TASI 2014 06 13 101157 | Latisana 4 | 900 | 1 | 310 | **UTC time** | TASI 2014 06 21 094556 | Latisana | 900 | 1 | 340 |
| **Flight 4** | TASI 2014 06 13 101742 | Latisana 5 | 900 | 1 | 310 | | TASI 2014 06 21 095222 | Latisana | 1000 | 1 | 340 |
| **13/06/2014** | TASI 2014 06 13 102435 | Latisana 6 | 900 | 1 | 310 | | TASI 2014 06 21 095916 | Latisana | 1000 | 1 | 340 |
| **Local time** | TASI 2014 06 13 103123 | Latisana 7 | 900 | 1 | 310 | | TASI 2014 06 21 101056 | Vineyard | 1000 | 1 | 340 |
| | TASI 2014 06 13 103746 | Latisana 8 | 900 | 1 | 310 | | TASI 2014 06 21 101436 | Vineyard | 1000 | 1 | 340 |
| | TASI 2014 06 13 104451 | Latisana 9 | 900 | 1 | 310 | | TASI 2014 06 21 101907 | Vineyard | 1000 | 1 | 340 |
| | TASI 2014 06 13 105107 | Latisana 10 | 900 | 1 | 310 | | TASI 2014 06 21 102223 | Vineyard | 1000 | 1 | 340 |
| | TASI 2014 06 13 105658 | Latisana 11 | 900 | 1 | 310 | | TASI 2014 06 21 102652 | Vineyard | 1000 | 1 | 340 |
| | TASI_2014_06_13_110315 | Latisana 12 | 900 | 1 | 310 | | TASI_2014_06_21_103029 | Vineyard | 1000 | 1 | 340 |

| | | | | | |
|---|---|---|---|---|---|
| | TASI 2014 06 13 110943 | Latisana 13 | 900 | 1 | 310 |
| | TASI 2014 06 13 111616 | Latisana 14 | 900 | 1 | 310 |
| | TASI 2014 06 13 112255 | Latisana 15 | 900 | 1 | 310 |
| | TASI 2014 06 13 112943 | Latisana 16 | 900 | 1 | 310 |
| | TASI 2014 06 13 113532 | Latisana 17 | 900 | 1 | 310 |
| | TASI 2014 06 13 114211 | Latisana 18 | 900 | 1 | 310 |
| | TASI 2014 06 13 114805 | Latisana 19 | 900 | 1 | 310 |
| | TASI 2014 06 13 115354 | Latisana 20 | 900 | 1 | 310 |
| | TASI 2014 06 13 120027 | Latisana 21 | 900 | 1 | 310 |
| | TASI 2014 06 13 120723 | Latisana 22 | 900 | 1 | 310 |
| | TASI 2014 06 13 121257 | Swimming pool | 900 | 1 | 310 |
| | TASI 2014 06 13 140921 | Latisana 1 | 900 | 1 | 290 |
| | TASI 2014 06 13 141517 | Latisana 2 | 900 | 1 | 290 |
| | TASI 2014 06 13 142134 | Latisana 3 | 900 | 1 | 290 |
| | TASI 2014 06 13 142802 | Latisana 4 | 900 | 1 | 290 |
| **Flight 5** | TASI 2014 06 13 143434 | Latisana 5 | 900 | 1 | 290 |
| **13/06/2014** | TASI 2014 06 13 144134 | Latisana 6 | 900 | 1 | 290 |
| **Local time** | TASI 2014 06 13 144703 | Latisana 7 | 900 | 1 | 290 |
| | TASI 2014 06 13 145716 | Torviscosa 1 | 900 | 1 | 290 |
| | TASI 2014 06 13 150157 | Torviscosa 2 | 900 | 1 | 290 |
| | TASI 2014 06 13 151735 | Spilimbergo 1 | 1000 | 1 | 310 |
| | TASI 2014 06 13 152139 | Spilimbergo 2 | 1000 | 1 | 310 |
| | TASI 2014 06 13 153405 | Swimming pool | 900 | 1 | 310 |
| **Flight 6** | TASI 2014 06 17 101136 | Latisana 1 | 600 | 0.75 | 360 |
| **17/06/2014** | TASI 2014 06 17 101734 | Latisana 2 | 600 | 0.75 | 360 |
| **Local time** | TASI 2014 06 17 102642 | Latisana 3 | 500 | 0.5 | 360 |

| | | | | | |
|---|---|---|---|---|---|
| | TASI 2014 06 21 103416 | Vineyard | 900 | 1 | 340 |
| | TASI 2014 06 21 103710 | Vineyard | 900 | 1 | 340 |
| | TASI 2014 06 21 105022 | Latisana | 900 | 1 | 340 |
| | TASI 2014 06 21 105713 | Latisana | 900 | 1 | 340 |
| | TASI 2014 06 21 110335 | Latisana | 900 | 1 | 340 |
| | TASI 2014 06 21 111011 | Latisana | 900 | 1 | 340 |
| | TASI 2014 06 21 111712 | Latisana | 900 | 1 | 340 |
| | TASI 2014 06 21 112334 | Latisana | 900 | 1 | 340 |
| | TASI 2014 06 21 112935 | Latisana | 900 | 1 | 340 |
| | TASI 2014 06 21 113610 | Latisana | 900 | 1 | 340 |
| | TASI 2014 06 21 142701 | Latisana | 900 | 1 | 320 |
| | TASI 2014 06 21 143926 | Latisana | 900 | 1 | 320 |
| | TASI 2014 06 21 144554 | Latisana | 900 | 1 | 320 |
| **Flight 11** | TASI 2014 06 21 145213 | Latisana | 900 | 1 | 320 |
| **21/06/2014** | TASI 2014 06 21 145855 | Latisana | 900 | 1 | 320 |
| **Local time** | TASI 2014 06 21 150609 | Latisana | 900 | 1 | 320 |
| | TASI 2014 06 21 151223 | Latisana | 900 | 1 | 320 |
| | TASI 2014 06 21 151739 | Latisana | 900 | 1 | 320 |
| | TASI 2014 06 21 152307 | Latisana | 900 | 1 | 320 |

The files have been produced in ENVI format; nevertheless, each data file is identified by an ASCII header file '*.hdr' containing all the info required for opening the data file with a different SW.

All of the 151 files have been delivered radiometrically corrected ($\mu W\ cm^{-2}\ sr^{-1}\ nm^{-1}$), converted into temperature (°K), and geocoded in metric coordinates, UTM 33.

<u>TASI data pre-processing</u>

The TASI calibration and correction process involves both the radiometric calibration and the geometric correction of the images. The data flow of the TASI pre-processing is sketched in Figure 10.
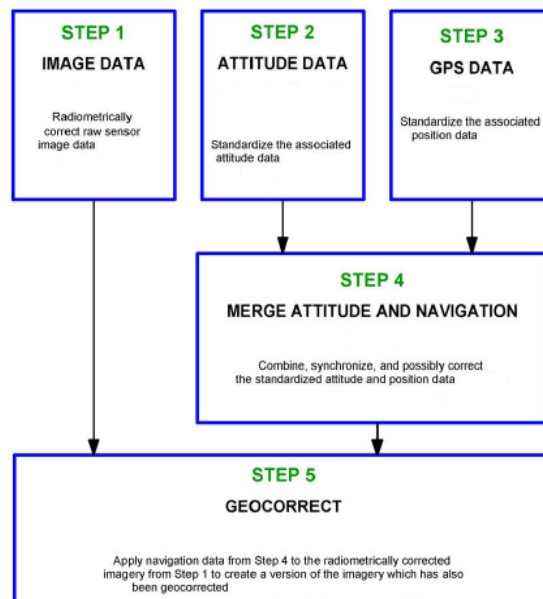


**Figure 10. Five steps pre-processing flow diagram for TASI images.**

**Radiometric calibration**

The radiometric calibration, performed with the ITRES standard processing software, has the general purpose to perform the following tasks on the TASI raw data (i.e. D.N.):

1. Correct: for the additional, non-target-related components in the raw signal;

2. Calibrate: the raw measured DN value for each pixel by multiplying by coefficients generated during the calibration of the instrument. In this way, the data are converted to units of Spectral Radiance. These coefficients are contained within the instrument's calibration files, which are outputted to the sensor calibration run;

3. Scale data: from 14-bit to 16-bit values;

4. Output: TASI image file, in 16-bit unsigned integer, BIP format. The TASI radiance is expressed in **[$\mu W\ cm^{-2}\ sr^{-1}\ nm^{-1}$].**

Moreover, in a further level of pre-processing applied to this Flex activity, three main data artefacts have been minimized to better enhance the further investigation phases after the standard processing of the TASI imagery from the DUCAS campaign in June 2011. The considered artefacts were:

1.  Spectral shift

2.  Unbalanced radiometric (radiance) values between the left and right sides of the imagery (effect of the two slits)

3.  Blinking pixels


*Spectral Shift*

Although the TASI sensor is supported by calibration certification #486  (see above), once the TASI sensor is installed and operates onboard an airborne platform, where the environmental conditions are different from the lab conditions, some slight deviation in the spectrographic alignment can occur. These deviations determine spectral and radiometric artefacts in the processed imagery.

The ITRES standard processing software includes a function to estimate and correct these spectral misalignments on a flightline-by-flightline basis. The value of this kind of correction depends on the specific scene. The shift detection algorithm then computed an incorrect amount of spectral shift of approximately 1 band for some files. The inaccurate shift calculation not only resulted in the image spectra being shifted but also increased the presence of radiometric artefacts, such as unbalanced radiance values, between the two sides of the TASI imagery.

For spectra, the shift artefacts new approaches were investigated that also consider the shutter radiance contribution to the dark, corrected flight-line imagery. The new approaches are less dependent on the specific scene characteristics and allow a better definition of the deviations in the spectrographic alignment.

Figure 11 shows comparisons between MODTRAN simulations (black and blue lines in the left image and right images, respectively) and TASI spectra (red and black lines in the left image and right images, respectively) acquired on a metal panel. Both MODTRAN and TASI spectra depicts the ozone spectral features centred at 9.65 µm (marked by the arrows in both graphs). The left graph of Figure 11 shows the comparison of the TASI spectrum acquired in 2011 and processed using the old calibration chain, which caused a spectral shift with respect to MODTRAN simulation of about one TASI band. This shift was corrected for the FLEX-EU campaign using the new TASI calibration chain. The improvement obtained in the TASI spectral calibration procedure are shown in Figure 11, right.
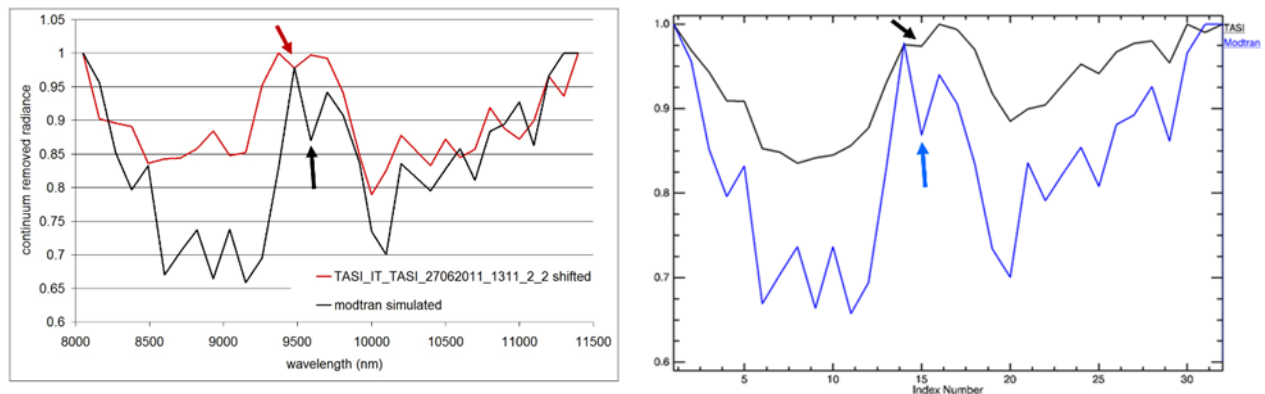
**Figure 11: Left: TASI spectral shift of about one band of magnitude calculated on a TASI imagery acquired on 2011 processed using the old calibration chain. Right: The spectral alignment obtained using the new calibration procedure applied for the FLEX-EU campaign in 2014.**

*Unbalanced radiometric values*

Some of the radiometric artefacts that showed up in the Flex data set were due to the fact that the spectral shift was being incorrectly computed, determining a spectral misalignment between the two slits. Thus, when the spectral shift is more accurately corrected, the presence and severity of radiometric artefacts is reduced.

The following Figure 12 the effects of the radiometric unbalance of the two slits of the TASI-600 sensor is shown. Figure shows a stretched RGB composition image of a flat homogeneous target.
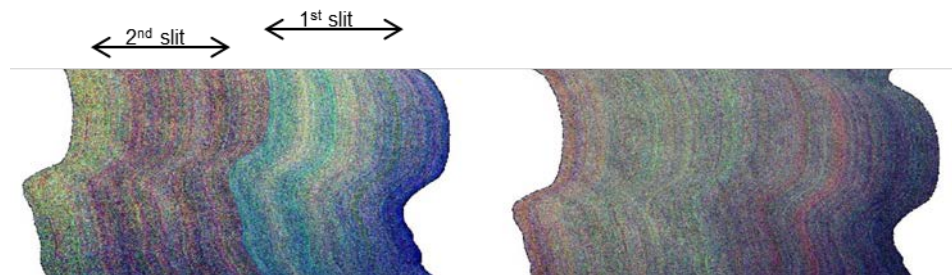


**Figure 12: Effect of the incorrect radiometric unbalance of the two TASI slits as viewed on a homogeneous flat target. Left: standard correction; Right: improved correction minimizing the differences between the slits.**

The correction is applied on a spectral basis so that the incorrect radiometric unbalance of the two slit is minimized for all the TASI wavelengths as shown in Figure 13. The error was measured in term of RMSE between the radiance spectra on different radiance targets (Table 10). However, even with improved shift detection, some small residual radiometric artefacts (left-right unbalance or vertical banding) may appear in the data, especially when it is very complex.
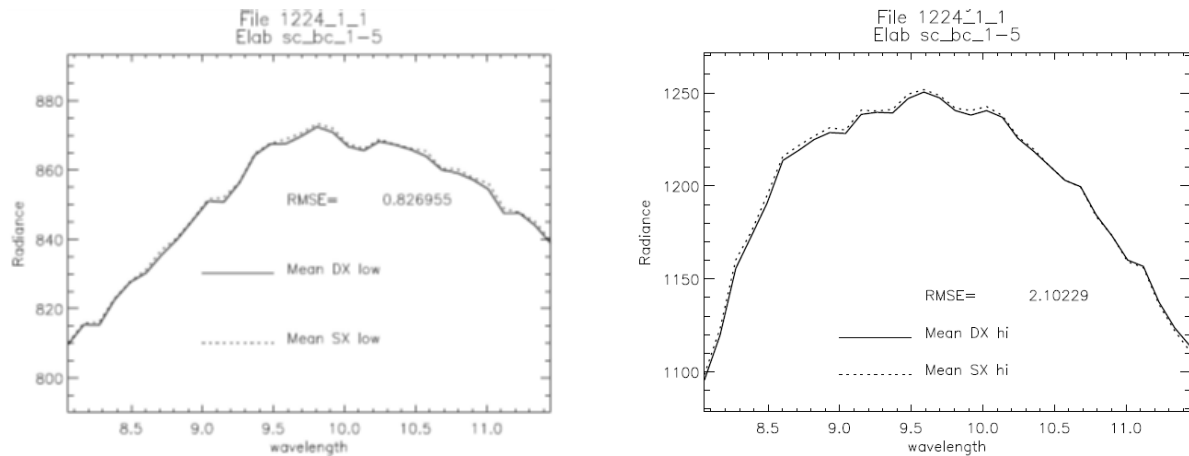
**Figure 13: Radiance spectra of the 1st and the 2nd slit. Left: radiance spectra of a global image, Right: radiance spectra of a high radiance target.**

**Table 10: RMSE calculated on high and low radiance on the overlapping zone of the two slits.**

| | RMSE standard correction | RMSE CNR correction |
|---|---|---|
| Global mean | 1.75 | 0.80 |
| Low radiance values | 1.45 | 0.83 |
| High radiance values | 5.98 | 2.10 |

*Blinking pixels*

Intermittent pixel responses (i.e. blinking pixels - BP) are a known characteristic of thermal infrared Mercury-Cadmium-Telluride (MCT) detectors, such as the type that is used in the TASI sensor. The number of pixels in the MCT array that display this behaviour is generally small. Some are permanently blinking, whereas some pixels will behave normally most of the time but occasionally will show intermittent response variations. For pixels that are consistently defective, they are flagged as 'bad' pixels at the time of lab calibration, and they are interpolated over during the radiometric processing step. Due to the variability in blinking pixels, ITRES had incorporated into the software program the ability to detect and interpolate (either spectrally or spatially) any additional blinking and defective pixels on a flight-line-by-flight-line basis. This correction was originally applied after the data had been radiometrically processed and spectrally resampled. The effect of the BP on the data can be noted by using a RX Anomaly Detection algorithm that will pop up the blinking pixel Figure 14.
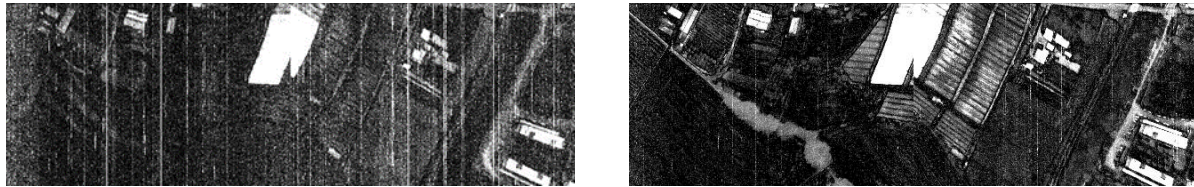
**Figure 14: RX anomaly detection algorithm applied on a TASI resized image. Left image RX output with the defective pixels and lines after the standard BP correction; right image the RX output after have applied the new BP correction.**

Because these approaches also did not adequately resolve the blinking problem, new strategies were defined for the detection and removal of the blinking pixels.

The challenge when developing algorithms to identify blinking pixels is to find the appropriate thresholds for their detection: setting the threshold too high detects and removes too many pixels thereby removing information about the scene and/or removing spectral information from the scene pixels; setting the threshold too low allows some blinking pixels to remain in the imagery, which can complicate certain types of imagery analysis (RX studies). The new strategies performs the blinking pixel detection algorithm earlier on in the processing flow – prior to the radiometric calibration and spectral resampling – to avoid spectral mixing between good and bad pixels. Moreover, the new detection procedures use statistic results obtained by the analysis of both the flight-line imagery and the flight-line shutter (dark) data. This approach better detects specific blinking pixels in the flight line and allows improved results.

**Geometric correction**

The same FLEX-EU configuration was used for the Bundle Adjustment on the Pontecagnano (Italy) airfield. The Bundle Adjustment was made in order to assess the spatial offset between the navigation sensors and the TASI image sensor to account for the geometric correction process. These angle assessments must be determined to achieve an accurate map because the navigation sensors (IMU and GPS antenna) are, in general, not coincident with the sensor's optical centre. The performed Bundle Adjustment process was applied to determine the sensor orientation computing the six sensor offset parameters (i.e. three position and three altitude offset parameters).

The position errors calculated for the Bundle Adjustment over Pontecagnano are expressed in RMS, and they are 0.832 m, 0.614 m, and 1.389 m respectively for longitude, latitude, and elevation.

The geometric correction of the images is performed in a sequence of four steps based on retrieving the altitude and GPS data from the raw file, synchronizing it with respect to the sensor frames acquisitions, differentiating the GPS, and merging all this information in the navigational file describing the precise trajectory of the TASI sensor's centre of mass.

The altitude processing is finalized to create a pre-processed altitude data file that will then become the data input for the navigational file. The procedure is applied via the following steps:

- extract the raw POS data directly from the PC card – 'flash' card;

- extract real-time altitude and navigation data. The key files extracted are the real-time POS NovAtel GPS data and the real-time navigation data files. The real-time POS altitude solution may be directly inputted to *attsync*, or optionally this file may be:

- post-processed to increase the quality of the downstream geo-corrected output image file.

The second stage of processing the POS data altitude is to synchronize it with the imagery data. This was done by:

- estimating the offset between sensor time and GPS time;

- applying the time offset;

- inserting POS altitude data into the navigational file: roll, pitch, and heading;

- extracting the GPS data and applying a post-processing correction with respect to the base station provided by the SIT of Friuli Venezia Giulia Region, which is located close to the flying area (i.e. Cervignano and Bevazzana).

The third step of processing before geometric correction consists of merging the processed altitude data and navigation data. This is possible because the altitude and imagery data are already time synchronized and the time offset between sensor time and GPS time has previously been estimated.

The final step in the standard processing is the geometric correction, which corrects image data created by TASI into an UTM geographic coordinate grid using a nearest neighbour algorithm. The geometric correction applied to the TASI data set takes into account: (a) changes in the position and altitude of the sensor head during data acquisition; (b) the linear and angular offsets among the instrument sensor head, the IMU, and the GPS antenna; and (c) variations in terrain height by utilizing the DEM at 10 m of GSD provided by the SIT of Friuli Venezia Giulia Region.

Concerning the FLEX-EU TASI deployment, the geometric correction procedure was configured with square pixels (i.e. 1 x 1 m or 0.75 x 0.75 m and 0.50 x 0.50 m of GSD according to the flight altitude) in the output images.

**Atmospheric correction and temperature retrieval**

The standard pre-processing procedures implemented in the ENVI 5 software (Excelis, Boulder, CO, USA) were then applied for executing the atmospheric correction and temperature-emissivity separation.

Atmospheric correction of spectral radiances was performed by applying the in-scene atmospheric compensation (ISAC) algorithm (Young, *et al.* 2002) that requires only the calibrated, at-sensor radiance data to estimate the upwelling radiance and transmissivity of the atmosphere by solving Equation (1):

$$L_{obs} = \tau B(T) + L_u$$

where, $L_{obs}$ is the observed at-sensor radiance, $\tau$ is transmission of the atmosphere, *B(T)* is the Planck function, and $L_u$ is the upwelling radiance from the atmosphere. The algorithm assumes that two pixels in the scene are black bodies for which neither the locations nor the temperatures are known (Vaughan *et al.*, 2003). The ISAC algorithm is suitable when the variables that characterize the atmospheric radiative conditions are not available during the acquisition time, as in our case. For our study, we used the 'most

hits' method as described by Johnson (1998), in which pixels that have the maximum brightness temperature are then used as the reference wavelength (Gu *et al.*, 2000).

Once the images were atmospherically corrected, the 'emissivity normalization routine' (Vaughan *et al.*, 2003) method was used to separate temperature and emissivity to retrieve the temperature for the acquired TASI imagery. The emissivity normalization technique calculates the temperature for every pixel and band in the data using a fixed emissivity value. The highest temperature for each pixel is then used to calculate the emissivity values using the Planck function.

The main limitation of the entire procedure is that it assumes atmospheric homogeneity in the environment under analysis. This could lead to incomplete removal of strong atmospheric effects that affect the LWIR region, in particular the strong absorptions related to $O_3$ (9.6–9.8 μm) and other minor absorptions resulting from $SO_2$ (8.5–9.0 μm) and $CO_2$ (9.5–9.8 and 10.3–10.8 μm).

**TASI Data Quality**

*Geometric accuracy*

To assess the geometric accuracy of the TASI images in the overlapping the data set, a reference fixed target common to all the images was selected. In particular, a metal rooftop of a building located on Latisana TASI imagery (see Figure 15) was identified to check the TASI images geometric accuracy. The metal roof was selected as it assures a good precision of detection because of its low emissivity causing a high contrast with respect to the background. The Geometric Data Quality corresponds to the total RMS in localization of the NE roof edge (the position is indicated by the red arrow in Figure 15) as identified on the Google Earth reference image and on the TASI images.

TASI geocoding procedure has allowed the overlapping among the 22 images of the entire data set an accuracy of about 1 pixel corresponding to the GSD of 1. In particular, for the Latisana data set the RMS values are $X_{error}$ = 1.01 m and $Y_{error}$ = 0.84 m.
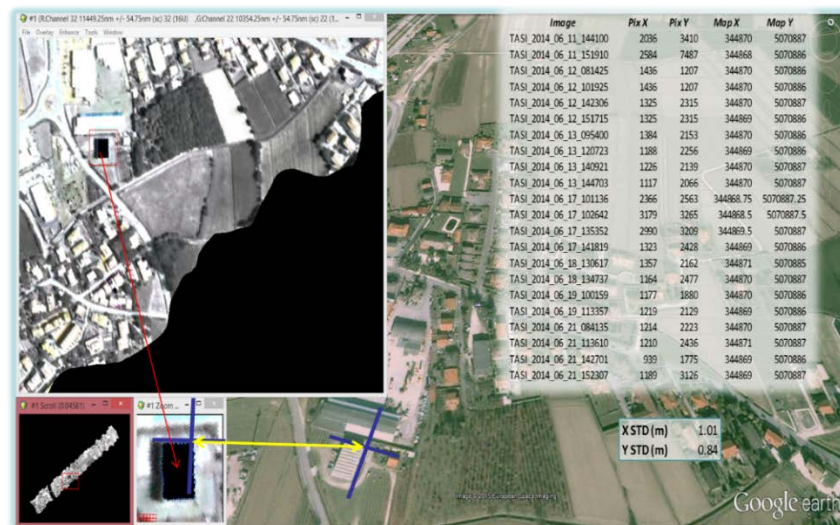
**Figure 15. TASI geometric accuracy estimation using the RMS between the metal roof edge on TASI images and Google Earth reference imagery.**

*TASI temperature retrieval accuracy*

To validate the TASI temperature, derived by applying the procedure described above (see 'Atmospheric correction and Temperature retrieving'), we used the ground, true temperature acquired from a swimming pool using a thermocouple acquired at the same date and time by TASI imagery (i.e. file TASI_2014_06_12_102449). For TASI imagery, the mean value of the inner pixels relative to the water of the pool (used to avoid border-effects, i.e. mixed pixels) was calculated and shows a difference of less than 0.5 K (as showed in Figure 16) with respect to the measured ones.
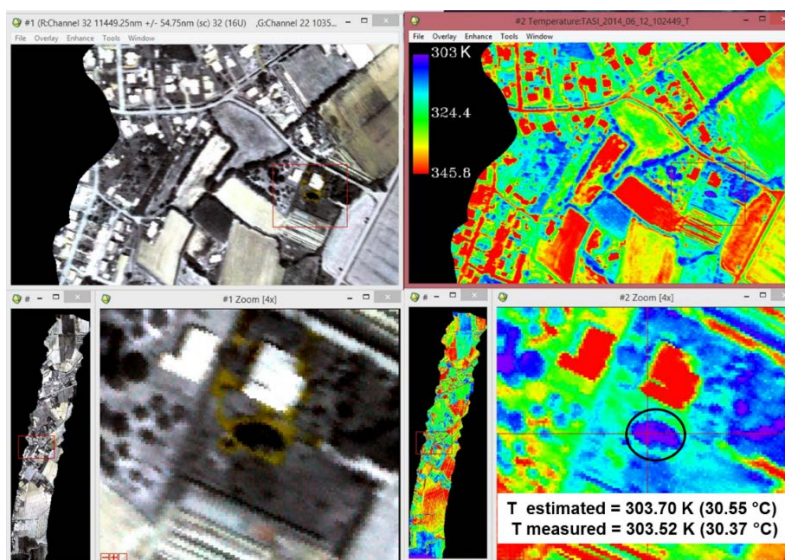


**Figure 16. TASI temperature accuracy assessed by comparing the TASI temperature and field measured temperature acquired on the same time and date.**

Each TASI images, recorded for the Latisana treatment experiment, were transformed in temperature to detect the thermal temporal behaviour of the different plots. The temperature maps recorded in parallel to the *HyPlant* overpasses are shown in Figure 17. The temperature is an integrated measure while radiance is spectral, and therefore possibly radiance could be more sensitive to detected spectral variations.

Considering that the ISAC atmospheric correction algorithm, retrieves atmospheric parameters from the image itself (transmission and upwelling radiance are estimated from the image), eventual residual errors in the temperature retrieval can be related to the extreme variability of atmosphere conditions (cloud covers) occurred within some days of flights. Therefore, the obtained temperatures represent an accurate assessment of the plots temperature behaviour, in accordance to the TASI-600 sensor' characteristics.

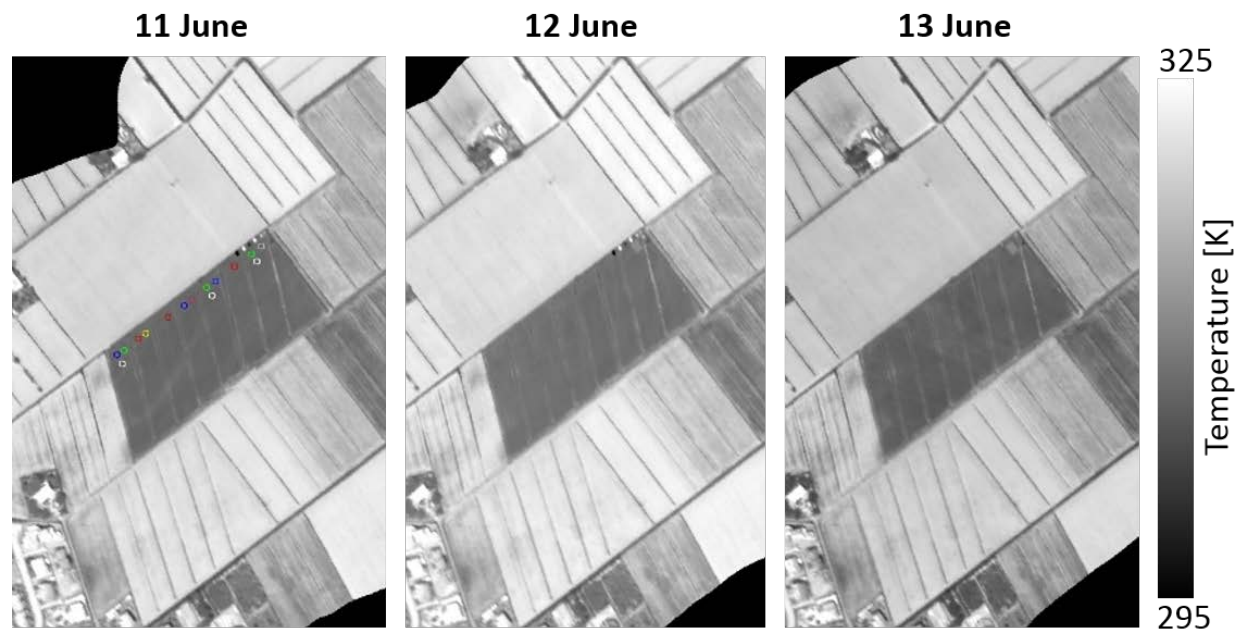**11 June**   **12 June**   **13 June**



**Figure 17: Temperature maps of Latisana treatment experiment. TASI images were recorded in parallel to the *HyPlant* overpasses. Coloured circles in the first temperature map indicate the plots of the Latisana treatment experiment.**

## 4.2 Spectral ground and reference measurements

During this FLEX-EU campaign a network of dedicated and specialized ground measuring facilities was operated throughout the campaign windows. Those data were used as reference and for further analyses of the airborne data.

### 4.2.1 Spectral reference measurements

A mobile team equipped with a calibrated spectrometer operating in the spectral range from the visible to the shortwave infrared measured various surface calibration/validation targets. Natural 'pseudo-invariant' features at the site and artificial targets specifically placed into the flight lines were used as calibration/validation (cal/val) targets. Pseudo-invariant surfaces were for concrete. Three artificial targets (black, white, and grey; Figure 18) have been placed into the flight lines.



**Figure 18: Artificial calibration/validation targets for ground reference measurements.**

Target reflectance was measured by recording: (i) incoming radiation using a white reference calibrated panel (Labsphere Inc., U.S.A.); (ii) upwelling radiation from the surface.

Target optical properties were acquired with the portable spectroradiometer Fieldspec 4 (ASD Inc., USA) (serial number 18068) operating in the 350–2500 nm spectral range. A Spectralon Labsphere was used as white reference (serial number 51340-1-14). Spectra were acquired in raw digital numbers over the targets and over the Spectralon white reference panel.

Twenty measurements were taken in order to characterize each target with the sampling scheme shown in Figure 19; each number corresponds to the location of each acquisition. The Spectralon white reference was mounted on a levelled tripod as shown in Figure 19 B; the white reference spectra were acquired every five target measurements. Reflectance was then calculated in post-processing, normalizing each target spectrum for the average of two white reference spectra acquired before and after five target measurements. Reflectance was then multiplied by the Spectralon calibration file. The

tripod, white reference, and operators were positioned towards north to avoid shadow on the observed areas.

The Fieldspec was set to acquire an average of twenty-five spectra for dark current, white reference, and sample. An example of reflectance spectra of concrete, the white, grey and black tarp, are presented in Figure 20.
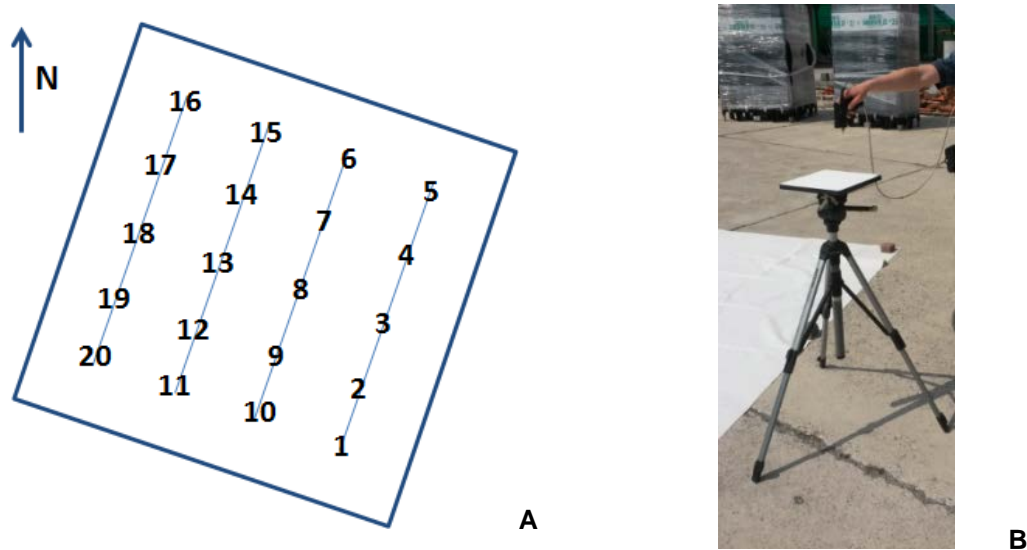


**Figure 19: A) Measurement scheme used on each target. Each number corresponds to the location of each measure. B) White reference mounted on a levelled tripod.**
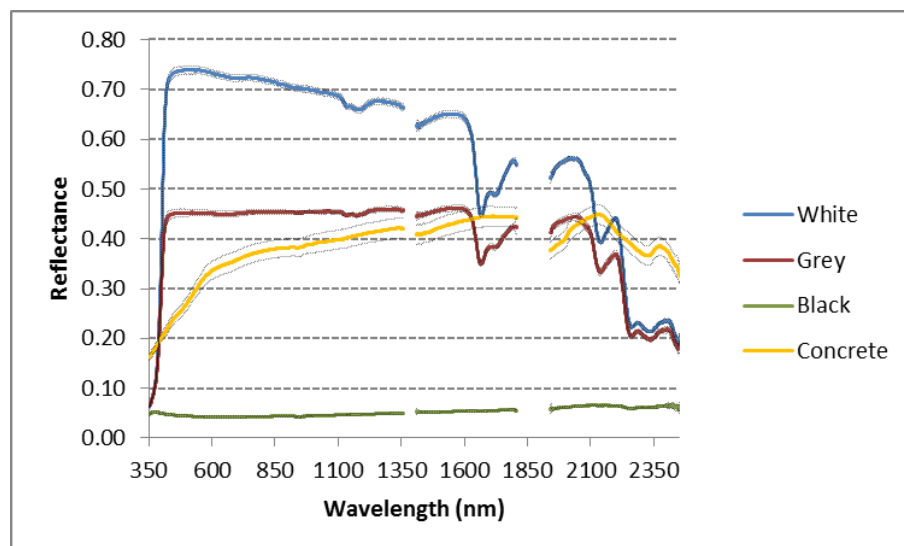


**Figure 20: Reflectance spectra of three artificial calibration/validation targets (white, grey, and black tarp) and a pseudo-invariant target (concrete). Coloured lines represent the average of 20 single measurements and the dotted lines the standard deviation. Data were recorded on 12 June 2014.**

### 4.2.2 Top-of-canopy spectral measurements of reflectance and sun-induced fluorescence

Top-of-canopy, high-resolution radiance spectra were collected simultaneously with three spectrometers covering different spectral ranges:

i) a spectrometer HR4000 (OceanOptics, USA) operating in the visible and near infrared (400–1000 nm) spectral range with a full width at half maximum (FWHM) of 1 nm allows the computation of incident irradiance, visible to near-infrared reflectance and different vegetation indices;

ii) a spectrometer HR4000 (OceanOptics, USA) covering the 700–800 nm spectral range with a finer resolution (FWHM = 0.15 nm). This spectrometer is specifically designed for sun-induced fluorescence measurements in the oxygen absorption band $O_2$-A positioned at 760 nm ($F_{760}$);

iii) a third OceanOptics spectrometer (model QE 65000) operating in the 657–740 nm spectral range with a FWHM of 0.25 nm was used to measure sun-induced fluorescence at the $O_2$-B absorption band.

Bare fibre optics with a field of view (FOV) of 25° have been used alternatively to measure a white reference calibrated panel (Labsphere Inc., U.S.A.) and the grass targets. The grass targets were measured from nadir at a height above the ground of 130 cm, corresponding to a sampling area of about 60 cm diameter. Measurements were collected during *HyPlant* overpasses (1 hour before and 1 hour after).

Ocean Optics spectrometers were housed in a Peltier thermally regulated box (model NT-16, Magapor, Zaragoza, Spain) keeping the internal temperature at 25 °C in order to reduce dark current drift.

The three spectrometers were spectrally calibrated with known standards (CAL-2000 mercury argon lamp, OceanOptics, USA) while the radiometric calibration has been inferred from cross-calibration measurements performed with a reference calibrated FieldSpec spectrometer (Analytical Spectral Device, USA). The experimental set-up is shown in Figure 21.

**Figure 21: Experimental setup used to collect high-resolution spectral measurements over the grassland plots.**

The S-FLUO box is designed for high-temporal-frequency acquisition of continuous radiometric measurements. This system is based on a commercial, optical multiplexer (MPM-2000, OceanOptics, USA), able to switch between a channel measuring the incident irradiance (cosine response optic), a downward-looking bare fibre (FOV of 25°) for the measurement of the upwelling radiance, and a 'blind' channel for the dark current measurement and hosts two portable spectrometers (HR4000, OceanOptics, USA) operating in the visible and near-infrared region but with different spectral resolution. The first one covers the 400–1000 nm spectral range with a FWHM of 1 nm and allows the computation of vegetation indexes. The second one covers with a finer resolution (FWHM = 0.2 nm) a restricted spectral range (670–860 nm) and is specifically intended for sun-induced fluorescence measurements in the $O_2$-A absorption band. Spectrometers were spectrally calibrated with known standards (CAL-2000 mercury argon lamp, OceanOptics, USA) while the radiometric calibration was inferred from cross-calibration measurements performed with a reference calibrated FieldSpec spectrometer (ASD, USA). The S-FLUO box was installed on a 40-meters-tall Eddy Covariance tower at the Bílý Kříž study site, over a 17-meter-tall homogeneous spruce forest (*Picea abies* (L.) Karst.). The downward-looking bare fibres were mounted on a 3-meter-long arm perpendicular to the tower, approximately facing north to minimize the shadowing effect. The exact position of the arm was chosen to take care of avoiding major gaps of the forest canopy.

Collected data were processed with a specifically developed IDL (ITTvis IDL 7.1.1®) application that allowed the basic processing steps of raw data necessary for the computation of the reflectance factors:

- correction for CCD detector non linearity;
- correction for dark current and dark current drift;
- wavelength calibration and linear resampling;
- radiance calibration;
- incident radiance computation by linear interpolation of two white reference measurements and correction for the known white reflectance.

A set of quality criteria described in (Meroni *et al.* 2011) has been applied for automatic data selection in order to reject poor-quality data due to unfavourable meteorological conditions (e.g. clouds, rain or fog).

Different spectral indexes were computed from the top-of-canopy reflectance spectra. The fluorescence in the far-red region ($F_{760}$) was estimated using the spectral fitting methods described in Meroni and Colombo (2006) and in Meroni *et al.* (2010), assuming a linear variation of reflectance and fluorescence in the $O_2$-A absorption band region. The spectral interval used for $F_{760}$ estimation was set to 759.00 to 767.76 nm for a total of 439 spectral channels. Fluorescence in the red region ($F_{687}$) was estimated at the $O_2$-B band by using an improved version of spectral fitting methods (Cogliati *et al.*, 2015), that uses piecewise cubic spline and Voigt spectral functions to represent canopy reflectance and fluorescence, respectively, in the spectral range between 684 and 696 nm, for a total of 200 spectral channels.

## 4.3 Correlative ground measurements: Characterization of the structural and functional status of vegetation using canopy level methods

Especially during the Italy campaign, a network of dedicated correlative ground measurements were conducted. Those data are used as reference and for further analyses of the airborne data.

### 4.3.1 Leaf chlorophyll content

There were seven Eppendorf tubes per plot, with 3-5 leaves were randomly sample within one treatment plot. The plastic tubes were immediately stored in liquid nitrogen and later transferred into a -80 °C freezer for long-term storage. The chlorophyll content was extracted later in the lab.

The extraction of chlorophyll a and chlorophyll b was carried out using 100% acetone buffered with magnesium hydroxide carbonate ($\sim 4MgCO_3 \cdot Mg(OH)_2 \cdot 5H_2O$), hereafter referred to as acetone.

The 1000 ml of acetone was mixed with 20 g of magnesium hydroxide carbonate and the mixture was cooled to 4 °C until used. For extraction, the punched and frozen leaf discs were transferred into new 2-ml Eppendorf tubes (Safe Lock) and 200 µl of acetone was added. The sample was filled to 1–5 ml. The tube was stored on ice until they could be centrifuged at 13000 rpm for 5 minutes at 4 °C. The excess solution was measured in the photometer. The spectrophotometric measurements were carried out in a glass cuvette at wavelengths of 470 nm, 645 nm, 662 nm, and 710 nm.

$$Chl\,a = [11{,}24 \cdot (A_{662} - A_{710}) - 2{,}04 \cdot (A_{645} - A_{710})] \cdot \frac{\alpha}{\beta} \tag{22}$$

$$Chl\,b = [20{,}13 \cdot (A_{645} - A_{710}) - 4{,}19 \cdot (A_{662} - A_{710})] \cdot \frac{\alpha}{\beta} \tag{23}$$

*Chl*:     Chlorophyll content (mg/g fresh weight)

$A_{662}$:     reading at 662 nm (Absorption maximum of Chlorophyll a)

$A_{645}$:     reading at 645 nm (Absorptions maximum of Chlorophyll b)

$A_{710}$:     reading at 710 nm (no absorption of pigments, reference)

α:     Volume of extract (5 ml)

β:     leaf area of the probe (g)

## 4.3.2 Eddy covariance measurements

Two fully equipped flux towers were installed in the field site of Latisana (Figure 22). Each station consisted of a sonic anemometer (Metek, D), an open-path gas analyser (Li7500, licor, Nebraska) measuring CO2 and $H_2O$ concentrations at high frequency data (10 Hz). The synchronized data were acquired on a laptop using proprietary software. Flux data were calculated using the EddyPro software package to estimate the net ecosystem $CO_2$ exchange rate (NEE), the latent and sensible heat fluxes (LE and H) as well as the momentum flux u* and $CO_2$-exchange rate. C-flux partitioning was made according to the standard Fluxnet methodology to estimate the Gross Primary Productivity (GPP) and Ecosystem Respiration (Reco). Half-hourly fluxes were computed and stored.



**Figure 22: View of one of the two flux towers installed in Latisana (Italy) that operated throughout the field campaign.**

Ancillary measurements included half-hour means of net radiation (Rebs Q7, Campbell Sci. USA) shortwave and longwave, incoming and outgoing radiation (CNR1, Campbell Sci. Australia), soil heat flux (G), air and soil temperatures that were acquired using thermocouples and coated thermistors. Continuous measurements of net $CO_2$ ecosystem exchange rates were acquired during the campaigns to derive GPP. GPP time series might be used to investigate the link between photosynthesis and TOC sun-induced fluorescence.

### 4.3.3 Gas-exchange chamber measurements

*Description of the chamber system*

The closed dynamic (non-steady-state flow-through) chamber system was used in order to estimate $CO_2$ and $H_2O$ fluxes from the experimental plots (Figure 23). The *net ecosystem exchange* (*NEE*) and the *ecosystem respiration* (*Reco*) were derived directly from measurements using a transparent and an opaque chamber, respectively. The transparent chamber was made from 3 mm thick Plexiglas® (Evonik Industries, Darmstadt, Germany), as this material has a high solar radiation transmittance (ca 90%; Chojnicki *et al.* 2010, Hoffman *et al.* 2015). The opaque chamber was made from 3 mm thick white PVC to ensure dark conditions. Both chambers had dimensions of 78x78x50 cm and a total volume of 0.296 m$^3$. The chambers were fixed on square PVC collars (0.75 x 0.75m) installed in each experimental plot with an insertion depth of 5 cm. Twelve soil frames were installed on 5th of June 2014 at the main experimental area. The next nine frames were installed on the external Kaolin and Vapor Gard experiment in the middle of the field. All frames were levelled at the day of installation.



**Figure 23: Closed, dynamic-chamber system used for measurements of $CO_2$ fluxes.**

During the measurement, the air inside the chamber was mixed using three computer fans (1.4 W each) installed in the chamber. Air temperature was measured with radiation-shielded thermistor (T-107, Campbell Scientific, USA). None cooling devices were used (as described in Chojnicki *et al.* 2010) in order to not reduce $H_2O$ fluxes due to condensation. The air was circulated at approximately 2.5 L min$^{-1}$ between the chamber and a portable control box containing an infrared gas analyzer (LI-840, LICOR, USA), which measured $CO_2$ and $H_2O$ concentration in the air connected to a bypass flowing through the analyzer at 0.7 L min$^{-1}$. Readings of gases concentration and air temperature were recorded every 5 seconds on a data logger (CR-1000, Campbell Sci., USA).

*Protocol of measurements*

The opaque chamber was closed for 120 seconds during measurements, while the closure time of transparent chamber varied from 120 seconds in the morning to 40 seconds at noon and afternoon in order to avoid chamber overheating. In case of transparent chamber, the closure time was shortened if the within-chamber air temperature raised more than 1.5 °C and the variability of the measured PAR was higher than 10% of the value recorded at the beginning of the measurement. In order to avoid overheating of the chamber and temperature probe in the period between measurements, the transparent chamber was covered with a white reflective material.

NEE measurements were taken just after reflectance and SIF measurements on the same plots. Reco measurements followed the NEE estimations (measurements were taken no more than one minute after NEE chamber was removed from the plot)

The flux measurements started on 7 June and were continued till 20 June 2014. In the period between 7 and 11 June, measurements were carried out on all 12 plots. Starting from the 12 June, measurements

were carried out on selected plots exposed for different treatments. Each day measurements started in the early morning and were continue till late afternoon. Frequency of measurements at each plot and number of fluxes was different each day and depend on the campaign schedule.

In order to monitor environmental conditions during the campaign and chamber measurements and correlate the measured fluxes with PAR and temperature, meteorological measurements of soil temperature at 2 cm depth, air temperature at 30 cm height and PAR were carried out automatically at the provisionally installed climate station (in the middle of the site). Additionally, soil temperature probes (T-107, Campbell Scientific, USA) were installed next to the frames at the depth of 2 cm in order to refer the respiration fluxes to soil temperature.

### *Data processing and fluxes calculation*

In order to avoid errors related to changes in water vapor concentration in the chamber headspace over the closure time, the measured $CO_2$ concentrations were corrected for water dilution effect using equation:

$$C(t) = \frac{C(t)^{'}}{1 - w/1000} \qquad (24)$$

where $C(t)$ is the mole fraction of $CO_2$ ($\mu mol \cdot mol^{-1}$) in dry air, $C(t)'$ is the measured $CO_2$ mole fraction ($\mu mol \cdot mol^{-1}$) in wet air and $w$ is the measured mole fraction of water vapor ($mmol \cdot mol^{-1}$) measured by LI-840 gas analyzer (LI-COR Application Note 129, Perez-Priegoet *et al.* 2015). Afterwards, all data were visually inspected and data noise originating from disturbances caused by chamber deployment and possible saturation and canopy microclimate effects were discarded (according to Davidson *et al.* 2002, Hoffman et al. 2015).

$CO_2$ and $H_2O$ fluxes were calculated based on a gas concertation changes over the closure time using the linear regression type as described in Juszczak *et al.* 2013. Fluxes were calculated from the first 30 – 40 seconds of measurements for data with the highest regression slopes in order to avoid underestimation of the fluxes due to e.g. gas saturation, in accordance with Hoffmann et al. 2015. The gas flux ($F$) from the chambers in $\mu mols\ m^{-2}$ per certain time unit ($t$) was calculated from the gas concentration change in the chamber headspace $\frac{\Delta C}{\Delta t}$, the chamber volume ($V$) and enclosed soil area ($A$) using the equation:

$$F = \frac{\Delta C}{\Delta t} \cdot \frac{V}{A \cdot M_v} \qquad (25)$$

where $M_v$($m^3 \cdot mol^{-1}$) is the molar volume of air at the chamber air temperature and pressure. The determination coefficient was calculated for each time series and if $r^2 < 0.9$ the fluxes were discarded and not considered in the analyses.

Gross Primary Productivity (GPP), indicating the amount of $CO_2$ assimilated by plants in photosynthesis, was calculated as the difference between Reco and NEE taken consecutively with both chambers.

# 5  Campaign sites and activities

FLEX-EU campaign activities in 2014 consisted of three campaigns:

- Germany campaign:          25 May to 07 June 2014 (chapter 5.1)
- Italy Campaign:            11 to 26 June 2014         (chapter 5.2)
- Czech Republic campaign:   10 to 20 July 2014         (chapter 5.3)
                             04 to 06 September

A detailed description of the acquired data on each measurement day can be found in the DAR [RD-7].

## 5.1  Germany

Two experimental sites were covered during the flight campaign in Germany; both are located in the anthropogenically influenced agricultural area around Jülich (Figure 24 and Figure 25, Table 11-Table 13) and the agricultural experimental Campus Klein-Altendorf (Figure 26, Table 13). Both sites were already recorded during the 2012 and 2013 campaigns (see HYFLEX final report [RD-5]) and mapping of these sites was continued in 2015 and 2016. Thus, the data set of this campaign is imbedded in a continuous annual data set of high resolution fluorescence and reflectance data of these two experimental sites in Germany.

### 5.1.1  Anthropogenic, agricultural area around Jülich

The agricultural experimental sites around Jülich (Figure 24 and Figure 25, Table 11-Table 13) are research sites associated with the Transregional Collaborative Research Centre 32: Patterns in Soil-Vegetation-Atmosphere Systems: Monitoring, Modelling, and Data Assimilation (TR32; www.tr32.de) and located in the Rur catchment. It can be described as an anthropogenically influenced area consisting of a variety of different vegetation types, including agricultural fields, grasslands, meadows, and small forest patches.

**Figure 24: Large map of the agricultural area around Jülich (TR32 map).**

**Table 11: Flight lines of the large agricultural map around Jülich (TR32 map) with a spatial resolution of 2.5 x 2.5 m per pixel.**

| Flight | Start | | End | | Altitude |
|---|---|---|---|---|---|
| line | lat | long | lat | long | [m] |
| fluomap_1 | 50.901088 | 6.290447 | 50.90109 | 6.290447 | 1860 |
| fluomap_2 | 50.901088 | 6.301827 | 50.90109 | 6.301827 | 1860 |
| fluomap_3 | 50.901088 | 6.313207 | 50.90109 | 6.313207 | 1860 |
| fluomap_4 | 50.901088 | 6.324587 | 50.90109 | 6.324587 | 1860 |
| fluomap_5 | 50.901088 | 6.335967 | 50.8884 | 6.335967 | 1860 |
| fluomap_6 | 50.901088 | 6.347347 | 50.8884 | 6.347347 | 1860 |
| fluomap_7 | 50.901088 | 6.358727 | 50.8884 | 6.358727 | 1860 |
| fluomap_8 | 50.901088 | 6.370107 | 50.83375 | 6.370107 | 1860 |
| fluomap_9 | 50.901088 | 6.381487 | 50.83375 | 6.381487 | 1860 |
| fluomap_10 | 50.901088 | 6.392867 | 50.83375 | 6.392867 | 1860 |
| fluomap_11 | 50.901088 | 6.404247 | 50.83375 | 6.404247 | 1860 |
| fluomap_12 | 50.901088 | 6.415627 | 50.83375 | 6.415627 | 1860 |
| fluomap_13 | 50.901088 | 6.427007 | 50.83375 | 6.427007 | 1860 |
| fluomap_14 | 50.901088 | 6.438387 | 50.83375 | 6.438387 | 1860 |
| fluomap_15 | 50.901088 | 6.449767 | 50.83375 | 6.449767 | 1860 |
| fluomap_16 | 50.901088 | 6.461147 | 50.83375 | 6.461147 | 1860 |
| fluomap_17 | 50.889027 | 6.472527 | 50.83375 | 6.472527 | 1860 |
| fluomap_18 | 50.883353 | 6.483907 | 50.83375 | 6.483907 | 1860 |

**Figure 25: Flight lines of the Selhausen/Merzenhausen area.**

**Table 12: Flight lines of the large map of the Selhausen/Merzenhausen area with a spatial resolution of 1 x 1 m per pixel.**

| Flight | Start | | End | | Altitude [m] |
|---|---|---|---|---|---|
| line | lat | long | lat | long | |
| MEZ_L1 | 50.933708 | 6.288913 | 50.922000 | 6.311543 | 790 |
| SEL_L4 | 50.881712 | 6.448185 | 50.840693 | 6.463043 | 790 |
| SEL_L5 | 50.880555 | 6.444651 | 50.839403 | 6.459409 | 790 |
| SEL_L6 | 50.879737 | 6.441037 | 50.838782 | 6.455585 | 790 |

## 5.1.2 Agricultural research campus Klein-Altendorf

The agricultural research campus Klein-Altendorf near Bonn comprises 181 ha for field trials and approximately 4,800 m² for Greenhouse trials. On Campus Klein-Altendorf, research can be conducted with all kinds of plants and crops, ranging from small plants like *Arabidopsis* or herbs to large crops like maize, from annual crops like vegetables to perennial plants like *Miscanthus* or fruit trees. Plants can be grown in the experiments under practical conditions.
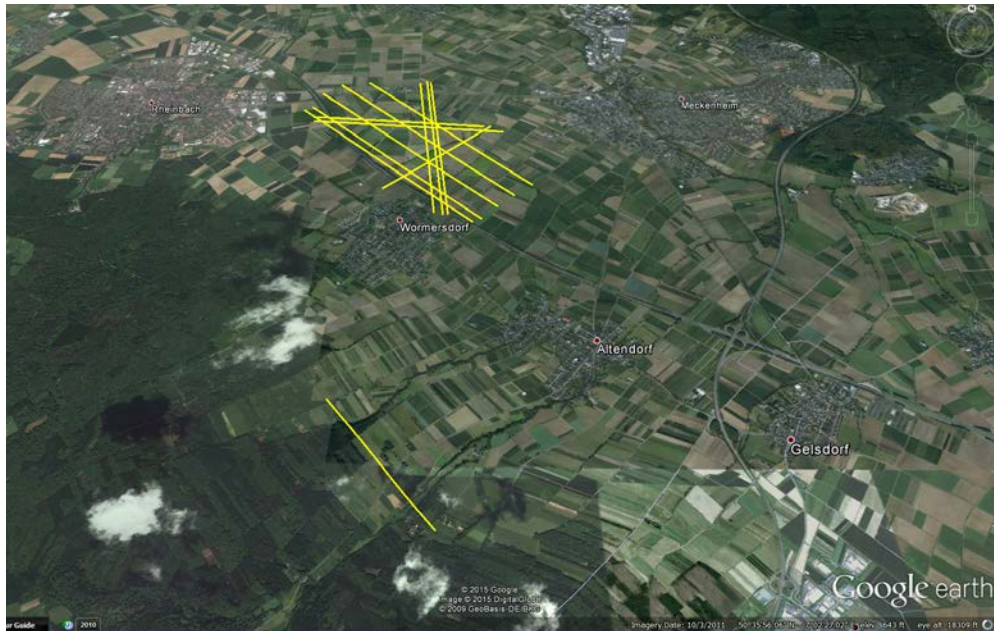


**Figure 26: Flight lines of the Kleinaltendorf area.**

**Table 13: Flight lines of the Kleinaltendorf area with a various spatial resolution.**

| Flight line | Start long | lat | End long | lat | Altitude [m] | Spatial resolution [m] |
|---|---|---|---|---|---|---|
| L1_map_2014 | 6.981846 | 50.629918 | 7.007524 | 50.612125 | 865 | 1 x 1 |
| L2_map_2014 | 6.977155 | 50.629450 | 7.004941 | 50.610518 | 865 | 1 x 1 |
| L3_map_2014 | 6.974344 | 50.627800 | 7.002542 | 50.608937 | 865 | 1 x 1 |
| L4_map_2014 | 6.973288 | 50.625199 | 7.000324 | 50.607192 | 865 | 1 x 1 |
| L9_Hilberath_Lukas | 6.983482 | 50.586796 | 6.996177 | 50.576264 | 960 | 1 x 1 |
| L5_Vera | 6.986152 | 50.611529 | 7.001587 | 50.621806 | 520 | 0.5 x 1 |
| L6_ZG | 6.9739 | 50.62332 | 7.000552 | 50.62177 | 520 | 0.5 x 1 |
| L7_ZR | 6.974148 | 50.62258 | 7.003493 | 50.62086 | 520 | 0.5 x 1 |
| L8_Tim | 6.991064 | 50.6302 | 6.995003 | 50.60775 | 520 | 0.5 x 1 |
| L9_Hilberath_Lukas | 6.983482 | 50.586796 | 6.996177 | 50.576264 | 620 | 0.5 x 1 |
| L10_Miscantus1 | 6.972134 | 50.62463 | 6.999126 | 50.60676 | 520 | 0.5 x 1 |

| L11_Miscantus2 | 6.973288 | 50.625199 | 7.000324 | 50.607192 | 520 | 0.5 x 1 |
|---|---|---|---|---|---|---|
| L12_Apfelbäume | 6.991686 | 50.63002 | 6.995693 | 50.60782 | 520 | 0.5 x 1 |
| L13_Apfelbäume2 | 6.98999 | 50.62982 | 6.993752 | 50.60803 | 520 | 0.5 x 1 |

### 5.1.3  Data acquired in Germany 2014

A summary of the airborne data acquired during the campaign in Germany is given in Table 14. The table summarizes the date of the recording, the start and end time of the data acquisition in local time, the total number of flight lines recorded for the experimental area. Furthermore, the table indicates if there were any sensor failures or problems, gives an indication of the cloud conditions during the recording, and summarizes if ground reference measurements for calibration validation purposes are available for the acquired flight lines.

**Table 14: Data acquired during campaign in Germany 2014.**

| Date | Start | End | No. flight lines | Area | *HyPlant* performance | Cloud cover (okta) | ASD Reference (Cal/Val) |
|---|---|---|---|---|---|---|---|
| 25 May | 11:02 | 11:44 | 11 | Klein-Altendorf (CKA) | OK | 3/8 | Lat: 50.615172° Long: 6.992587° |
| 25 May | 12:49 | 12:56 | 4 | Selhausen (SEL)/ Merzenhausen (MEZ) | OK | 2/8 | Lat : 50.870300° Long: 6.451330° |
| 28 May | 10:13 | 10:45 | 14 | Klein-Altendorf (CKA) | OK | 3/8 | Lat: 50.615172° Long: 6.992587° |
| 31 May | 13:08 | 14:24 | 19 | Klein-Altendorf (CKA) | OK | 3/8 | Lat: 50.615172° Long: 6.992587° |
| 31 May | 10:26 | 12:47 | 22 | Jülich (TR32 map) | OK | 3/8 | Lat : 50.870300° Long: 6.451330° |
| 2 June | 10:23 | 11:43 | 13 | Jülich (TR32 map) | OK | 6/8 | No |
| 6 June | 14:18 | 14:43 | 4 | Selhausen (SEL)/ Merzenhausen (MEZ) | OK | 1/8 | No |
| 6 June | 11:49 | 14:01 | 21 | Jülich (TR32 map) | OK | 2/8 | No |

## 5.2  Italy

### 5.2.1  Vineyard site with different soil properties

This area was selected because a major soil intervention was made involving the large-scale application of biochar that may have affected both the background soil colour, albedo, and fertility. W with possible consequences on plant vigour and the carbon uptakes rates of the vineyard and of the grassland vegetation growing among the rows (Figure 27, Table 15).
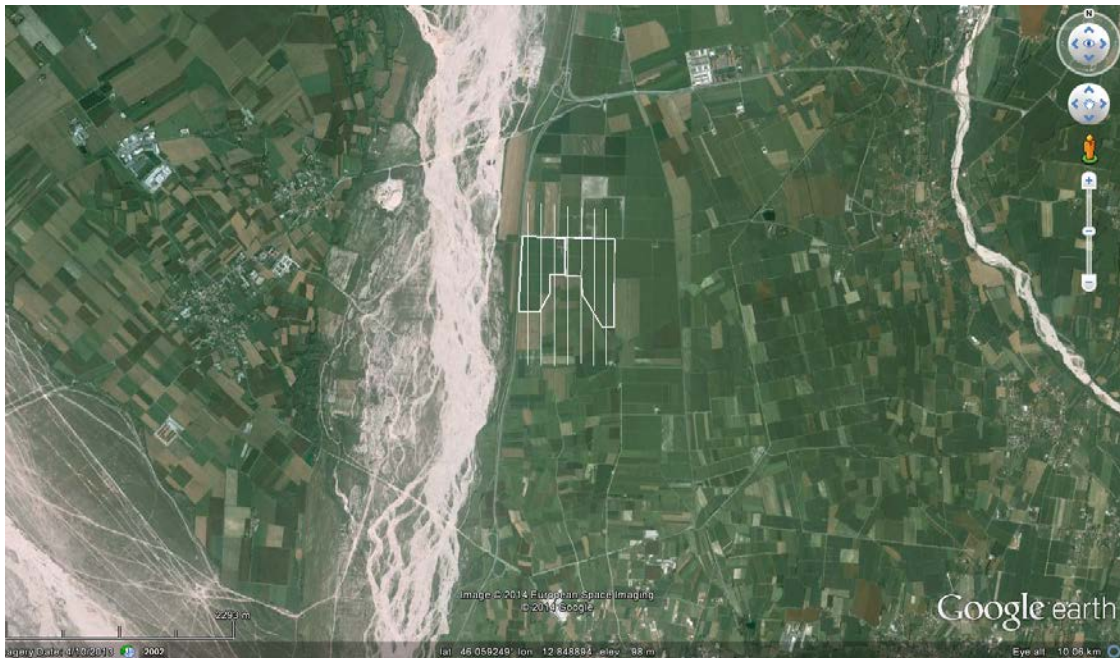


**Figure 27: Flight lines of the vineyard experimental site.**

**Table 15: Flight lines of the vineyard experimental site with a spatial resolution of 0.5 x 1m.**

| Flight line | Start long | lat | End long | lat | Altitude [m] |
|---|---|---|---|---|---|
| V1 | 12.82824 | 46.07189 | 12.82824 | 46.08605 | 390 |
| V2 | 12.82669 | 46.08601 | 12.82663 | 46.07182 | 390 |
| V3 | 12.82504 | 46.08611 | 12.82498 | 46.07196 | 390 |
| V4 | 12.82325 | 46.08618 | 12.82323 | 46.07186 | 390 |
| V5 | 12.82145 | 46.08635 | 12.82142 | 46.07172 | 390 |
| V6 | 12.81973 | 46.08652 | 12.81973 | 46.07183 | 390 |
| V7 | 12.81801 | 46.08663 | 12.81797 | 46.07188 | 390 |

### 5.2.2  Carlino farm

This area was selected to evaluate how different land uses (crops) modify solar-induced fluorescence. The area is used for extensive agriculture. The lack of consistent homogeneity in the crop cover allows

the simultaneous evaluation of the overall fluorescence signal and its magnitude in a complex mosaic of soil/vegetation components (Figure 28, Table 16). The area also includes a large, mixed-forest area of 143 ha. The forest comprises *Quercus robur, Carpinus betulus, Fraxinus oxycarpa, Ulmus minor* and some *Acer campestris* and *Fraxinus ornus*. The understorey consists of shrubs of *Corylus avellana, Clematis vitalba, Crataegus monogyna e C. oxyacantha, Prunus spinosa, Lonicera xylosteum, Hedera elix, Ruscus aculeatu, Cornus mas e C. sanguinea, Daphne mezereum, Ligustrum vulgare,* and *Viburnum opulus e V. lantana.* During the set-up of this 'mixed pixel experiment', it became clear that the crops on the Carlino farm were not suitable for the experimental set-up. Therefore, the experiment was moved to a grassland spot (see also chapter 5.2.3).
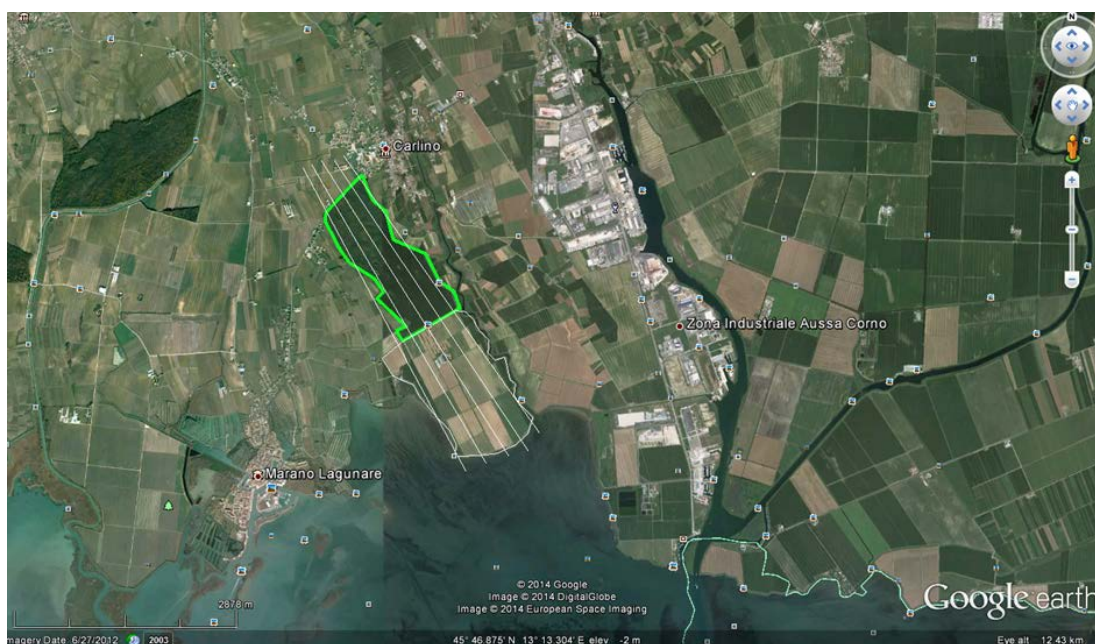


**Figure 28: Flight lines of the Carlino experimental Farm.**

**Table 16: Flight lines of the Carlino experimental Farm**

| Flight | Start | | End | | Altitude |
|---|---|---|---|---|---|
| line | long | lat | long | lat | [m] |
| C1 | 13.181133 | 45.801436 | 13.213831 | 45.769161 | 730 |
| C2 | 13.179595 | 45.800891 | 13.211921 | 45.767124 | 730 |
| C3 | 13.177476 | 45.80082 | 13.208667 | 45.766524 | 730 |
| C4 | 13.175863 | 45.800331 | 13.204926 | 45.765641 | 730 |
| C5 | 13.174401 | 45.799966 | 13.201561 | 45.764716 | 730 |

### 5.2.3 Latisana site

The Latisana experimental site is a homogeneous grassland (turf) site. The area belongs to a private company that specializes in the production and commercialization of 'rolling turfs' that are raised on very homogeneous soils and manage to maintain higher productivity and the most appropriate plan density. The turf, which is composed of a mixture of *Lolium perenne* and *Poa pratensis* are fully fertilized and periodically irrigated to avoid the occurrence of nutrient limitations and water shortages. Two main experiments took place in this side: (i) the treatment experiment; and (ii) the mixed-pixel experiment (Figure 29, Table 17).



**Figure 29: Flight lines Latisana field site including treatment and mixed-pixel experiment.**

**Table 17: Flight lines of the Latisana field site.**

| Flight | Start | | End | | Altitude |
|---|---|---|---|---|---|
| line | long | lat | long | lat | [m] |
| T1 | 13.02795 | 45.78655 | 12.99202 | 45.76705 | 730 |
| M3 | 13.02097 | 45.82292 | 13.04244 | 45.78076 | 730 |
| M4 | 13.01706 | 45.79275 | 13.07311 | 45.80381 | 730 |

### 5.2.3.1 Airborne acquisition

A summary of the airborne data acquired during the campaign in Italy is given in Table 18. The table summarizes the date of the recording, the start and end time of the data acquisition in local time, the total number of flight lines recorded for the experimental area. Furthermore, the table indicates if there were any failures or problems with the *HyPlant* and TASI sensor, gives an indication of the cloud conditions during the recording, and summarizes if ground reference measurements for calibration validation purposes are available for the acquired flight lines.

**Table 18: Data acquired during campaign in Italy 2014.**

| Date | Start | End | No. flight lines | Area | *HyPlant* performance | TASI performance | Cloud cover (okta) | ASD Reference (Cal/Val) |
|---|---|---|---|---|---|---|---|---|
| 11 June | 11:42 | 12:11 | 6 | Carlino Farm (CAR) | OK | OK | 3/8 | No |
| 11 June | 14:52 | 15:06 | 3 | Latisana (LAT, treatment) | OK | OK | 3/8 | 45°46'28.69"N, 13°0'16.56"E |
| 11 June | 15:14 | 15:35 | 5 | Carlino Farm | OK | OK | 1/8 | No |
| 11 June | 15:42 | 15:48 | 2 | Latisana (LAT, treatment) | OK | OK | 3/8 | 45°46'28.69"N, 13°0'16.56"E |
| 12 June | 10:21 | 15:17 | 38 | Latisana (LAT, treatment) | Oversaturation in some pixels | OK | 1/8 | 45°46'28.69"N, 13°0'16.56"E |
| 13 June | 09:56 | 14:41 | 30 | Latisana (LAT, treatment) | OK | OK | 1/8 | 45°46'28.69"N, 13°0'16.56"E |
| 18 June | 15:08 | 15:48 | 7 | Latisana (LAT, treatment) | OK | OK | 5/8 | No |
| 19 June | 11:32 | 11:56 | 5 | Latisana (MIX, mixed pixel) | OK | OK | 1/8 | 45°47'42.85"N, 13°2'7.08"E |
| 19 June | 12:02 | 13:34 | 16 | Latisana (LAT, treatment) | OK | OK | 2/8 | No |
| 21 June | 10:42 | 16:23 | 31 | Latisana (LAT, treatment) | OK | OK | 4/8 (cirrus) | 45°46'39.35"N, 13°0'45.60"E |
| 21 June | 12:12 | 12:34 | 7 | Vinyard (VIN) | OK | OK | 1/8 | No |
| 22 June | 12:10 | 12:57 | 8 | Latisana (LAT, treatment) | OK | No flight | 3/8 | No |
| 24 June | 10:33 | 11:56 | 15 | Latisana (LAT, treatment) | OK | No flight | 3/8 | 45°46'28.69"N, 13°0'16.56"E |
| 26 June | 09:56 | 14:36 | 16 | Latisana (LAT, treatment) | OK | No flight | 2/8 | 45°46'28.69"N, 13°0'16.56"E |
| 26 June | 11:00 | 11:41 | 7 | Carlino Farm (CAR) | OK | No flight | 2/8 | No |

## 5.3 Czech Republic

The experimental sites of Bílý Kříž in the Czech Republic was already covered as part of the HYFLEX 2012 campaign [RD-5]. Data acquisition was repeated in 2014 over the same area (Figure 30–Figure 32; Table 19–Table 21). A third mapping of this area was performed in 2016; therefore, every two years a data set of this forested site is available. In addition, the experimental site of Štítná was recorded as well. This was already planned for 2012 and made-up for in the FLEX-EU 2014 campaign flight

### 5.3.1 Spruce forest experimental site in Bílý Kříž

The spruce forest experimental research site of Bílý Kříž site is located in the Moravian-Silesian Beskydy Mountains in the eastern part of the Czech Republic, bordering the Slovak Republic (49.50194°N, 18.53667° E, 880 m above sea level). The experimental site was established in 1986 and is recently being used for the monitoring of energy and substances fluxes using eddy covariance technique and the evaluation of carbon pools in mountain forest ecosystems. The Bílý Kříž site is part of the CzechGlobe infrastructure (http://www.czechglobe.cz/en/) and serves as an experimental site for ecosystem monitoring. Many types of continuous/discrete measurements have been carried out there for more than 15 years (e.g., GHG and energy fluxes, water balance, carbon stock in vegetation and soil, biomass inventory, tree transpiration flow, nitrogen inputs, etc.). The site is equipped with power supply, a meteorological station covering basic micrometeorological measurements, and an EC tower (49.50222° N; 18.53683° E) where additional equipment can be installed. The climate of the area is characterised by an annual mean temperature of 5.5 °C, annual mean relative air humidity of 80%, and a total rainfall of 1000–1400 mm. The spruce forest experimental site is covered by a 35-year-old regular plantation of Norway spruce *(Picea abies (L.) Karst)* growing on a moderate slope (13°) with S-SE orientation. The geological bedrock is formed by Mesozoic Godula sandstone (flysch type) with ferric podzols.
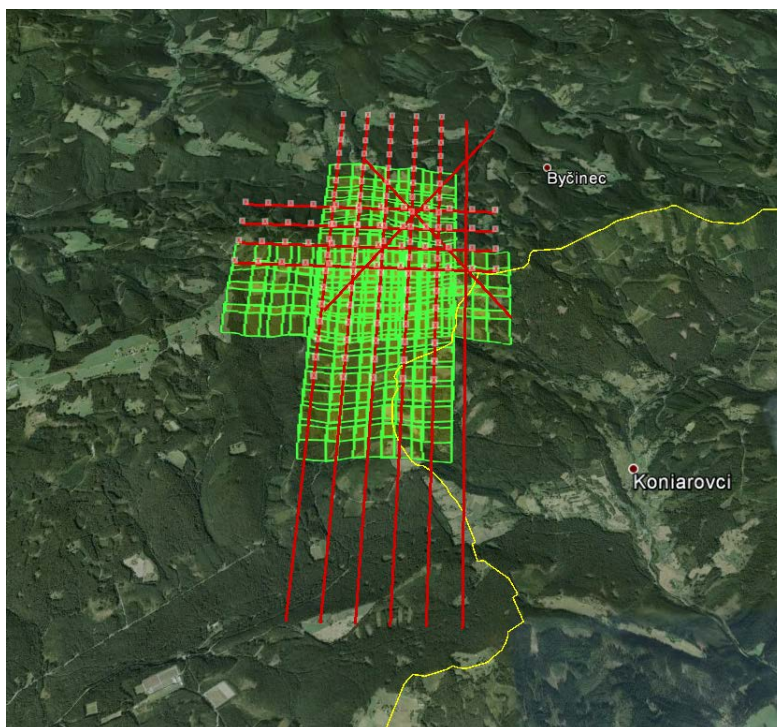
**Figure 30: Flight lines of the spruce forest experimental site in Bílý Kříž site with a spatial resolution of 1 x 1 m.**

**Table 19: Flight lines of the spruce forest experimental site in Bílý Kříž with a spatial resolution of 1 x 1 m.**

| Flight line | Start long | lat | End long | lat | Altitude [m] |
|---|---|---|---|---|---|
| BK 1 | 18.54086 | 49.46359 | 18.54453 | 49.51389 | 1540 |
| BK 2 | 18.53743 | 49.4637 | 18.5411 | 49.51399 | 1540 |
| BK 3 | 18.52405 | 49.4641 | 18.5277 | 49.5144 | 1540 |
| BK 4 | 18.52737 | 49.464 | 18.53102 | 49.5143 | 1540 |
| BK 5 | 18.53069 | 49.4639 | 18.53434 | 49.5142 | 1540 |
| BK 6 | 18.534 | 49.4638 | 18.53766 | 49.5141 | 1540 |
| BK 7 | 18.51569 | 49.50273 | 18.54729 | 49.50175 | 1540 |
| BK 8 | 18.53047 | 49.5087 | 18.54816 | 49.48992 | 1540 |
| BK 9 | 18.52625 | 49.49061 | 18.54819 | 49.51249 | 1540 |
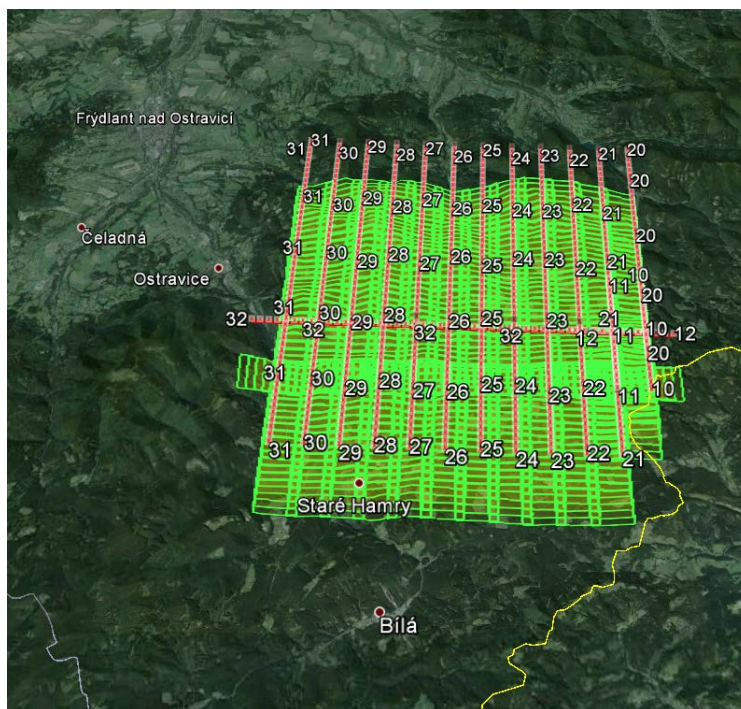
**Figure 31: Flight lines of the spruce forest map in Bílý Kříž with a spatial resolution of 3 x 3 m.**

**Table 20: Flight lines of the spruce forest map in Bílý Kříž with a spatial resolution of 3 x 3 m.**

| Flight | Start | | End | | Altitude |
|---|---|---|---|---|---|
| line | long | lat | long | lat | [m] |
| BKh 1 | 18.53704 | 49.48352 | 18.53921 | 49.51405 | 2620 |
| BKh 2 | 18.52648 | 49.48384 | 18.52864 | 49.51437 | 2620 |
| BKh 3 | 18.51542 | 49.49927 | 18.54708 | 49.4983 | 2620 |
| BKh 4 | 18.53773 | 49.49291 | 18.54233 | 49.55666 | 2620 |
| BKh 5 | 18.52527 | 49.46721 | 18.53175 | 49.55698 | 2620 |
| BKh 6 | 18.51471 | 49.46753 | 18.52111 | 49.5573 | 2620 |
| BKh 7 | 18.50409 | 49.46785 | 18.51053 | 49.55763 | 2620 |
| BKh 8 | 18.49353 | 49.46817 | 18.49995 | 49.55795 | 2620 |
| BKh 9 | 18.48297 | 49.46849 | 18.48931 | 49.55827 | 2620 |
| BKh 10 | 18.47235 | 49.46881 | 18.47873 | 49.55859 | 2620 |
| BKh 11 | 18.46179 | 49.46912 | 18.46814 | 49.55891 | 2620 |
| BKh 12 | 18.45123 | 49.46944 | 18.45751 | 49.55923 | 2620 |
| BKh 13 | 18.44061 | 49.46975 | 18.44692 | 49.55954 | 2620 |
| BKh 14 | 18.43005 | 49.47007 | 18.43634 | 49.55986 | 2620 |
| BKh 15 | 18.41948 | 49.47038 | 18.4257 | 49.56017 | 2620 |
| BKh 16 | 18.41056 | 49.50242 | 18.5442 | 49.49839 | 2620 |

## 5.3.2 Beech forest experimental site in Štítná

Štítná beech forest is an experimental research site located near the village of Štítná in the White Carpathians Mts. (Czech Republic, 17°58'N, 49°02'E, altitude 560 m a.s.l.). The research site is covered by 80-year-old *European beech (Fagus sylvatica (L.))* trees. The site's geological subsoil is represented mainly by sandstone. The mean annual temperature is about 6 °C, and an average precipitation about 800 mm per year, and annual cloudiness of 65%. The experimental site is equipped with a meteorological station measuring basic climatologic parameters and an eddy covariance measurement system.
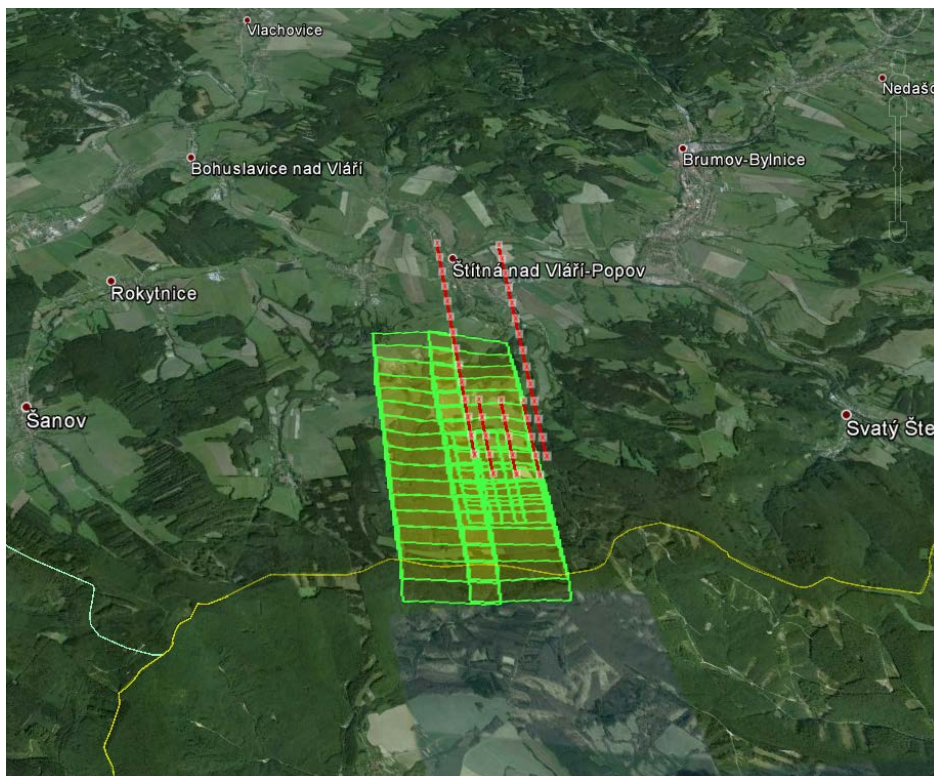


**Figure 32: Flight lines of the Štítná beech forest site.**

**Table 21: Flight lines of the Štítná beech forest site.**

| Flight | Start | | End | | Altitude |
|---|---|---|---|---|---|
| line | long | lat | long | lat | [m] |
| ST1 | 17.96723 | 49.04083 | 17.96677 | 49.03115 | 1150 |
| ST2 | 17.97057 | 49.04076 | 17.97005 | 49.03107 | 1150 |
| ST3 | 17.9739 | 49.04068 | 17.97338 | 49.03099 | 1150 |
| STh1 | 17.9616 | 49.05309 | 17.95992 | 49.02479 | 2230 |
| STh2 | 17.97091 | 49.05285 | 17.96922 | 49.02455 | 2230 |

### 5.3.3 Data acquired in Czech Republic 2014

A summary of the airborne data acquired during the campaign in Czech Republic is given in Table 22.

The table summarizes the date of the recording, the start and end time of the data acquisition in local time, the total number of flight lines recorded for the experimental area. Furthermore, the table shows if there were any sensor failures or problems during the recording. It also gives an indication of the cloud conditions during the recording and summarizes if Microtops measurements and ground reference measurements for calibration validation purposes are available for the acquired flight lines.

**Table 22: Data acquired during campaign in Czech Republic 2014.**

| Date | Start | End | No. flight lines | Area | *HyPlant* performance | Cloud cover (okta) | Microtops | ASD Reference (Cal/Val) |
|---|---|---|---|---|---|---|---|---|
| 19 July | 10:05 | 11:19 | 15 | Bílý Kříž (BK) | OK | 3/8 | Lat: 49.50254 Long: 18.53857 | Lat: 49.49951 Long: 18.54218 |
| 19 July | 11:52 | 12:33 | 6 | Štítná (ST) | OK | 3/8 | | Lat: 49.08296 Long: 18.01943 |
| 20 July | 09:57 | 10:19 | 4 | BK high | OK | 8/8 | Lat: 49.50254 Long: 18.53857 | Lat: 49.49951 Long: 18.54218 |
| 20 July | 10:48 | 10:53 | 2 | Štítná high | OK | 3/8 | | Lat: 49.08296 Long: 18.01943 |
| | | | | | | | | |
| 5 Sept | 10:14 | 11:45 | 30 | BK high | OK | 4/8 | Lat: 49.46761 Long: 18.43272 | Lat: 49.56191 Long: 18.42648 |

# 6 Results

## 6.1 Mapping of study sites

In the following chapters, we present true colour images, vegetation indices, and fluorescence maps of the anthropogenic, agricultural area around Jülich (Figure 34 - Figure 36) and the experimental Campus Klein-Altendorf (Figure 37, Figure 38) in Germany. Furthermore, the different vegetation maps of data acquired during the Italian campaign are presented; the vineyard site with different soil amendments (Figure 39, Figure 40), the Carlino experimental farm (Figure 41, Figure 42); and the Latisana site with the treatment and mixed-pixel experiment (Figure 44, Figure 45). For the Czech Republic, vegetation and fluorescence maps of the Spruce forest site of Bílý Kříž (Figure 45, Figure 46) and beech forest site (Figure 47, Figure 48) have been delivered to ESA; however, no further analyses of those vegetation maps are provided within this report. Fluorescence maps of the agricultural sites around Jülich were calculated using the iFLD method. Fluorescence maps of forest areas in Czech Republic could only be derived using the SVD method. Due to missing reference surfaces the iFLD method is not applicable and the hilly mountain terrain is not included in the SFM retrieval yet.

### 6.1.1 Anthropogenic, agricultural area around Jülich



**Figure 33: True colour map (R: 156, G: 105, B: 51) of the anthropogenic area around Jülich (TR32 map) recorded on 6 June 2014.**
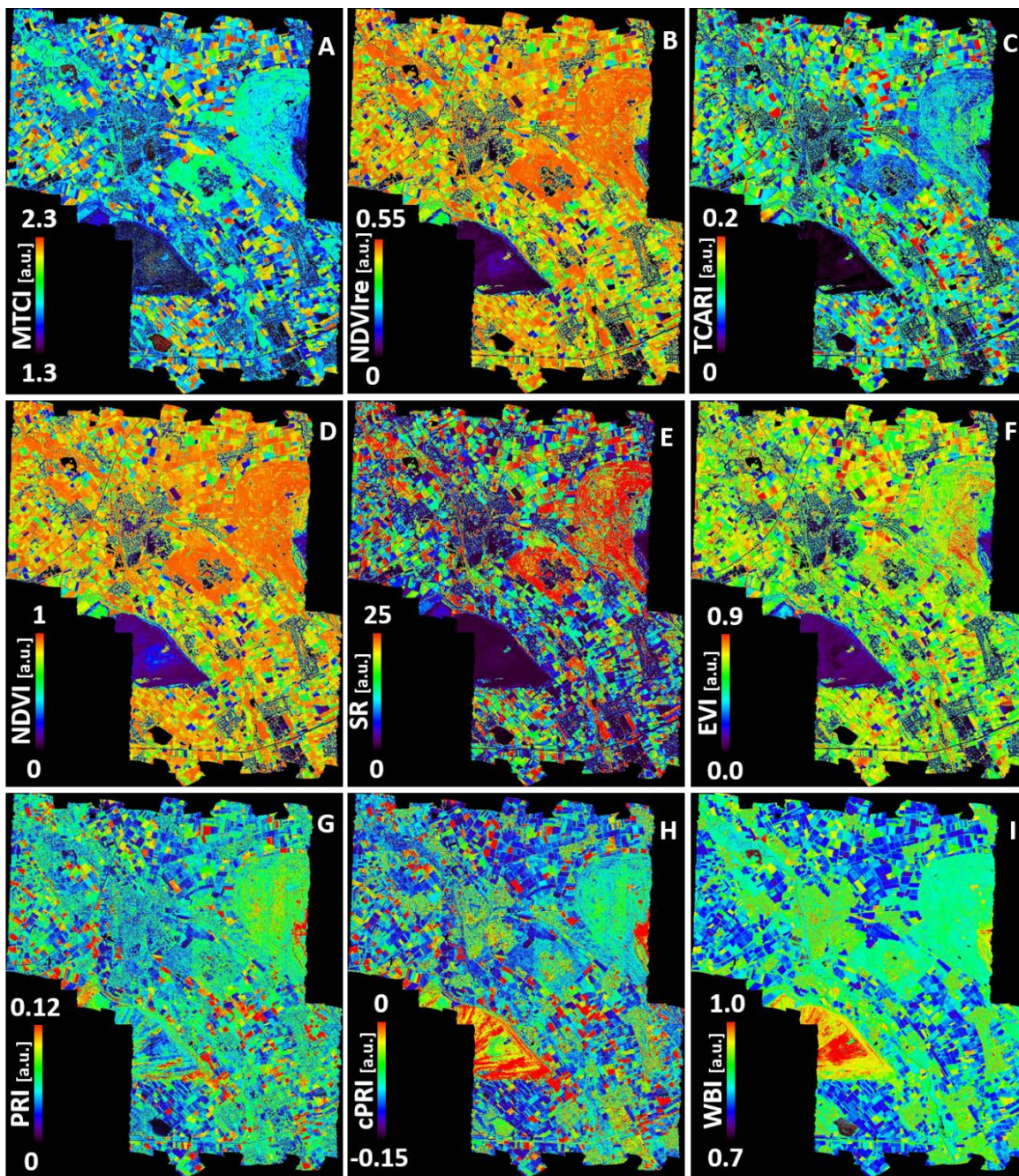
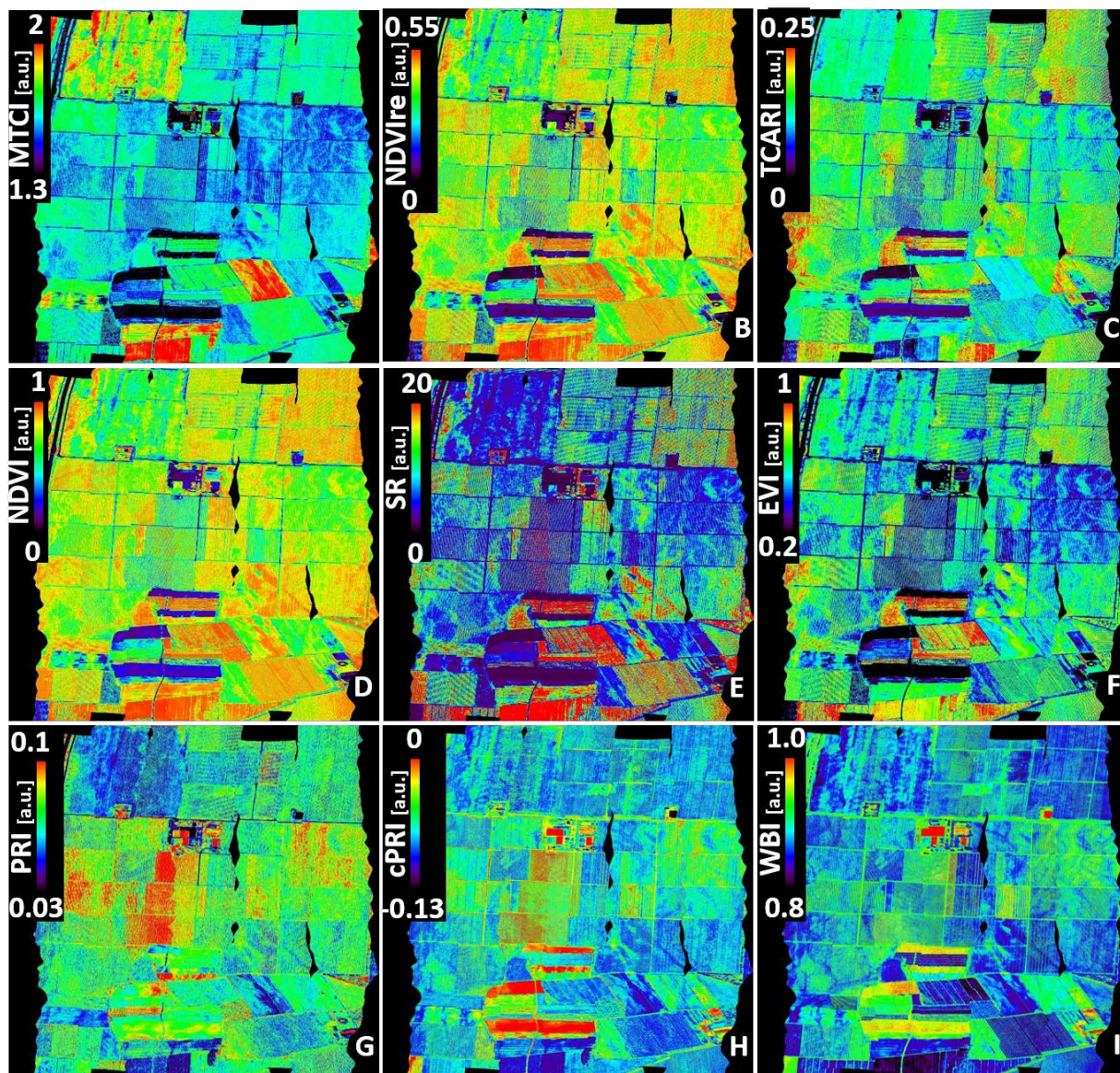**Figure 34: Maps of the anthropogenic, agricultural area around Jülich (TR32 map) showing different vegetation indices: MERIS terrestrial chlorophyll index (MTCI) (A); red-edge Normalized Difference Vegetation Index (NDVIre) (B); Transformed Chlorophyll Absorption Reflectance Index (TCARI) (C); Normalized Difference Vegetation Index (NDVI) (D); Simple Ratio (SR) (E); Enhanced Vegetation Index (EVI) (F); Photochemical Reflectance Index (PRI) (G); canopy Photochemical Reflectance Index (cPRI) (H); and Water Band Index (WBI) (I). Data were recorded on 6 June 2014.**

**Figure 35: True colour map (R: 156, G: 105, B: 51) of the anthropogenic area around Selhausen recorded on 6 June 2014.**
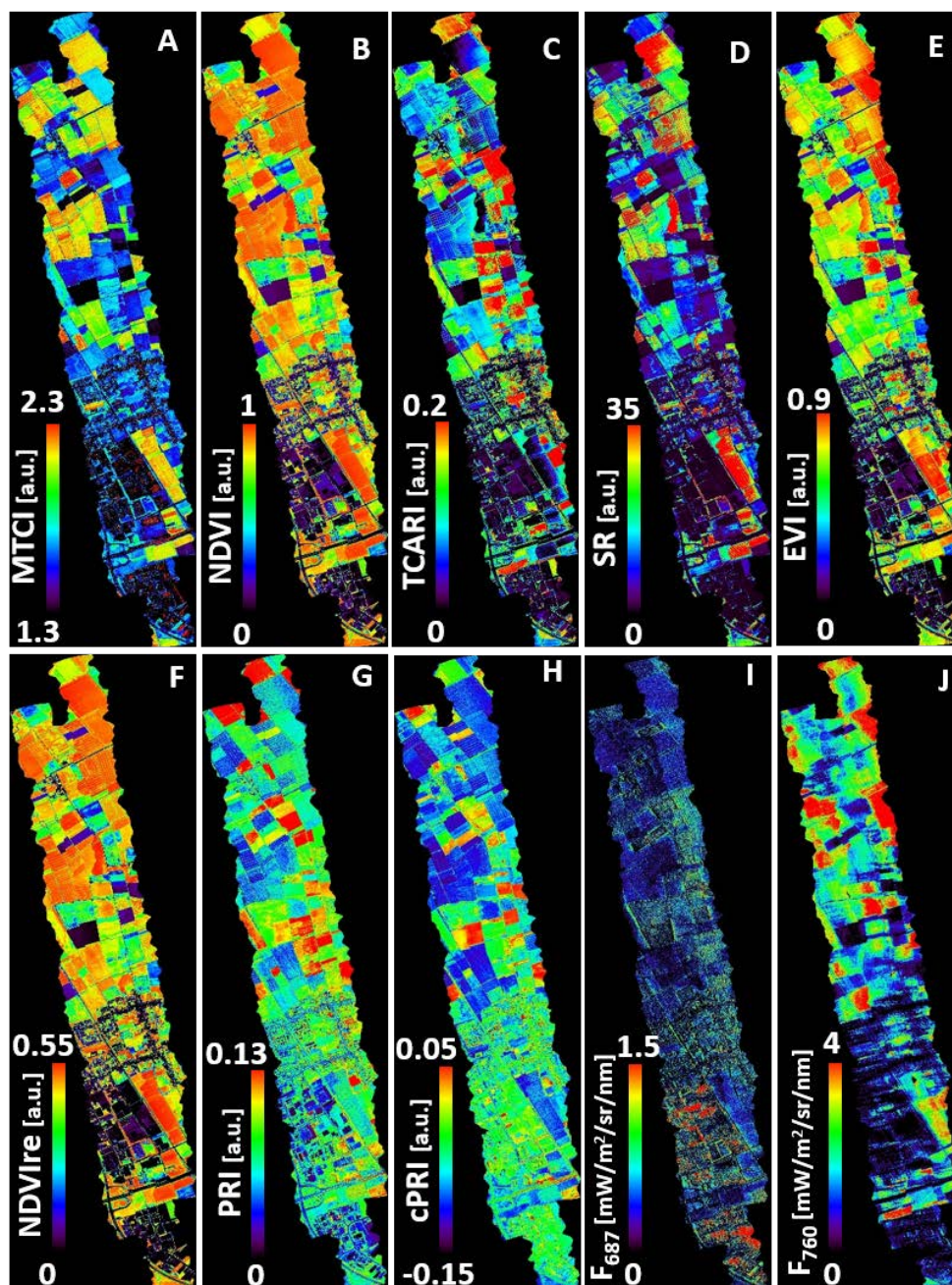
**Figure 36: Maps of the agricultural area around Selhausen showing different selected vegetation indices: MERIS terrestrial chlorophyll index (MTCI) (A); Normalized Difference Vegetation Index (NDVI) (B); Transformed Chlorophyll Absorption in Reflectance Index (TCARI) (C); Simple Ratio (SR) (D); Enhanced Vegetation Index (EVI) (E); Red-Edge Normalized Difference Vegetation Index (NDVIre) (F); Photochemical Reflectance Index (PRI) (G) and canopy Photochemical Reflectance Index (cPRI) (H); fluorescence at 687 ($F_{687}$) (I) and fluorescence at 760 ($F_{760}$) (J) calculated with the iFLD method. Data were recorded on 6 June 2014.**

## 6.1.2 Agricultural research campus Klein-Altendorf
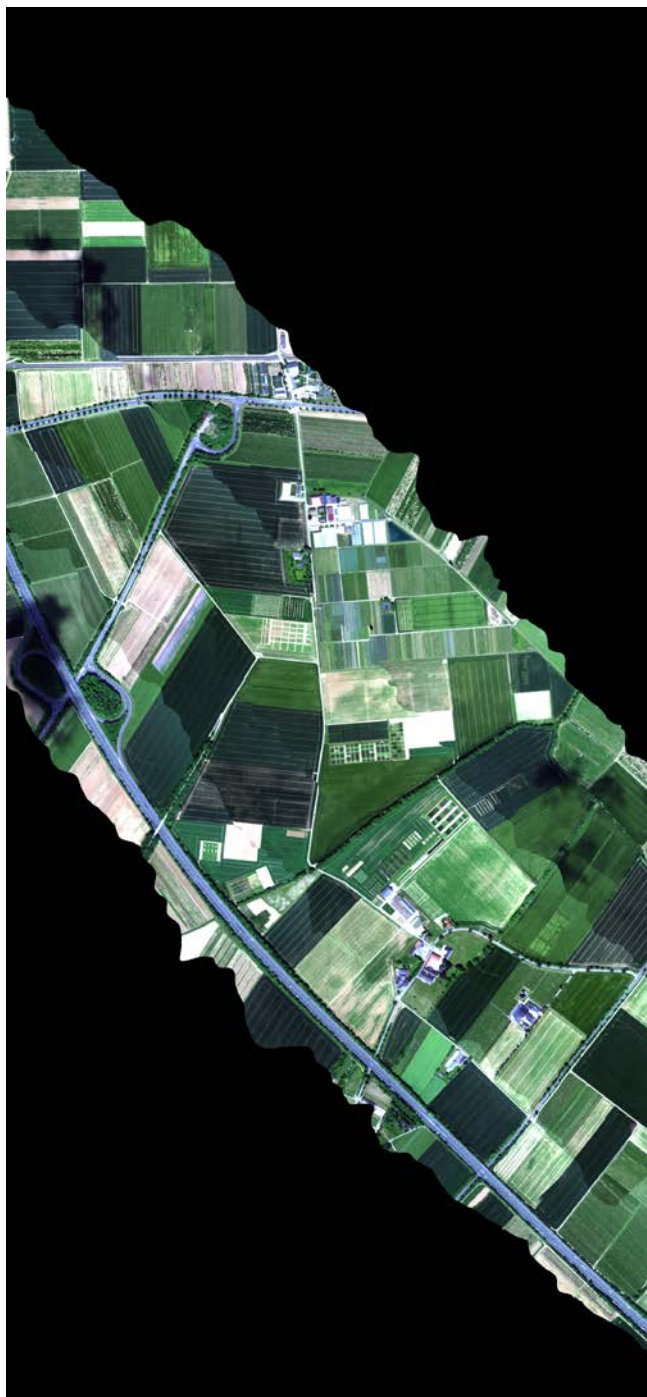


**Figure 37: True colour map (R: 156, G: 105, B: 51) of the research campus Klein-Altendorf recorded on 31 May 2014.**
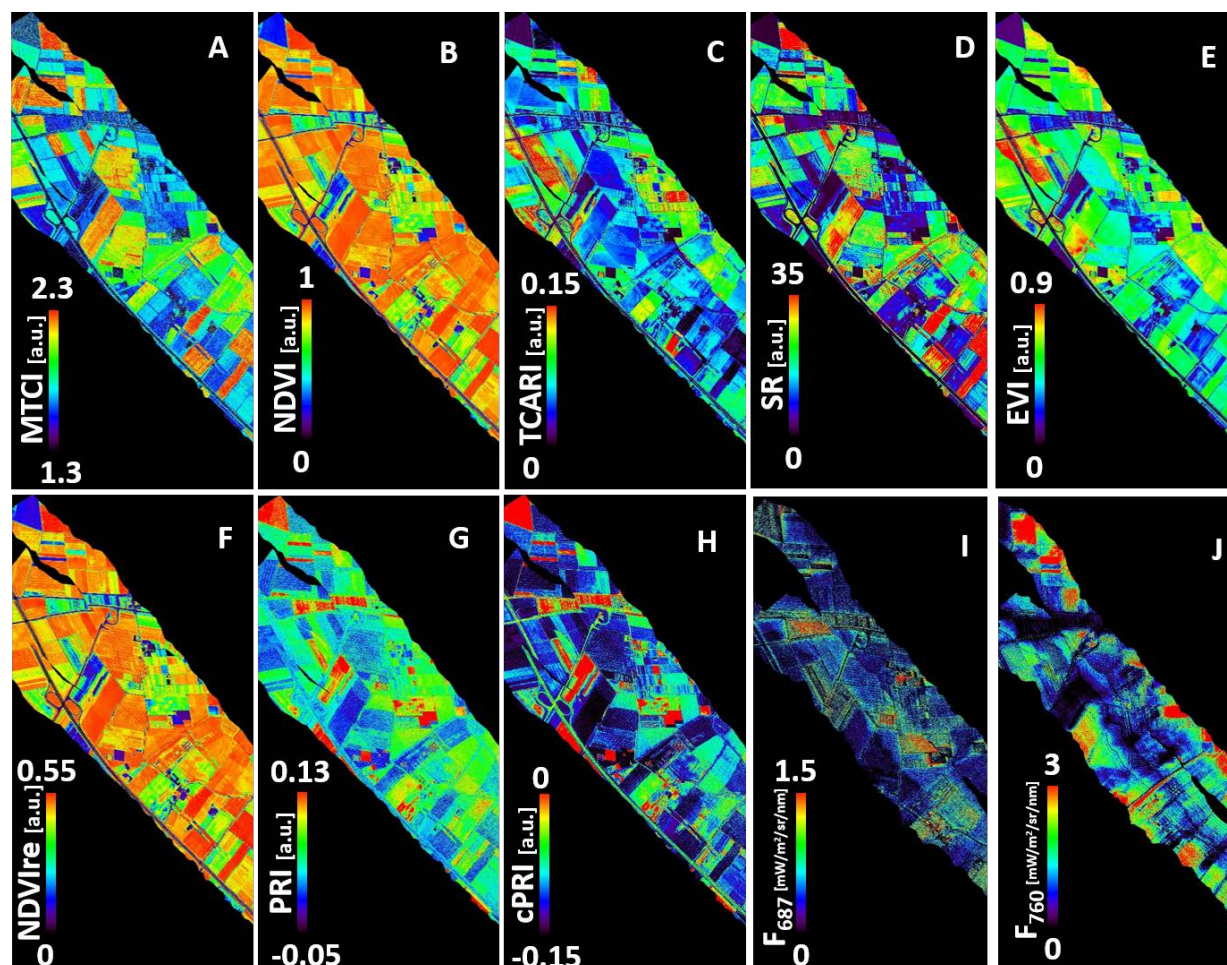
**Figure 38: Maps of the agricultural research campus Klein-Altendorf showing different selected vegetation indices: MERIS terrestrial chlorophyll index (MTCI) (A); Normalized Difference Vegetation Index (NDVI) (B); Transformed Chlorophyll Absorption in Reflectance Index (TCARI) (C); Simple Ratio (SR) (D); Enhanced Vegetation Index (EVI) (E); Red-Edge Normalized Difference Vegetation Index (NDVIre) (F); Photochemical Reflectance Index (PRI) (G) and canopy Photochemical Reflectance Index (cPRI) (H); fluorescence at 687 ($F_{687}$) (I) and fluorescence at 760 ($F_{760}$) (J) calculated with the i-FLD method. The most western flight line of the fluorescence maps needed to be removed due to wrong fluorescence values. Data were recorded on 31 May 2014.**

### 6.1.3  Vinyard with different soil properties



**Figure 39: True colour map (R: 156, G: 105, B: 51) of the vineyard farm recorded on 21 June 2014.**

**Figure 40: Maps of the vineyard farm showing different vegetation indices: MERIS terrestrial chlorophyll index (MTCI) (A); red-edge Normalized Difference Vegetation Index (NDVIre) (B); Transformed Chlorophyll Absorption Reflectance Index (TCARI) (C); Normalized Difference Vegetation Index (NDVI) (D); Simple Ratio (SR) (E); Enhanced Vegetation Index (EVI) (F); Photochemical Reflectance Index (PRI) (G); canopy Photochemical Reflectance Index (cPRI) (H); and Water Band Index (WBI) (I). Data were recorded on 21 June 2014.**

## 6.1.4 Agricultural research Farm Carlino (Mediterranean)



**Figure 41: True colour map (R: 156, G: 105, B: 51) of the agricultural research farm Carlino (Mediterranean) recorded on 11 June 2014.**
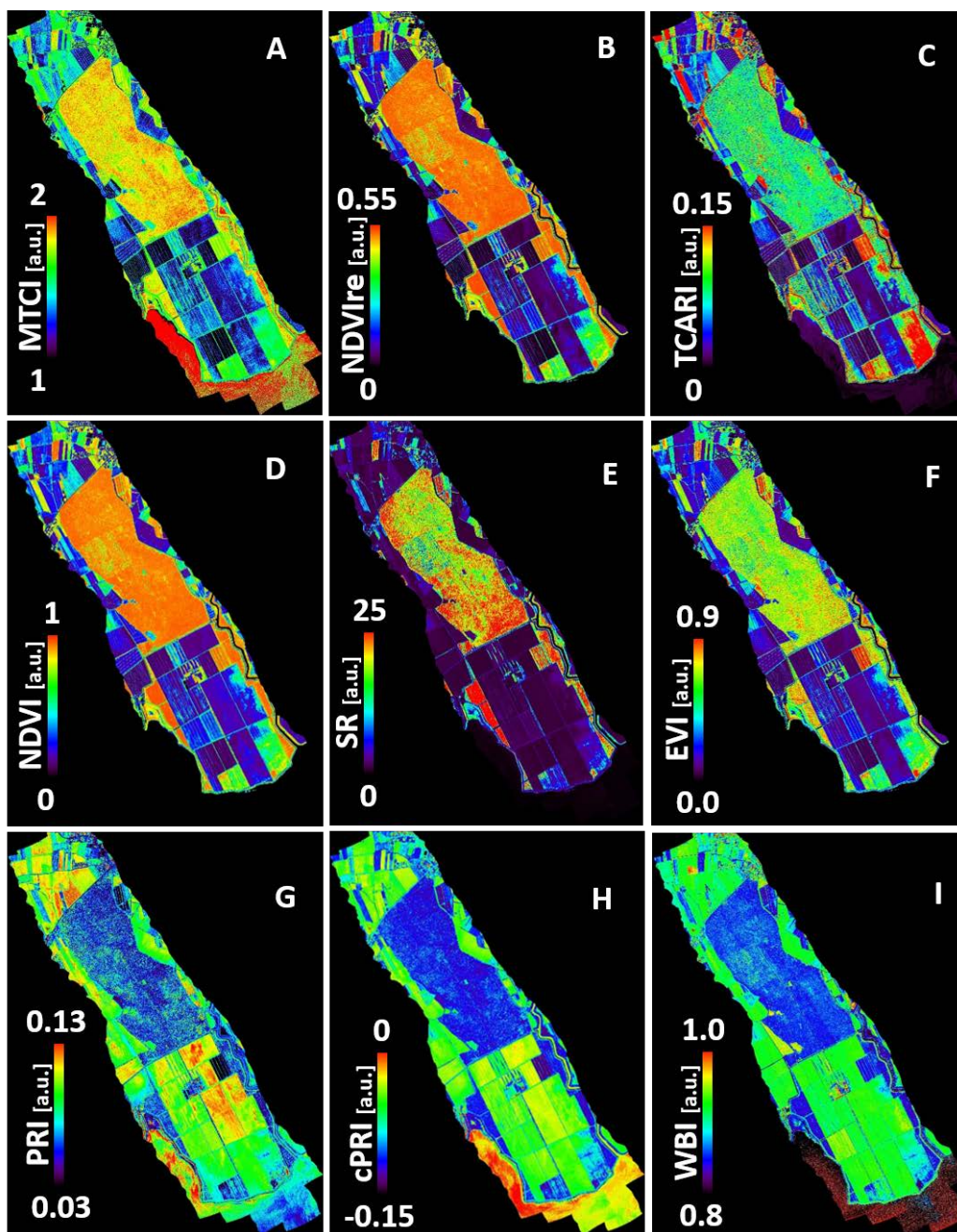
**Figure 42: Maps of the agricultural research farm Carlino (Mediterranean) showing different vegetation indices: MERIS terrestrial chlorophyll index (MTCI) (A); red-edge Normalized Difference Vegetation Index (NDVIre) (B); Transformed Chlorophyll Absorption Reflectance Index (TCARI) (C); Normalized Difference Vegetation Index (NDVI) (D); Simple Ratio (SR) (E); Enhanced Vegetation Index (EVI) (F); Photochemical Reflectance Index (PRI) (G); canopy Photochemical Reflectance Index (cPRI) (H); and Water Band Index (WBI) (I). Data were recorded on 11 June 2014.**

## 6.1.5 Latisana grassland



**Figure 43: True colour map (R: 156, G: 105, B: 51) of the Latisana grassland site recorded on 12 June 2014.**
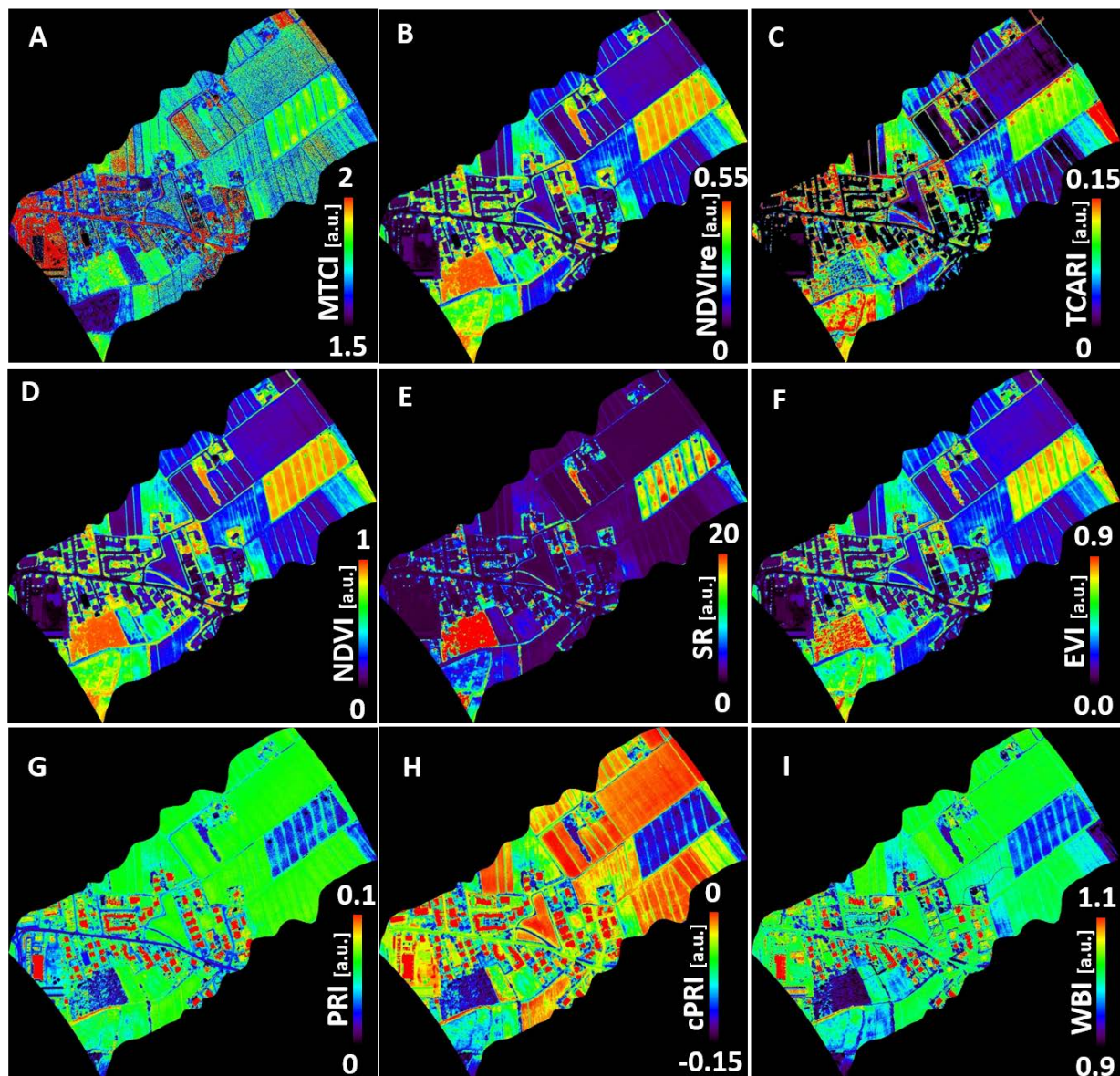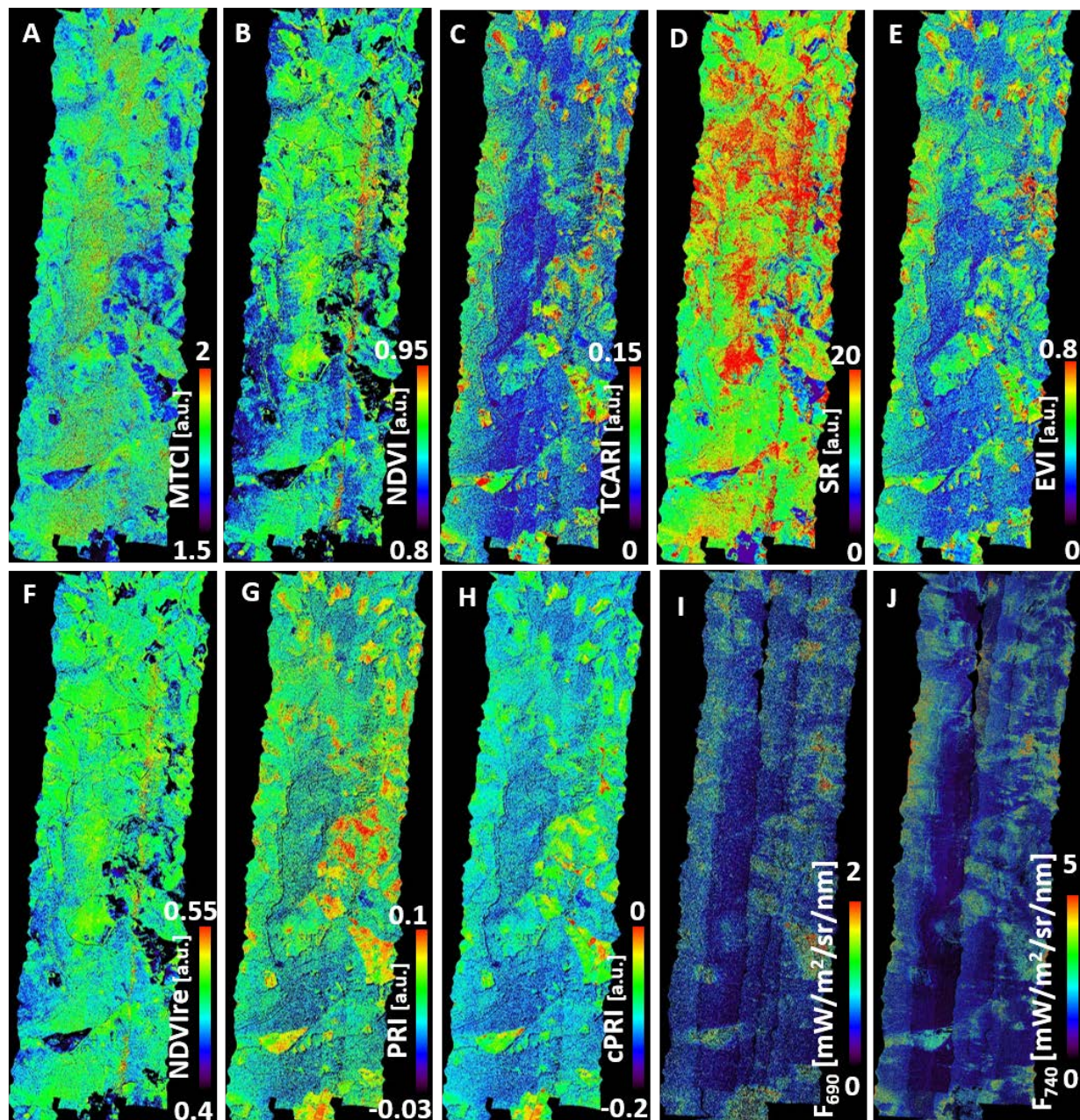
**Figure 44: Maps of Latisana grassland site showing different vegetation indices: MERIS terrestrial chlorophyll index (MTCI) (A); red-edge Normalized Difference Vegetation Index (NDVIre) (B); Transformed Chlorophyll Absorption Reflectance Index (TCARI) (C); Normalized Difference Vegetation Index (NDVI) (D); Simple Ratio (SR) (E); Enhanced Vegetation Index (EVI) (F); Photochemical Reflectance Index (PRI) (G); canopy Photochemical Reflectance Index (cPRI) (H); and Water Band Index (WBI) (I). Data were recorded on 12 June 2014.**

## 6.1.6 Spruce forest at Bílý Kříž



**Figure 45: True colour map (R: 156, G: 105, B: 51) of Bílý Kříž recorded on 19 July 2014.**

**Figure 46: Maps of Bílý Kříž showing different vegetation indices: MERIS terrestrial chlorophyll index (MTCI) (A); Normalized Difference Vegetation Index (NDVI) (B), Transformed Chlorophyll Absorption in Reflectance Index (TCARI) (C); Simple Ratio (SR) (D); Enhanced Vegetation Index (EVI) (E); Red-Edge Normalized Difference Vegetation Index (NDVIre) (F); Photochemical Reflectance Index (PRI) (G) and canopy Photochemical Reflectance Index (cPRI) (H); fluorescence at 690 ($F_{690}$) (I) and fluorescence at 740 ($F_{740}$) (J) calculated with the SVD method. Data were recorded on 19 July 2014.**

### 6.1.7 Beech forest at Štítná



**Figure 47: True colour map (R: 156, G: 105, B: 51) of Štítná beech forest recorded on 19 July 2014.**
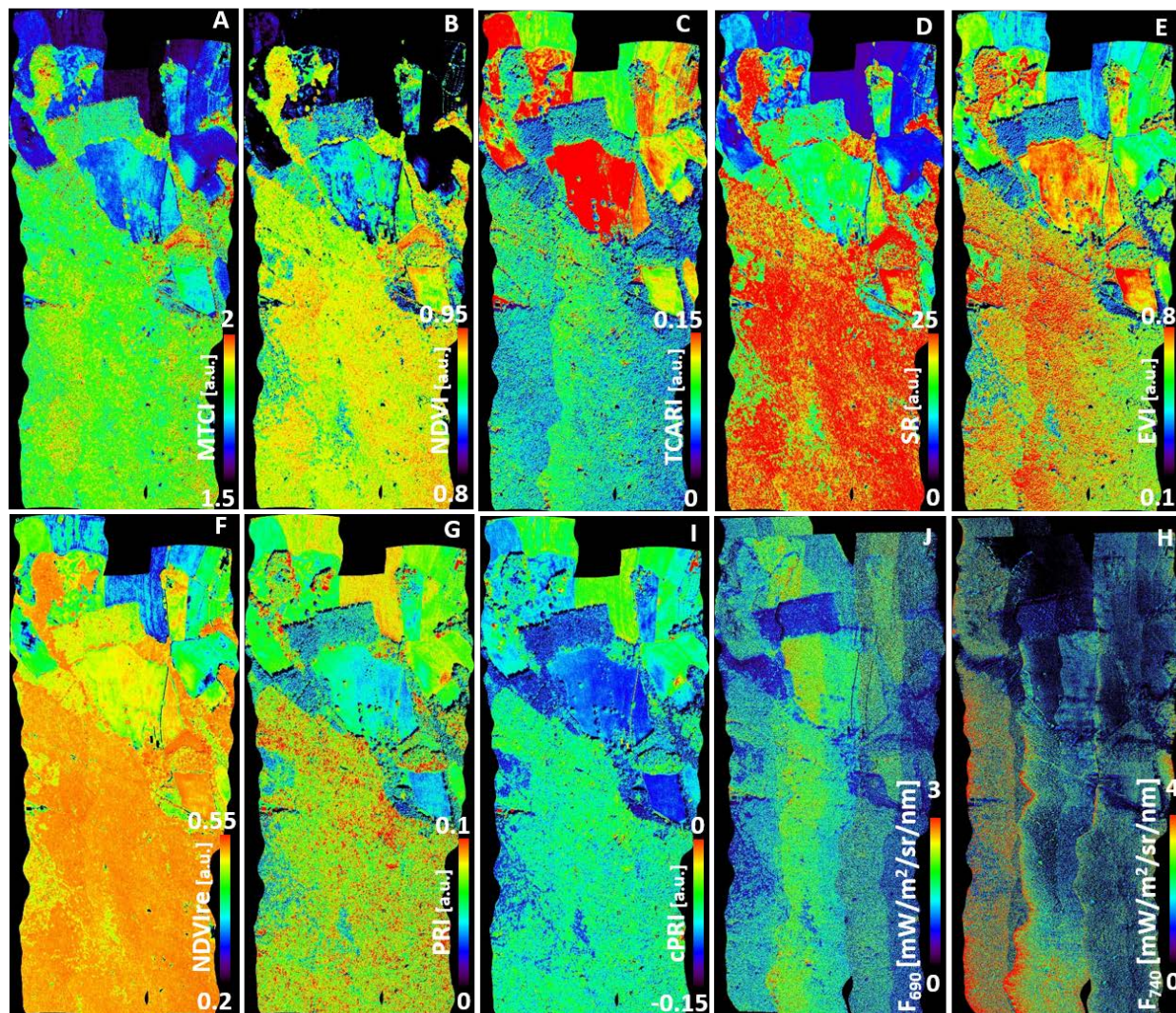
**Figure 48: Maps of Štítná beech forest showing different vegetation indices: MERIS terrestrial chlorophyll index (MTCI) (A); Normalized Difference Vegetation Index (NDVI) (B); Transformed Chlorophyll Absorption in Reflectance Index (TCARI) (C), Simple Ratio (SR) (D), Enhanced Vegetation Index (EVI) (E); Red-Edge Normalized Difference Vegetation Index (NDVIre) (F); Photochemical Reflectance Index (PRI) (G) and canopy Photochemical Reflectance Index (cPRI) (H); fluorescence at 690 ($F_{690}$) (I) and fluorescence at 740 ($F_{740}$) (J) calculated with the SVD method. Data were recorded on 19 July 2014.**

## 6.2 Relationship between fluorescence signal and soil fraction within the *HyPlant* pixel

The main goal of the mixed-pixel experiment was to investigate the role of fractional cover (Fc) on the fluorescence signal by combining field data, *HyPlant* images, and modelling tools. Therefore, an experimental setup needed to be designed, in which only the fractional cover and the leaf area were expected to change, while other variables such as LAI, Cab, Cw, incoming PAR, fAPAR were constant. On of 19 June 2014, grassland plots with 5 different fractional covers were set up. Each plot had a dimension of 4 x 1 m, and five replicates for each plot were created (Figure 49) on a homogenous 'rolling turf' grassland at lat 45.796108°; long 13.034918°.
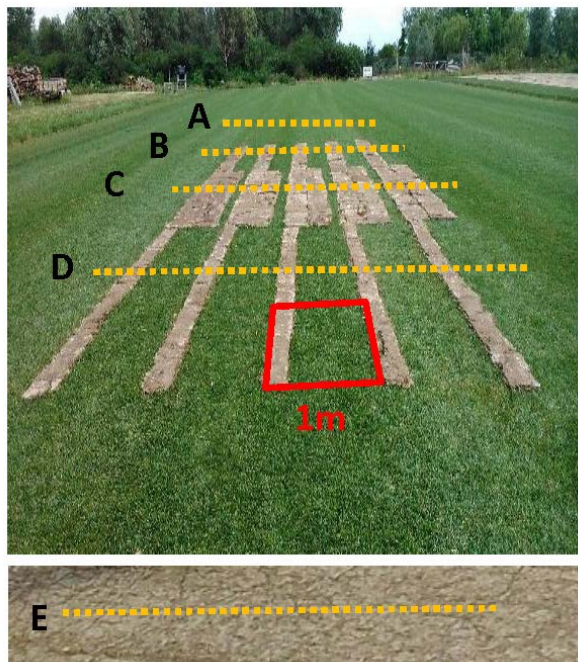


- A: full cover; Fc = 100%;
- B: medium cover; Fc = 60%;
- C: low cover; Fc = 20%;
- D: high cover; Fc = 80%;
- E: bare soil; Fc = 0.

**Figure 49: Sketch of the mixed pixel experiment.**

Five flight lines of the mixed-pixel experiment were recorded on 19 June 2014. The flight line at 11:50 a.m. local solar time (20140619-MIX-1150-0600-L3-S-FLUO) was the most suitable flight line because it was flown on the solar principle plane and showed the smallest cloud coverage (cirrus clouds). The flight altitude of 600 m resulted in the spatial pixel size of 1 x 1 m.
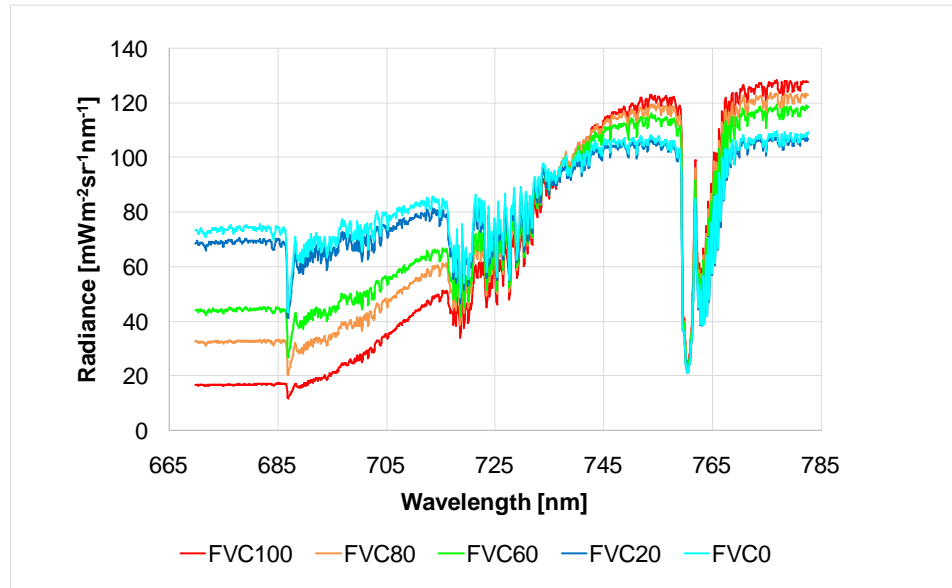
**Figure 50: At-Sensor radiance spectra of the fluorescence FLUO sensor module for the different factional cover classes.**

*HyPlant* at-sensor radiances (Figure 50) were used to estimate $F_{760}$. From those field experiment data, we found a strong linear relationship between fluorescence and vegetation fractional cover (Figure 51).
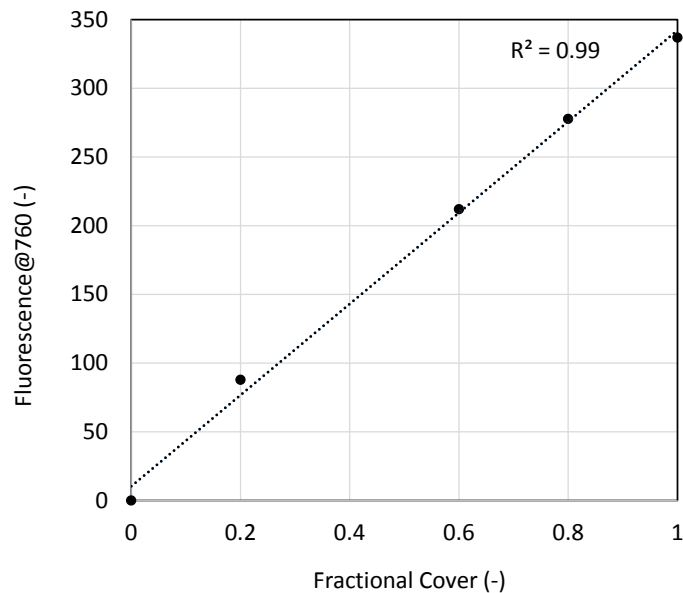


**Figure 51: Relationships between fluorescence at 760 nm and vegetation fractional cover**

The measured fluorescence values were then compared with the fluorescence values modelled using a linear mixing approach.

$$Fs = Fs_{veg} \times f_c + Fs_{soil} \times (1 - f_c)$$

Fs represents the modelled value of the fluorescence, $Fs_{veg}$ and $Fs_{soil}$ are the pure vegetation and bare soil components, respectively (derived from *HyPlant*), and $f_c$ is the fractional cover.

Figure 52 shows the comparison between the observed fluorescence and the modelled fluorescence, and it indicates that the unmixing model is well suited to model fluorescence in heterogeneous pixels.
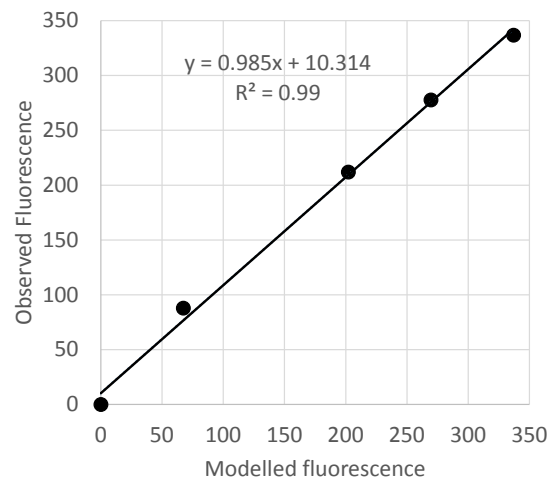


**Figure 52: Comparison between fluorescence retrieved from *HyPlant* and modelled fluorescence using the linear unmixing approach.**

In summary, this experiment allowed us to explore the relationships between fluorescence and fractional cover, indicating that the fluorescence of the pixel at $O_2$-A scale linearly with vegetation fractional cover. Moreover, we demonstrated that a simple unmixing model, with two classes, is suitable to model fluorescence in mixed pixel and this found may have implications for large scale mapping in the context of the FLEX mission.

## 6.3 Dynamic relations between reflectance, fluorescence, PRI, and photosynthetic gas exchange – the specific physiological effects the different treatments

To better understand the relationship between fluorescence emission on the one hand and photosynthetic energy dissipation, vegetation stress and canopy gas-exchange on the other hand, four different experimental biochemical treatments were used.

(1) The application of **Kaolin**, a highly reflective white powder, increases the leaf-surface reflectance (Figure 53) and therefore reduces the absorption of photosynthetic active radiation (APAR). Absorption coefficients of Kaolin are uniform in the PAR region (Lindberg & Smith 1974) and the effective irradiance on both photosystems should be reduced equally. As a result, effective light energy at both photosystems should be reduced in the course of the experiment. Additionally, high light stress that may occur during midday conditions should be prevented.

*Hypothesis 1: fluorescence of both peaks should be reduced as a result of the reduced effective PAR. Additionally, PRI should be reduced, indicating the lower high-light stress.*

(2) Secondly, an anti-transpirant was applied. We used Vapor Gard, which is a commercial product that is spayed on the plants and produces a thin, transparent wax layer on the leaf surfaces. The layer does not penetrate into the leaves and reduced stomatal conductance by physically sealing the leaf stomata. As a result also $CO_2$ uptake in the leaves is reduced and leaf internal $CO_2$ concentrations are reduced. Similar effects happen during acute drought, when limited water availability cause stomata to close. Such limitation in leaf internal $CO_2$ concentration should result in an increase of the fluorescence emission because of the substrate limitation of photosynthesis (Figure 53).

*Hypothesis 2: stomatal closure will decrease fluorescence emission. Greater decrease is expected in the red fluorescence emission.*
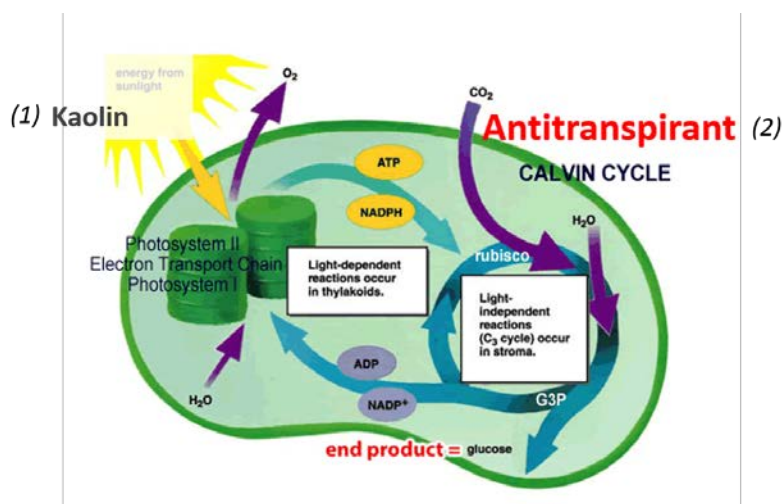
**Figure 53: Effect of physical stressors at different levels of photosynthesis: (1) reduction of APAR by increased leaf surface reflectance (Kaolin treatment); (2) block of gas exchange (Vapor Gard/anti-transpirant treatment).**

(3) Thirdly, we applied a biochemical agent that interfered with electron transport capacity in the chloroplast (Figure 54). **Paraquat** is a well-studied agent in photosynthesis research that blocks the electron transfer at photosystem I. In detail, the electrons are transferred from Ferredoxin to Paraquat, producing a hyperoxid via a Paraquat radical. This reaction results in a rapid and fundamental destruction of the photosynthetic apparatus via the accumulation of hyperoxid molecules (Trebst 2007). In a short time frame after application, a reduction of electron transport at photosystem I may affect primarily fluorescence from photosystem I and thus have an intermediate and strong effect of the far-red fluorescence (Figure 54).

*Hypothesis 3: Paraquat causes an immediate and strong increase of the far-red fluorescence after the application and, in a longer time frame (hours to days), undefined changes in red and far-red fluorescence and the PRI because of the destruction of the photosynthetic machinery.*

(4) Finally, we applied **Dicuran**, which is the commercial name of a **Chlortoluron** formulation 3-(3-Chloro-4-methyl)-1,1-dimethylurea. It is different from Diuron (DCMU) which is in fact 3-(3,4-Dichlorophenyl)-1,1-dimethylurea. It is a well-characterized herbicide that blocks the electron transport at photosystem II. Dicuran still used as herbicide in many countries and applied in photosynthesis research to block electron transfer transiently from Plastochinone A ($Q_A$) to Plastochinone B ($Q_B$) (Figure 54). It thus increases photosystem II fluorescence greatly and is often used in laboratory studies to induce a maximum PS II fluorescence (Trebst 2007). Dicuran is broken down within the course of a few days, and the photosynthetic electron transport is recovered. Therefore, we expect a great increase of both fluorescence peaks immediately after application and a decrease of initial values in the course of a few days. In our experiment, we applied Dicuran in various doses with the aim to investigate the dose response characteristics of the experimental block of photosynthetic electron transport at Photosystem II (PS II) and the intensity of fluorescence emission.

*Hypothesis 4: Dicuran causes an immediate and strong increases of the red and far-red fluorescence emission. The effect should be reversible, and initial fluorescence values should be obtained after a few days.*
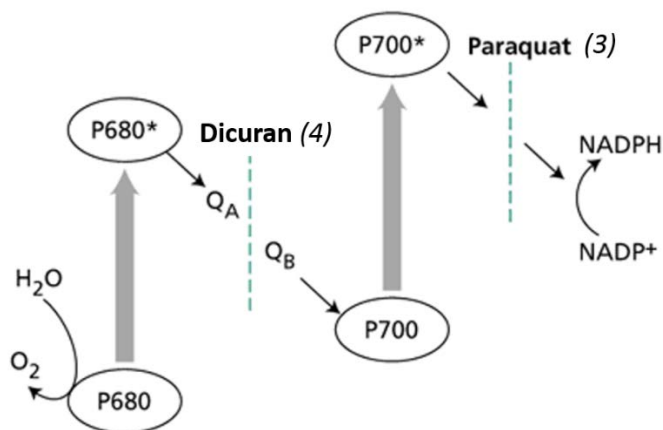


**Figure 54: Effect of chemical stressors on different levels of the photosynthetic apparatus. Block of electron transport at photosystem I (P700; Paraquat treatment); block of photosynthesis at Photosystem II (P680; Dicuran treatment).**

## 6.3.1 Experimental design

A grassland site was chosen for the experiment. The 'rolling turf' is optimally managed in terms of soil homogeneity and water supply and showed the most appropriate plan density. In total, 12 homogeneous grassland plots were used for the experiment. Each plot of the Kaolin experiment had a dimension of 9 x 9 m. The three additional treatments had plots dimension of 12 x 9 m. Before treatment, the plots were compared using TOC spectroscopy (chapter 4.2.2) to verify their homogeneity before the application. The average and standard deviation of the normalized difference vegetation index (NDVI) and of the MERIS terrestrial chlorophyll index (MTCI) of each plot before the treatment is shown in Figure 55.

The NDVI of all plots showed only minor differences between the plots and values were between 0.88 and 0.9. The MTCI however showed subtle differences between the different plots. It must be noted, that the MTCI is sensitive to already slight changes in the red-edge region and absolute values change strongly with the bands in the red-edge used for the calculation. Nevertheless, the variation of the MTCI

between the plots indicate slight different in terms of their pigment content or leaf area index. Plots 2, 8, and 11 which are distributed over the whole grassland field were chosen as control plots, to also take the variability of the MTCI into account.
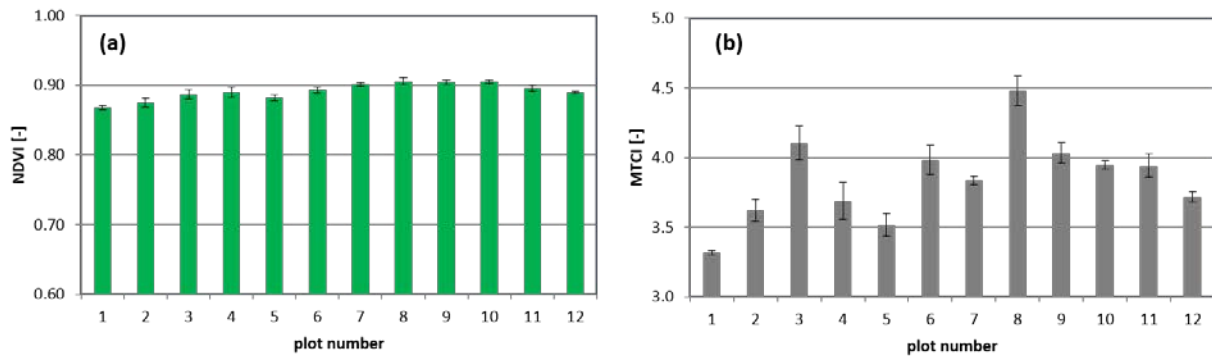


**Figure 55: Average and standard deviation of the midday measurements of (a) normalized difference vegetation index (NDVI) and of the (b) MERIS terrestrial chlorophyll index (MTCI) of each plot before the treatments started. Data were recorded on 9 July 2014.**

For an optimal statistical use of the available plots, we defined an experimental plan during which we applied the agents at different days of the campaign. This allowed a cross-validation of the results and enabled us to have different times after the treatment in one *HyPlant* overpass. Date and treatment can be found in Figure 57 and Table 23. The plots were continuously measured using ground and airborne sensors, which were applied in a complex rotation scheme to make best use of the existing resources (Figure 58). The overall goal was to capture the effects of the treatment on fluorescence emission and variations in PRI on the relevant time scales (Figure 58). To understand the dynamics of the functional response of the vegetation in relation to the changes in fluorescence emission and PRI, we normalized all measurements to the time of treatment. The time of treatment was set to zero, and all measurements are expressed as days before and after the treatment. By this, we archive that all data are inter-comparable and that characteristic temporal dynamics can be extracted.

The environmental conditions were almost stable over the measurement period. The incoming global radiation measurements from 10 June to 13 June 2014 of the Latisana field site indicate stable radiation conditions (Figure 56). However, the cloud influence increased on the following measurements days. Air temperature decreased slightly from 35 °C of the first three days of the measurements to only 23 °C on 16 June 2014. For the remaining time of the experiment, maximum temperature values fluctuated around 25 °C (Figure 56).
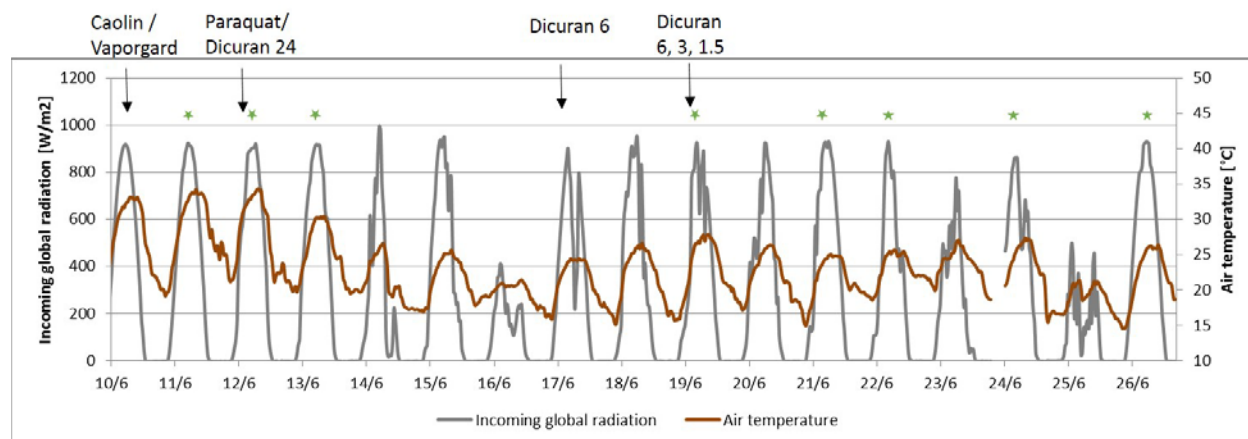
**Figure 56: Incoming global radiation [W m⁻²] and air temperature [°C] recorded from the meteorological station on the Latisana grassland field for the time period of the treatment experiments (10 June to 26 June 2014). Green stars indicate available *HyPlant* overpasses, black arrows the time of the different treatment applications.**
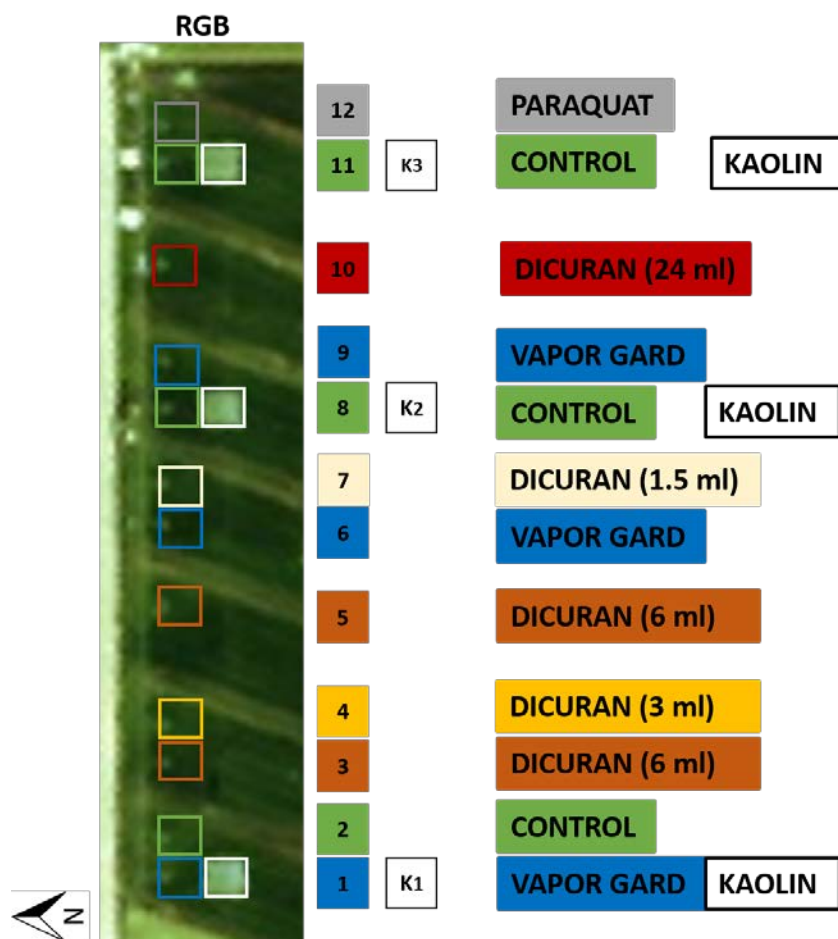


**Figure 57: Experimental setup of the treatment experiment.**

**Table 23: Dates and amounts of the treatment experiment.**

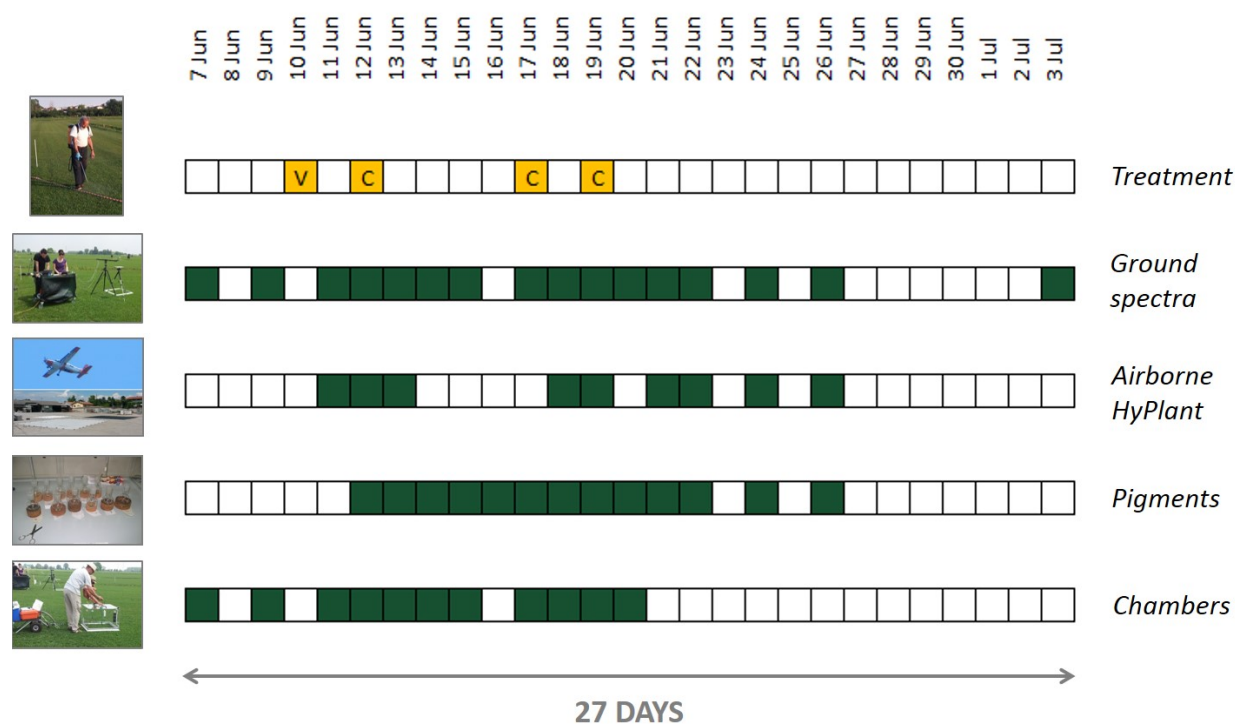| Date | Plot | Treatment | Amount [ml/l] |
|---|---|---|---|
| all dates | 2, 8, 11 | Control | |
| 10 June | K1-3 | Kaolin | |
| 10 June | 1, 6, 9 | Vapor Gard | |
| 12 June | 12 | Paraquat | |
| 12 June | 10 | Dicuran | 24 |
| 17 June | 3 | Dicuran | 6 |
| 19 June | 5 | Dicuran | 6 |
| 19 June | 4 | Dicuran | 3 |
| 19 June | 7 | Dicuran | 1.5 |



**Figure 58: Timeline and overview of the acquired data of the treatment experiment in Latisana 2014.**

A core dataset of flight lines (± 1 hour of solar noon) was selected to cover the changes of the different treatments (Table 24). In comparison with available incoming radiation, flight lines with the lowest cloud influence was chosen. Associated ground measurements, such as top-of-canopy reflectance and fluorescence emission as well as canopy gas-exchange measurements, are available for the time series.

**Table 24: Core dataset of Latisana flight lines.**

| Date | DOY | Recording time (local time) of the flight line |
|---|---|---|
| 11 June | 162 | 14:52 |
| 12 June | 163 | 13:40 |
| 13 June | 164 | 13:52 |
| 19 June | 170 | 13:34 |
| 21 June | 172 | 12:57 |
| 22 June | 173 | 12:10 |
| 24 June | 175 | 11:56 |
| 26 June | 177 | 13:18 |

All together, eight *HyPlant* scenes were analysed in detail (Table 24). To exemplify the data processing and to visualize the results, three flight lines were selected, and spatial maps of the different biophysical parameters (Figure 59 (A, NDVI); (B, PRI)) and the fluorescence emission at 687 nm and 760 nm are presented (Figure 59 (C, $F_{687}$); (D, $F_{760}$)). Similar analyses were done for all eight core flight lines. From these flights lines, regions of interest (ROIs) that cover 26 pixels in the middle of the treatment plots were manually selected. The position of the treated plot and the selected ROIs are indicated by the rectangles in Figure 59). In the following, the spatial means of the ROIs are shown to show the temporal development of the fluorescence parameters after the specific treatment.

Kaolin and Vapor Gard plot were already treated on 10 June 2014. As no *HyPlant* flight line is available on this day, the treated plots are compared to the control plots on 11 June 2014.
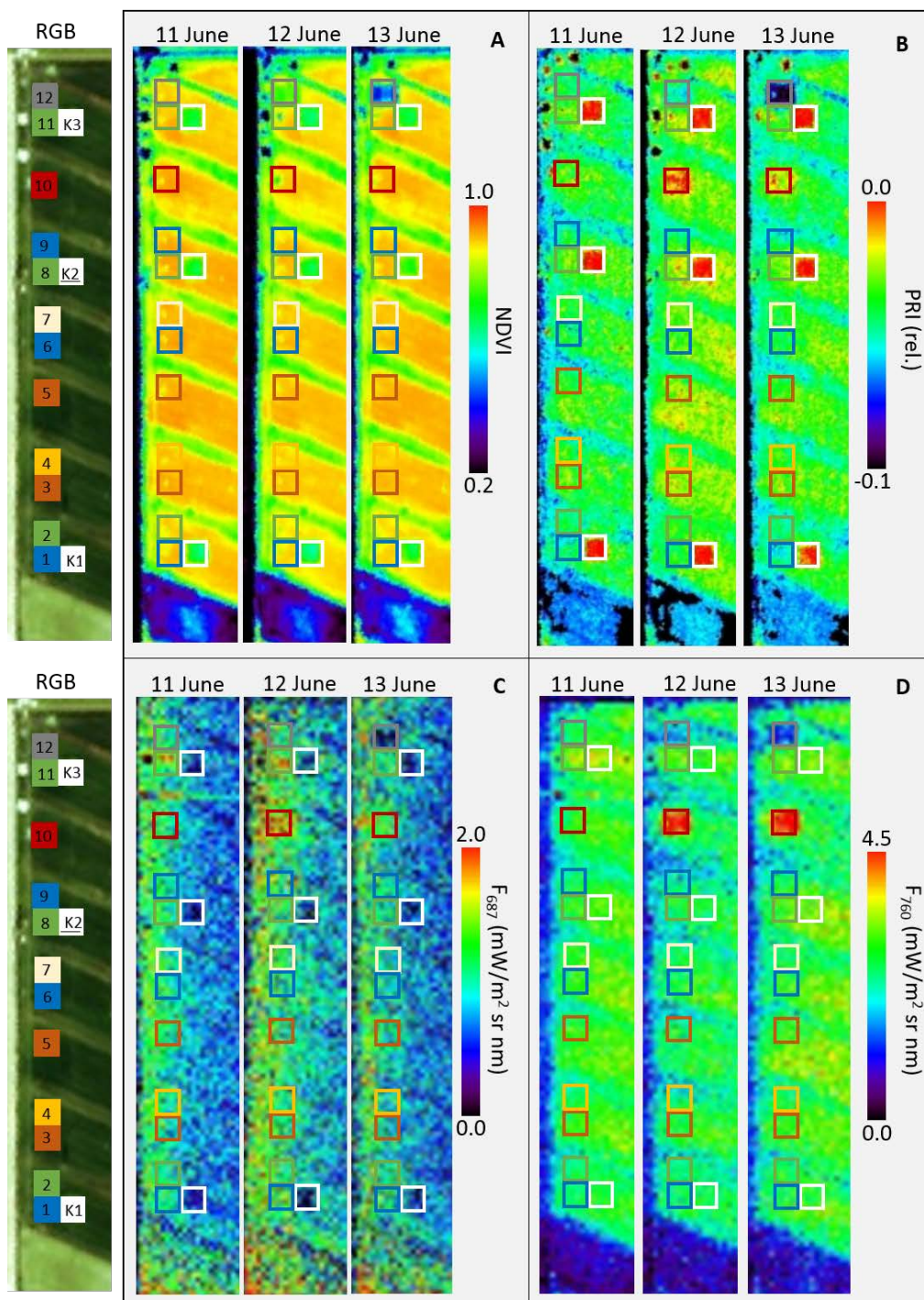
**Figure 59: RGB images, two selected vegetation indices (A: NDVI, B: PRI), and maps of the two fluorescence peaks (C: sun-induced fluorescence at 687 nm ($F_{687}$); D: sun-induced fluorescence at 760 nm ($F_{760}$)) of an example flight line in Latisana. The maps include the plot design of the different treatments.**

### 6.3.2  Effect of Kaolin treatment

The overall effects of the application of the Kaolin powder is illustrated through additional data collected during the months of July in the same fields of Latisana. During this post-campaign study, the effects of Kaolin application were investigated using an array of sensors and two eddy covariance systems on a sufficiently large surface patch. For those additional measurements, the Kaolin powder was applied to an area of 1 ha.

**Effects on reflectance and vegetation indices**

Overall, the Kaolin greatly changed the reflectance of the leaves, leading to higher albedo. The albedo, defined as the fraction of visible + near-infrared light reflected by the grass, was significantly increased by the treatment (Figure 60). This is illustrated using a BACI (Before After Control Impact) analysis by comparing reflectance and gas exchange properties during two consecutive clear-sky days (Figure 61) before and after the treatment.
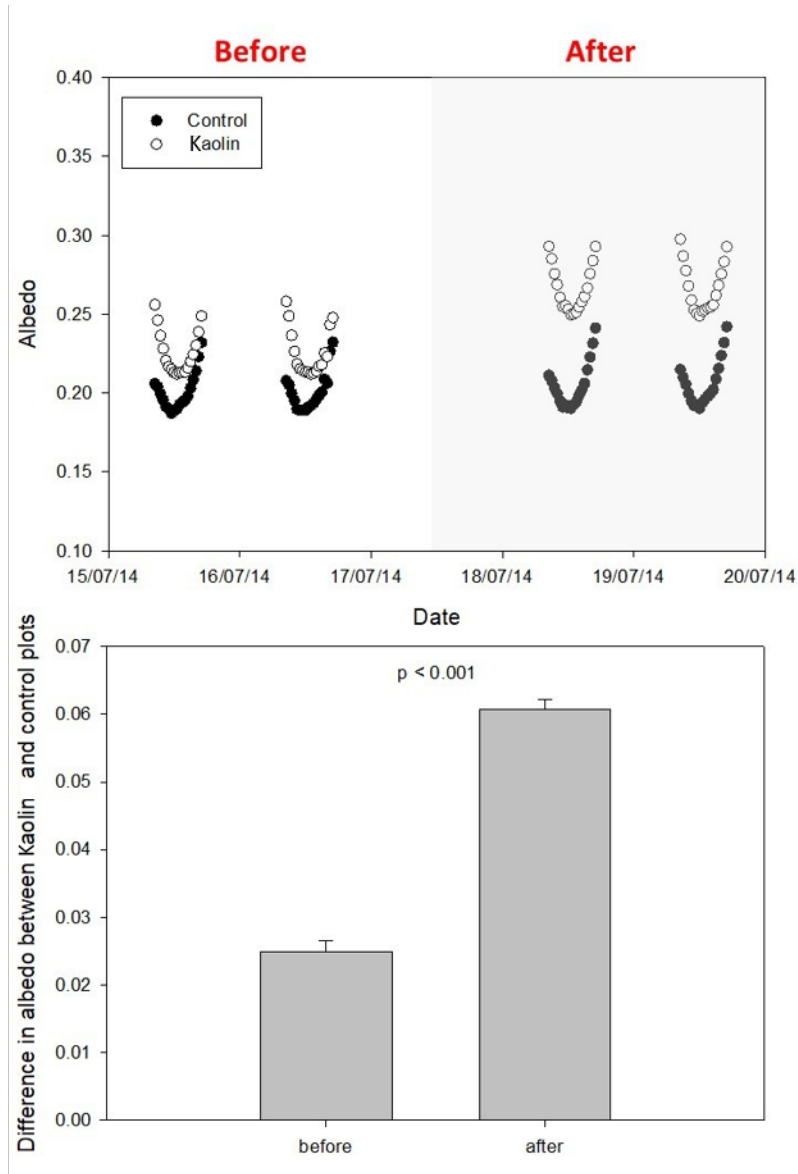
**Figure 60: Albedo measurements during two consecutive clear-sky days (upper panel) and difference in the average albedo (lower panel) before and after Kaolin application (control: solid symbols; Kaolin: open symbols). Vertical bars indicate standard error (n = 36). The Kaolin treatment increased albedo by 29% on average.**
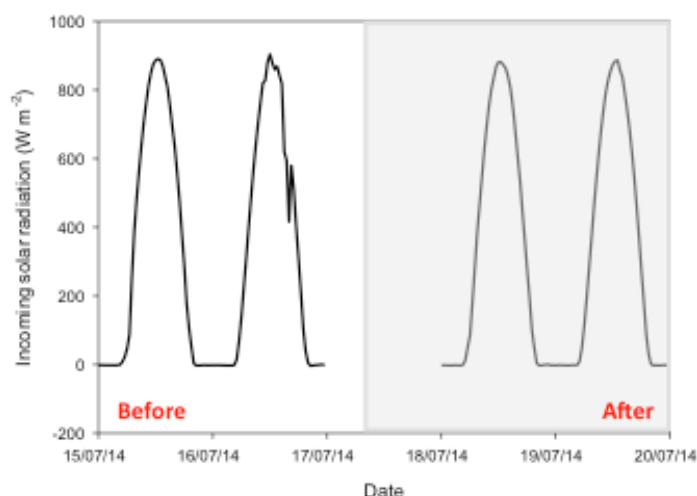
**Figure 61: Shortwave incoming PAR during two clear-sky days before and after the Kaolin treatment in Latisana.**

The increase of the albedo, caused by the Kaolin treatment, is also clearly visible in a higher reflectivity, especially in the VIS/NIR range of the Kaolin-treated plots K1-3. Exemplary reflectance spectra from *HyPlant* DUAL acquisition are shown in Figure 62. From the *HyPlant* reflectance spectra, the effective photosynthetic active radiation (PAR) was calculated using the wavelength between 400 to 700 nm. A reduction of 28% of the effective PAR could be calculated comparing the control and Kaolin-treated plots from the *HyPlant* flight line on 11 June 2014.
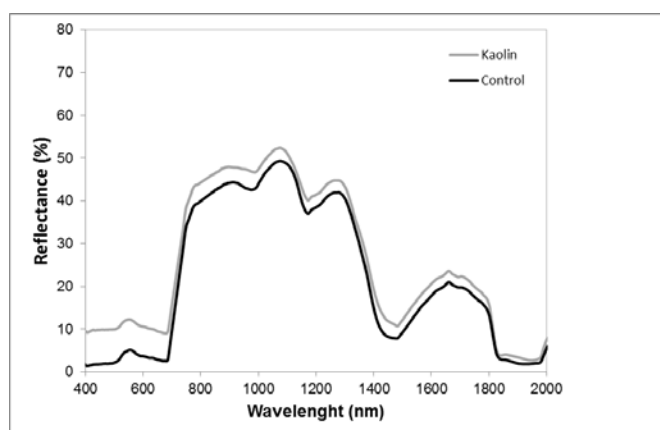


**Figure 62: Mean reflectance spectra measured from *HyPlant* acquisition comparing Kaolin-treated plots with control plots on 11 June 2014.**

The clear and significant effect on absorbance, reflectance, and albedo that is also visible in greenness-related vegetation indices such as the NDVI, which showed a reduction of (-24% to -20%) as measured by *HyPlant* on Kaolin-treated plots on 11, 12, and 13 June (Figure 63 and Table 26).
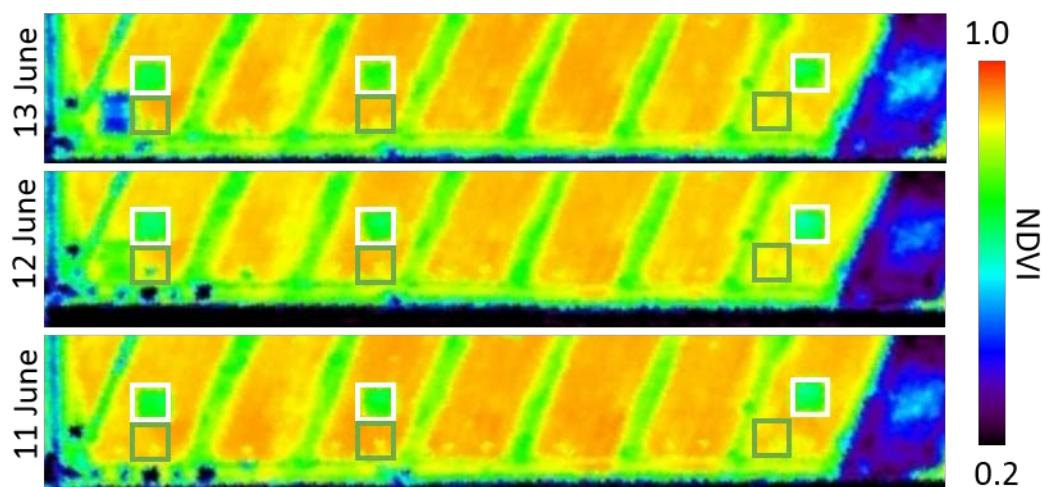


**Figure 63: *HyPlant*-measured NDVI. The Kaolin-treated plots are denoted by a white frame, control plots by a green frame.**

Changes were also observed in the Photochemical Reflectance Index (PRI) (Figure 59, B); however, these changes cannot be interpreted to reflect changes in non-photochemical energy dissipation (NPQ). The link between PRI and NPQ is only valid for conditions where the reference waveband at 570 nm remains unaffected. Kaolin clearly changed reflectance at 570 nm (Figure 62); thus, the interpretation of PRI as a physiology-related parameter is not valid, and no further results on the PRI are presented from the Kaolin treatment.

**Effect on sun-induced fluorescence**

In addition, significant lower $F_{687}$ values of Kaolin-treated plots could be detected from *HyPlant* recordings Figure 64. For the three days after, the $F_{687}$ of the Kaolin-treated plots was 60% less than the red fluorescence of the control plots (Figure 64, Table 26). The far-red fluorescence ($F_{760}$), however, did not show any significant differences between Kaolin-treated and control plots (Figure 59, D). We investigated the results of different retrieval methods (3-FLD, iFLD with and without brightness correction) on the Kaolin-treated plots. The $F_{760}$ emission showed a strong dependency on the high reflectivity of the Kaolin powder, resulting in a high uncertainty of the signal. Therefore, the $F_{760}$, will not be used for any further interpretation of the Kaolin treatment.
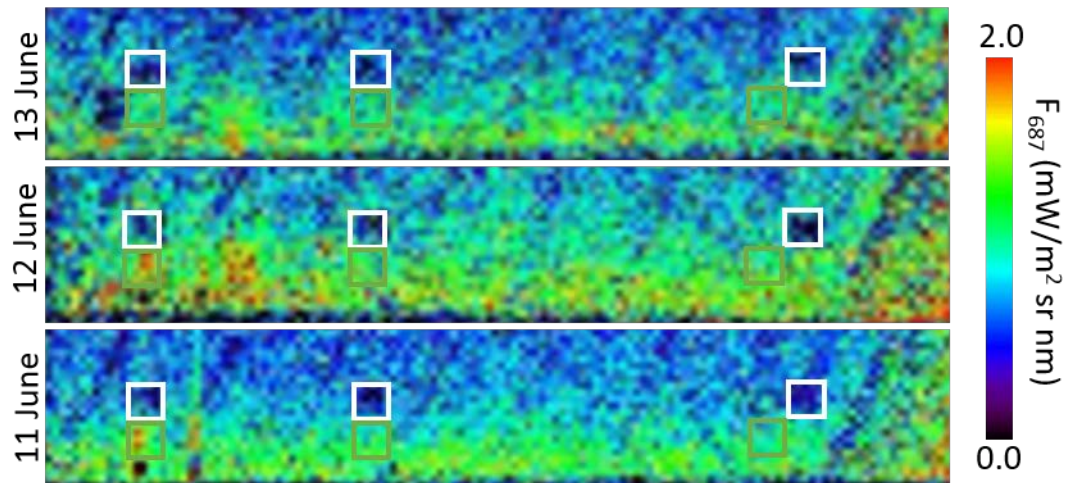
**Figure 64: Sun-induced fluorescence at 687 nm ($F_{687}$) from *HyPlant* recording. The Kaolin-treated plots are denoted by a white frame, control plots by a green frame.**

**Effect on canopy energy and gas exchange**

Changes in albedo caused by the Kaolin application led to a substantial decrease in the net radiation that was associate with a decrease in both latent and sensible heat flux (Figure 65).

The overall amelioration of plant water status of Kaolin-treated plants likely compensated the reduction on light absorption associated to enhanced albedo, and accordingly, the Net Ecosystem Exchange (NEE) of the large plots before and after the treatments were not statistically significantly different (Figure 65).
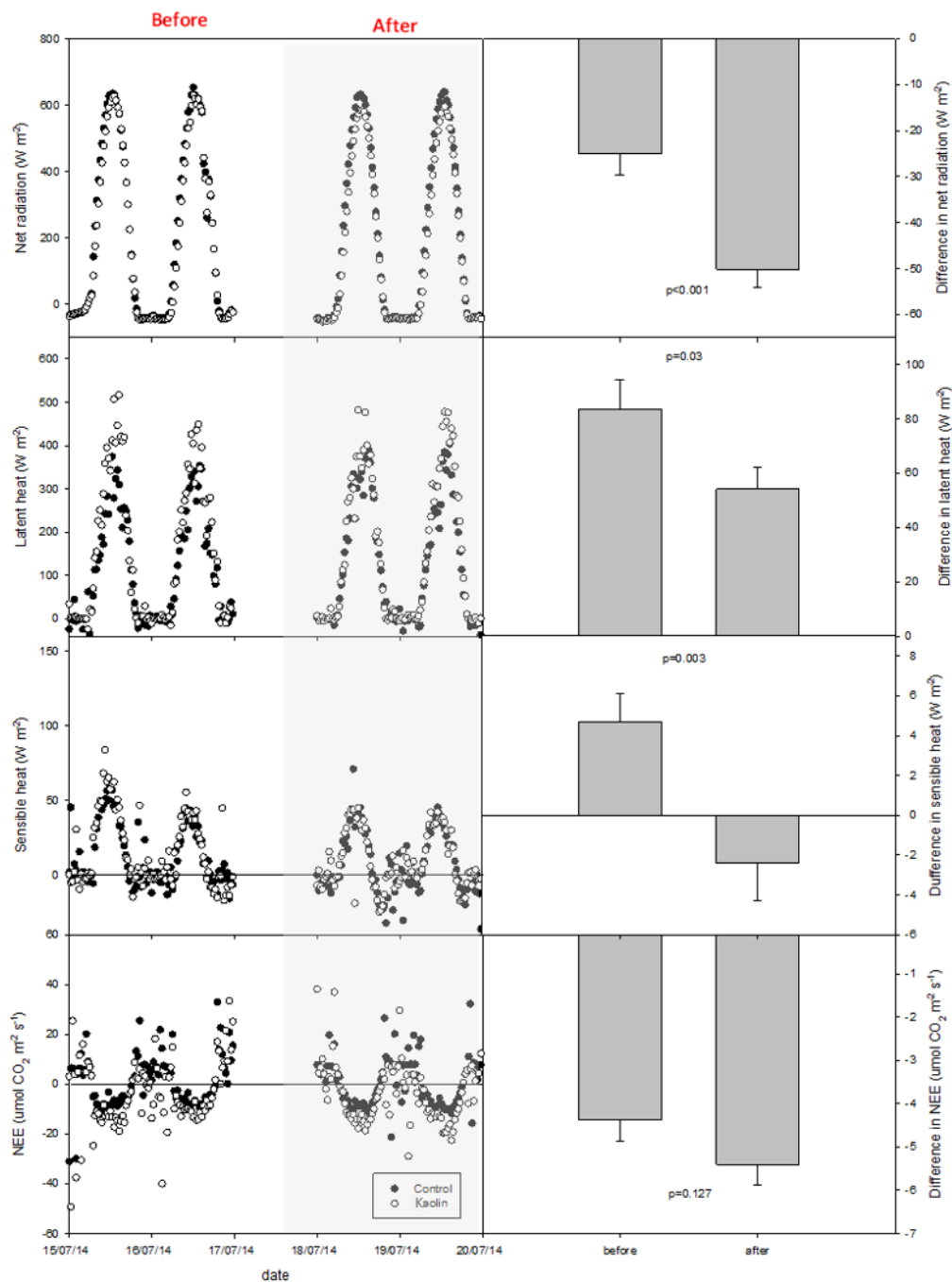
**Figure 65: The effect of Kaolin application on the large plots in July on net radiation, sensible and latent heat fluxes and net ecosystem exchange (NEE) measured by eddy covariance. The panels on the left report the half-hour data before and after Kaolin application (control: solid symbols; Kaolin: open symbols). The grey bars on the right panels report the relative difference between the two plots (Kaolin and control) before and after treatment application. Vertical bars indicate standard error (n = 38).**

### 6.3.3 Effect of anti-transpirant Vapor Gard

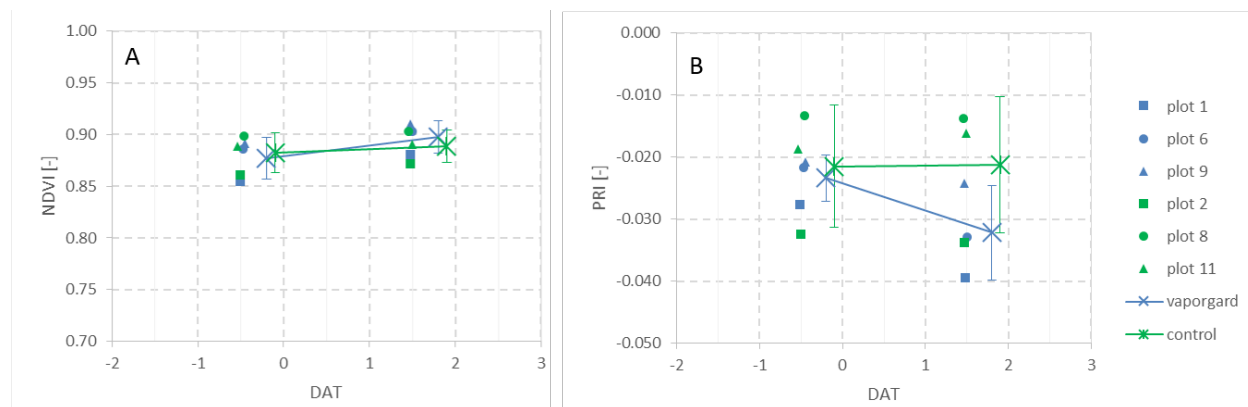**Effects on reflectance and vegetation indices**



**Figure 66: Normalized Difference Vegetation Index (NDVI, A) and Photochemical Reflectance Index (PRI, B) calculated from TOC hyperspectral measurements recorded on 9 June (DOY 160) and 11 June (DOY 162).**

Top-of-canopy reflectance and radiance on the ground were measured before (9 June) and after (11 June) for the Vapor Gard treatment. Ground measurements of canopy reflectance confirmed that the transparent Vapor Gard did not affect reflectance or absorbance of the canopy. This was also confirmed in various greenness-related vegetation indices that all did not show any changes (see e.g. NDVI in Figure 66, A). NDVI values did not change after the treatment but stayed rather constant for both the control and Vapor Gard plots (Figure 66, A) and no significant differences between control and treated plot could be detected by *HyPlant* recordings (Figure 68, A).

PRI showed comparable values for the control and Vapor Gard plots before the treatment was applied (Figure 66, B). PRI values of Vapor Gard plots decreased after the treatment and showed lower (more negative) values compared to the control plots. Even though absolute values of PRI are different from *HyPlant* and ground measurements, the significantly lower PRI values of the Vapor Gard plots after the treatment is present in both ground (Figure 66, B) and airborne measurements (Figure 67, B, Table 26).
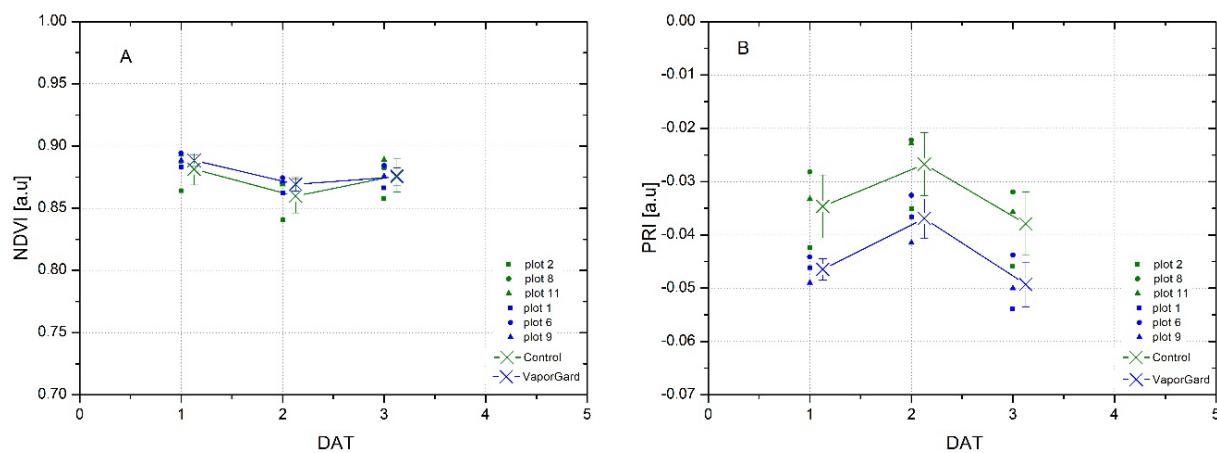
**Figure 67: Normalized Difference Vegetation Index (NDVI, A) and Photochemical Reflectance Index (PRI, B) calculated from *HyPlant* measurements recorded on 11–13 June. Vapor Gard treated plots are indicated in blue, control plots are in green.**

**Effect on fluorescence**
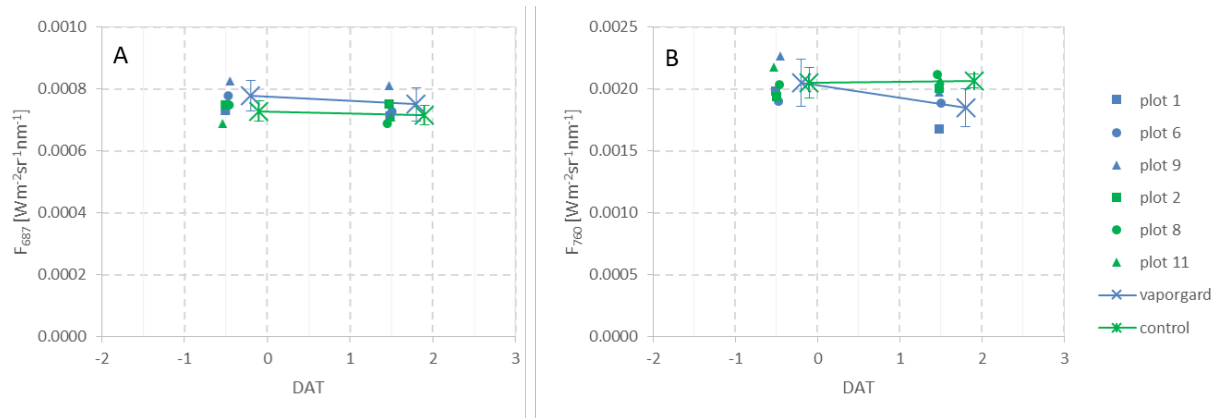


**Figure 68: Sun-induced fluorescence at 687 ($F_{687}$, A) and at 760 nm ($F_{760}$, B) calculated from TOC hyperspectral measurements recorded on 9 June (DOY 160) and 11 June (DOY 162).**

Red fluorescence ($F_{687}$) showed comparable values for the control and treated plot before and after the treatment (Figure 68, A) and only a slight difference for the following days after treatment for *HyPlant* data (Figure 69, A).

Absolute values of $F_{760}$ from *HyPlant* are slightly higher than TOC measurements from the ground (Figure 68, B and Figure 69, B). $F_{760}$ values from ground showed a slight reduction after the Vapor Gard treatment, which is in line with the observations from *HyPlant*, where Vapor Gard plots showed slightly lower values of $F_{760}$ on 11 June than for the control plots. However, this decrease in far-red fluorescence cannot be confirmed for the following days after the treatment (Figure 69, B; Table 26).



**Figure 69: Sun-induced fluorescence at 687 nm ($F_{687}$, A) and at 760 nm ($F_{760}$, B) calculated from *HyPlant* measurements recorded on 11–13 June. Vapor Gard treated plots are denoted on blue, control plots are green.**
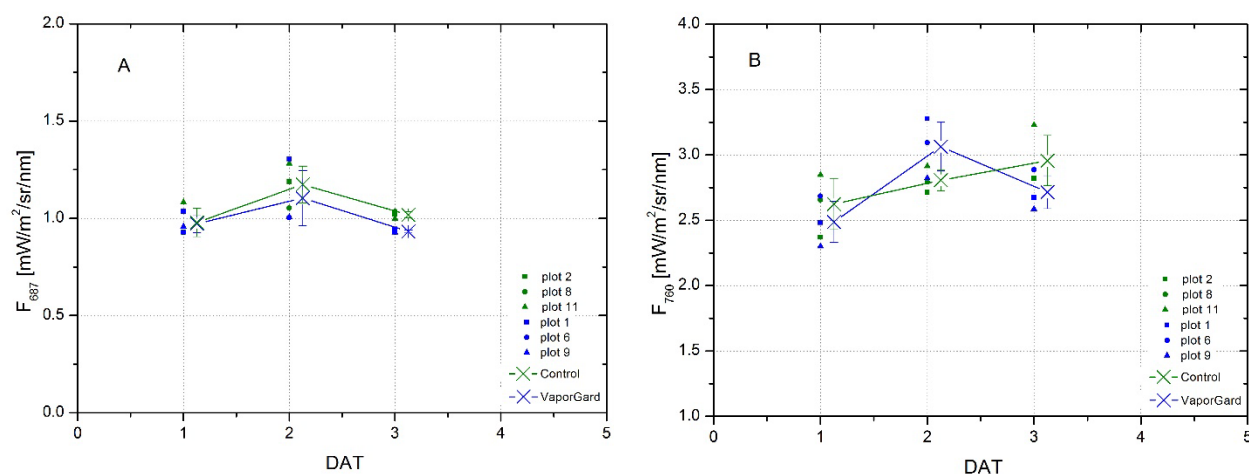
**Effect on gas exchange**

The $CO_2$ flux values derived from the gas-exchange chamber measurements on 11 June are presented in Figure 70. Ecosystem respiration fluxes (Reco) were significantly higher for Vapor Gard than for the control plots (Figure 70, A). Net Ecosystem Exchange (NEE) were less negative for the Vapor Gard than for the control plots, meaning that the assimilation rates are higher than the respiration (Figure 70, B). An exception is Vapor Gard plot 1, which showed positive NEE values, meaning respiration was higher than assimilation rates (data not shown). Nevertheless, GPP values of Vapor Gard plots are lower than for the control plots for the day after the treatment (Figure 70, C). The same is the case for the evapotranspiration. $H_2O$ flux of the control plots is slightly smaller than for the control plots (Figure 70; D).
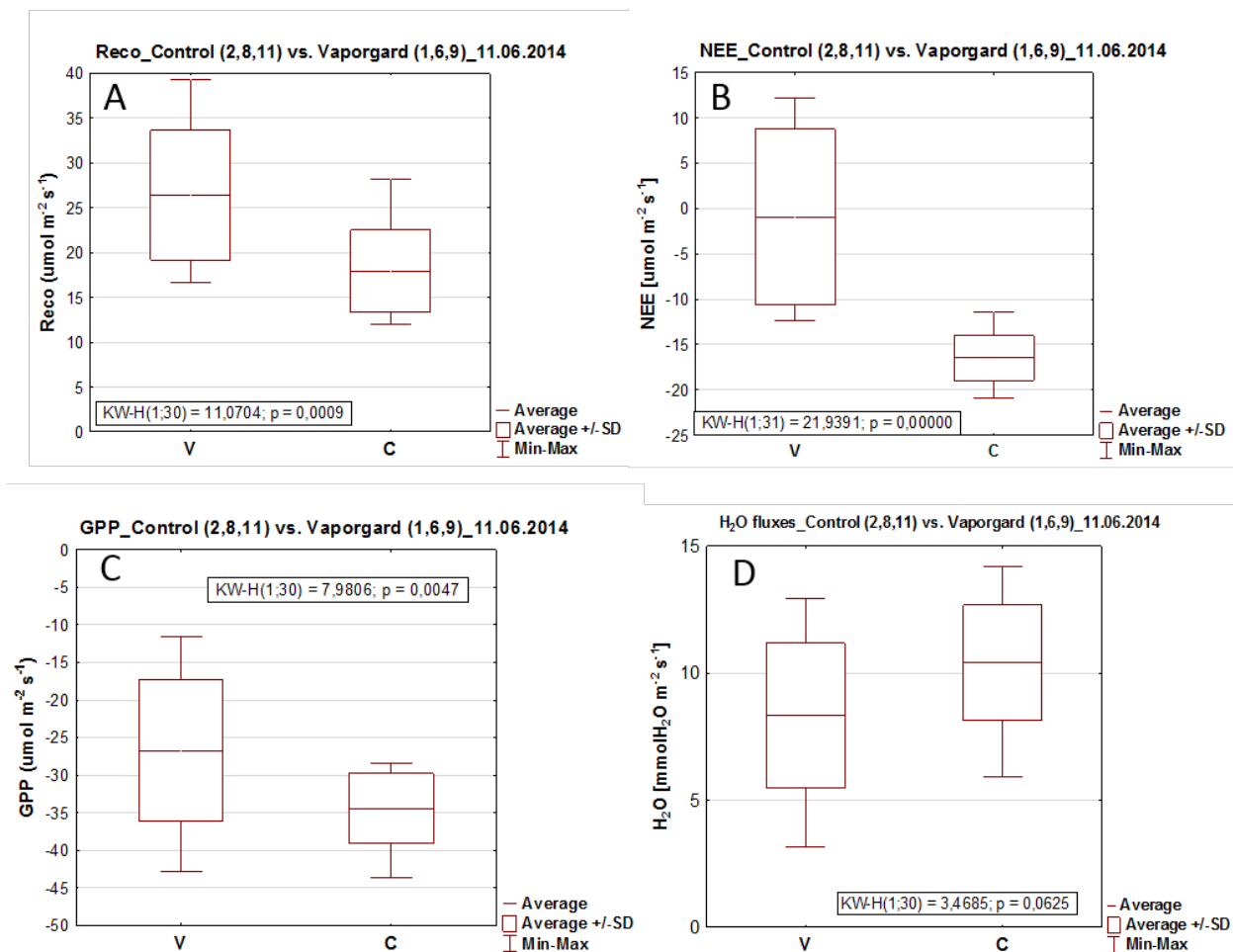
**Figure 70: Ecosystem Respiration (Reco, A), Net Ecosystem Exchange (NEE, B), Gross Primary Productivity (GPP, C) and evapotranspiration (H$_2$O fluxes, D) of three control (C) and Vapor Gard (V) treated plots. Fluxes were recorded with the gas exchange chambers on 11 June 2014, one day after the Vapor Gard treatment.**

**Effect on surface temperature**

The treatment experiment was recorded with the TASI sensor in parallel to the *HyPlant* overpasses. A map of the temperature in Kelvin is presented in Figure 71. The temperature of the Vapor Gard treated plots is 0.6 °K higher than the temperature of the control plots on the first days after treatment, while on the third day after the treatment this difference is reduced to 0.3 °K (Figure 72).
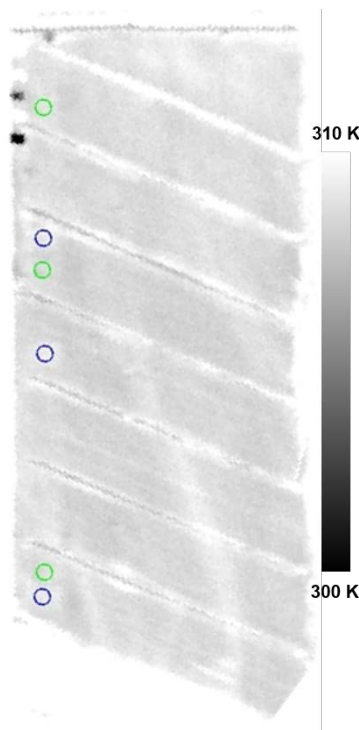
**Figure 71: Temperature in °K from TASI recorded on 11 June 2014. Regions of interest are marked blue for the TASI treated plots and green for the three control plots.**
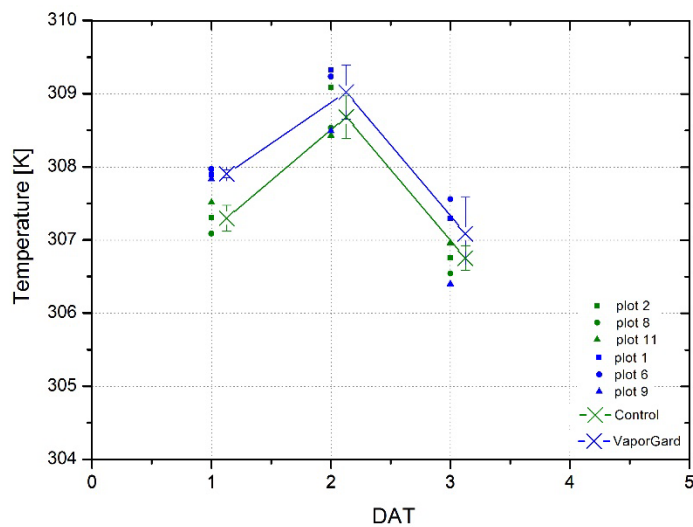


**Figure 72: Temperature in °K of the TASI recordings on 11–13 June, one to three days after the treatment. Vapor Gard treated plots are in blue, control plots are in green. Single symbols indicate the value of each plot, crosses the mean and standard deviation of all three plots.**

### 6.3.4 Effect of Paraquat

**Effects on vegetation indices and fluorescence**

On the morning of 12 June, plot number 12 was treated with the chemical **Paraquat**. The treatment showed an immediate effect. There was severe damage to the photosynthetic aperture accompanied by the breakdown of chlorophyll molecules in the leaves shortly after the treatment, which could also be observed by the chlorophyll indices, such as NDVI and MTCI from TOC ground measurements (Figure 73 A, B). Both indices dropped within the first two days after treatment to almost half of the values of the control plot and decreased even further within the following measurement days. The quick destruction of chlorophyll molecules is supported by the NDVI *HyPlant* measurements (Figure 59), which showed a drop by almost 50% within 30 hours after the Paraquat treatment (Table 26). A decrease in the PRI was detected by *HyPlant* and TOC ground measurements immediately after the application (Figure 73 B; Table 26).
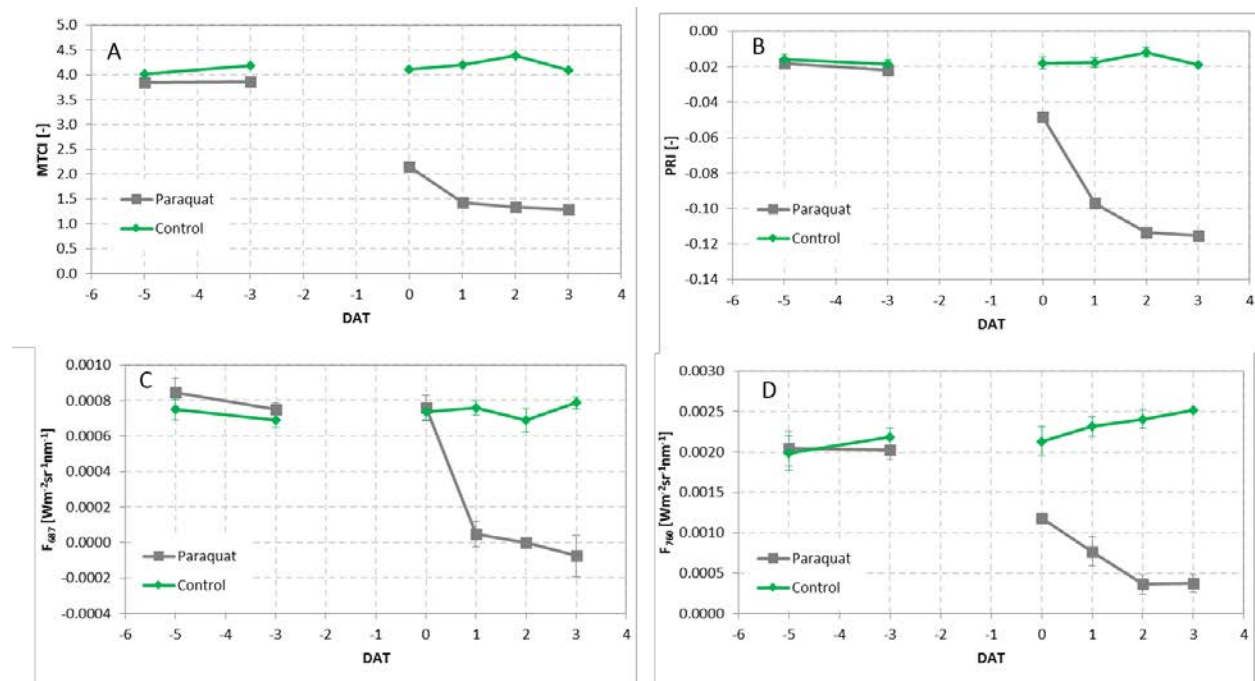


**Figure 73: Temporal changes of the MERIS terrestrial chlorophyll index (MTCI, A), the photochemical reflectance index (PRI, B) and the red ($F_{687}$, C) and far-red fluorescence ($F_{760}$, D) in the plots 11 (control) and 12 (Paraquat). Data are derived from TOC ground measurements.**

Far-red fluorescence values dropped immediately after the treatment by almost half (Figure 73 D) for the ground measurements and by 18% for the *HyPlant* measurements (Table 26). For both *HyPlant* and ground measurements, a significant decrease of the red fluorescence ($F_{687}$) could be detected one day after the treatment (Figure 73 C; Table 26).

However, in retrospect, the dose of the Paraquat treatment was just too high, and the fast and uncontrolled destruction of all components of the photosynthetic machinery restricts the physiological

meaning that can be attached to the fluorescence or PRI values. Thus, we will not discuss them in more depth here.

**Effect on gas-exchange**

The physiological response and a reduction of the photosynthetic rate of the treatment could be also observed immediately. No GPP flux could be detected after the Paraquat treatment, and no recovery of the grassland was observed within the time window of the experiment (Figure 74).
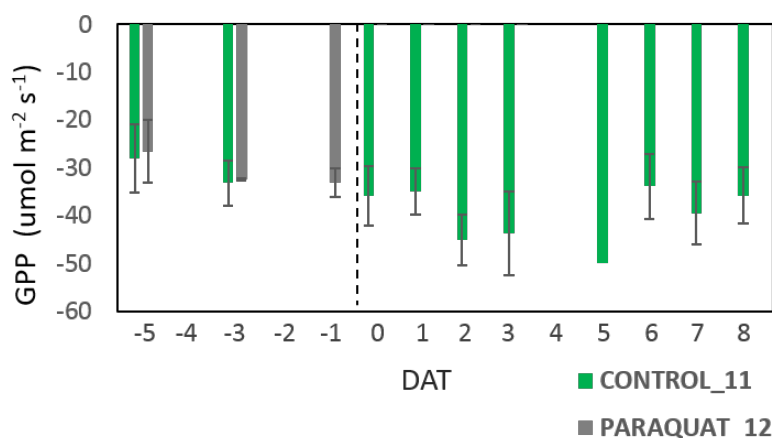


**Figure 74: Gross Primary Productivity (GPP) of control (plot 11) and Paraquat-treated plot (plot 12). Time of the treatment is indicated with a dotted line.**

## 6.3.5  Effect of different doses on Dicuran treatment

The different doses of Dicuran (24 ml, 6 ml, 3 ml, and 1.5 ml) were applied on different days to the single plots (Figure 57, Table 23). Hence, the measurement results were normalized by the day of treatment.

**Effects on Vegetation indices**

The application of the different doses of Dicuran caused a gradual chlorophyll degradation that became visible 2 days after the application in a gradually decreasing MTCI (Figure 75). This chlorophyll breakdown continued until about 6 days after the treatment (Figure 75). For the lower dose treatments (6 ml, 3 ml, and 1.5 ml), the plants started to recover, and the MTCI gradually increased again showing the recovery and newly synthesized chlorophyll at the lower doses. For the high-dose treatment of 24 ml Dicuran, no sign of chlorophyll synthetisation could be found either from the ground and airborne retrieved chlorophyll vegetation indices such as MTCI (Figure 75) and NDVI (Figure 76) or from the destructive chlorophyll analyses (Table 25).

| | Doc.: Final Report | | |
|---|---|---|---|
| | Date: 25-09-2015 | Issue: 1 | Revision: 0 |
| | Ref.: ESA Contract No. 4000107143/12/NL/FF/lf | | Page: 107 / 132 |

**JÜLICH**
FORSCHUNGSZENTRUM
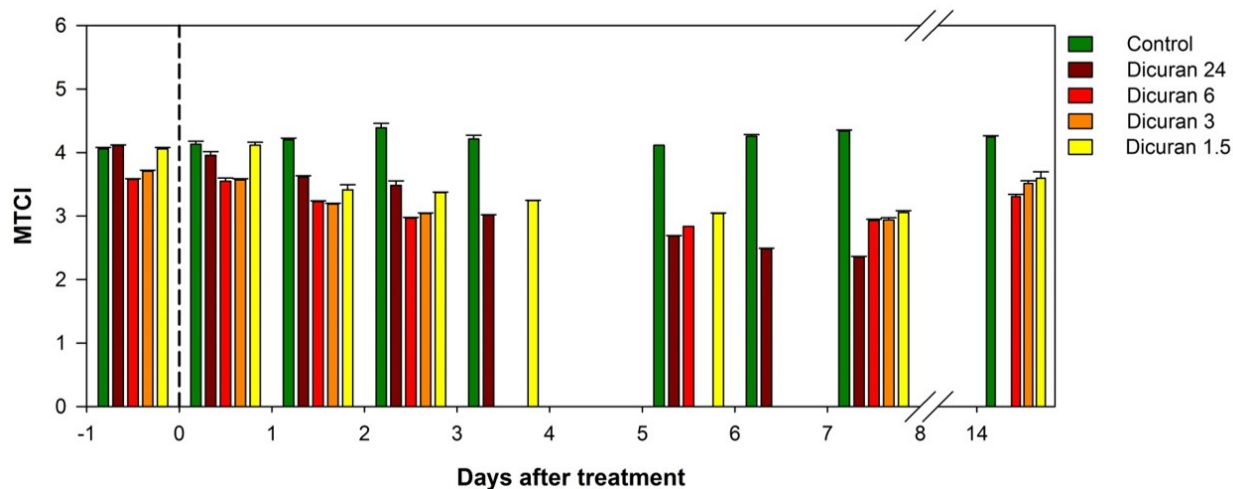
**Figure 75: Temporal courses of MERIS Terrestrial Chlorophyll Index (MTCI) normalized by day of different treatment. The treatment covered different doses of Dicuran: 24 ml, 6 ml, 3 ml, and 1.5 ml. Data are derived from TOC ground measurements.**
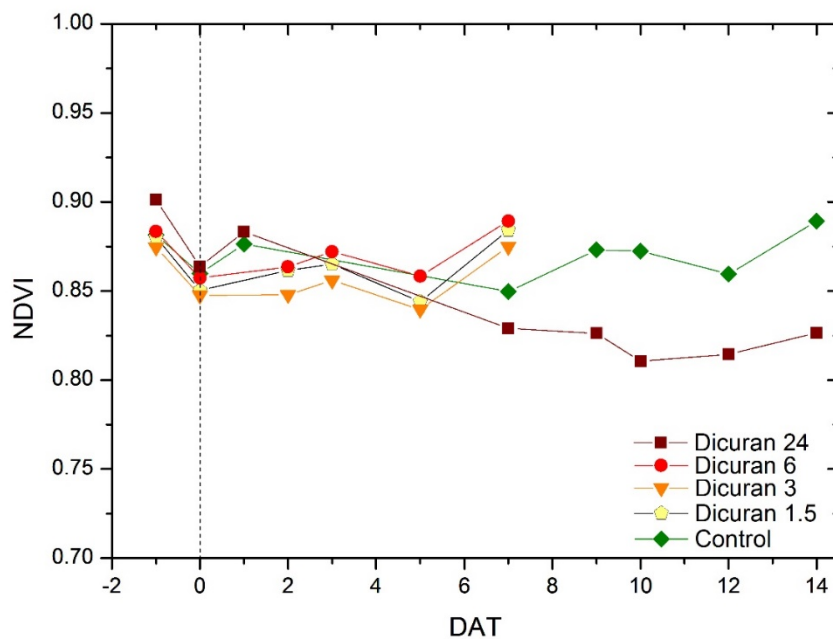


**Figure 76: Temporal courses of Normalized Difference Vegetation Index (NDVI) normalized by day of different treatment. The treatment covered different doses of Dicuran: 24 ml, 6 ml, 3 ml, and 1.5 ml. Data are derived from *HyPlant* measurements.**

**Table 25: Averaged chlorophyll a and chlorophyll b [µg/gFW] of the destructive chlorophyll samples for the control and the different Dicuran treatments: 24 ml, 6ml, 3ml, and 1.5 m.**

| DAT | Control | | Dicuran 24 ml | | Dicuran 6 ml | | Dicuran 3 ml | | Dicuran 1.5 ml | |
|---|---|---|---|---|---|---|---|---|---|---|
| | Chl a | Chl b | Chl a | Chl b | Chl a | Chl b | Chl a | Chl b | Chl a | Chl b |
| -1 | | | | | 1583 | 589 | 1583 | 594 | 1590 | 582 |
| 0 | 1880 | 717 | 1596 | 619 | 1356 | 510 | 1529 | 580 | 1504 | 576 |
| 1 | 1610 | 595 | 1580 | 617 | 1337 | 531 | 1422 | 571 | 1420 | 556 |
| 2 | 1662 | 609 | 1358 | 516 | 1467 | 577 | 1447 | 581 | 1349 | 528 |
| 3 | 1612 | 603 | 1485 | 583 | 1386 | 550 | 1304 | 537 | 1315 | 527 |
| 4 | | | 1411 | 543 | | | | | | |
| 5 | 1634 | 586 | 1315 | 510 | 1305 | 513 | 1322 | 529 | 1321 | 520 |
| 6 | 1702 | 625 | 1184 | 485 | | | | | | |
| 7 | 1766 | 639 | **1303** | **546** | 1324 | 501 | 1376 | 520 | 1412 | 534 |



**Figure 77: Temporal courses of the Photochemical Reflectance Index (PRI) normalized by day of different treatment. The treatment covered different doses of Dicuran: 24 ml, 6 ml, 3 ml, and 1.5 ml. Data are derived from TOC ground measurements.**

The PRI showed an initial increase after the treatment for all doses (Figure 77, Figure 78), which may be linked to the functional block of electron transport by Dicuran. The gradual decrease in PRI for the following days is in parallel to the chlorophyll breakdown, suggesting that this gradual phase is caused by the sensitivity of PRI to chlorophyll content.
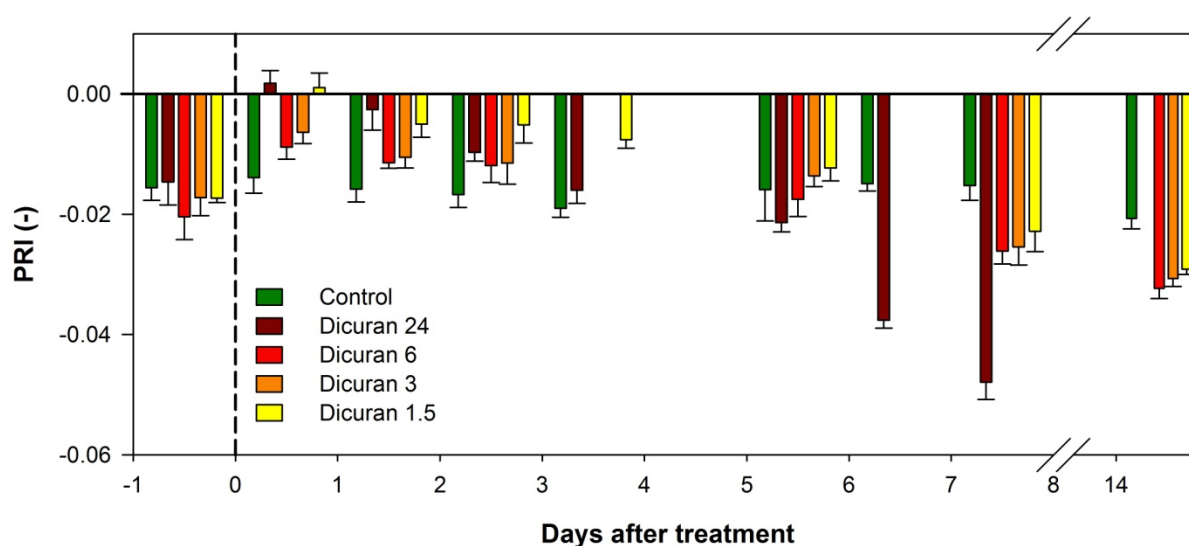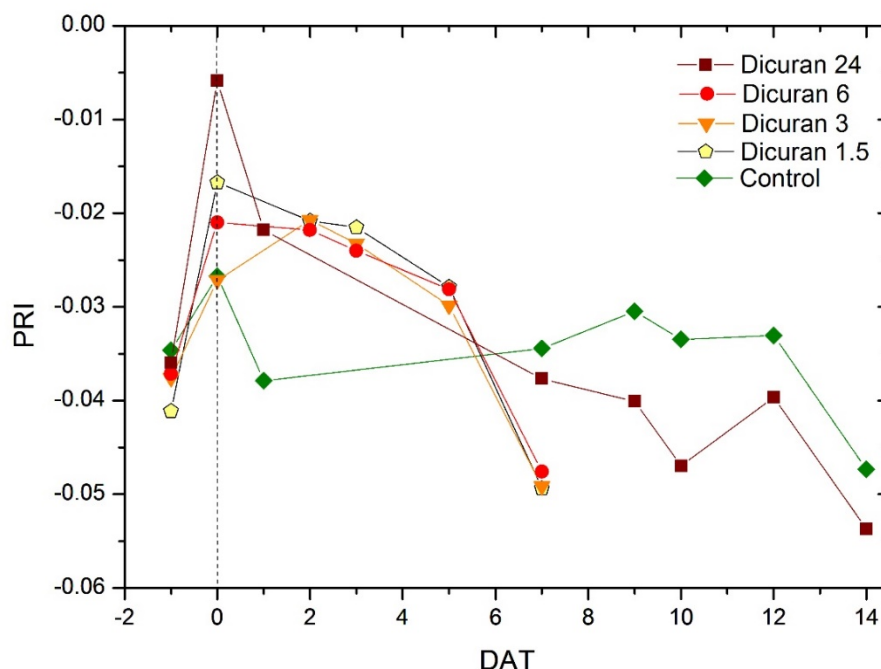
**Figure 78: Temporal courses of the Photochemical Reflectance Index (PRI) normalized by day of different treatment. The treatment covered different doses of Dicuran: 24 ml, 6 ml, 3 ml, and 1.5 ml. Data are derived from *HyPlant* measurements.**

**Effect on Fluorescence**

Both Fluorescence peaks at 687 nm ($F_{687}$) and at 760 nm ($F_{760}$) showed an immediate increase only a few hours after the application. The treatment with the highest doses of 24 ml Dicuran caused an increase of $F_{687}$ from 0.8 to 1.8 mW m$^{-2}$ sr$^{-1}$ nm$^{-1}$ in less than 3 hours after the treatment for the ground measurements (Figure 79) and comparable results for *HyPlant* measurements (Table 26; Figure 81 A). For both airborne and ground measurements, red fluorescence ($F_{687}$) decreased gradually in the following days (Figure 79, Figure 81 A). Far-red fluorescence ($F_{760}$) showed a temporal course comparable to that of red fluorescence ($F_{687}$). More than double the values of $F_{760}$ showed only hours after the treatment and gradually decreased again over the following days (Figure 80, Figure 81 B). All lower treatments showed an increase of the both fluorescence peaks hours after the application treatment (Figure 79, Figure 80, Figure 81 A, B). The highest $F_{760}$ values appeared two to three days after the treatment (Figure 80, Figure 81 A, B). However, fluorescence values of the lower treatment doses reached the initial (pre-treatment) levels fasters than the high-dose treatment (Figure 81 A, B).
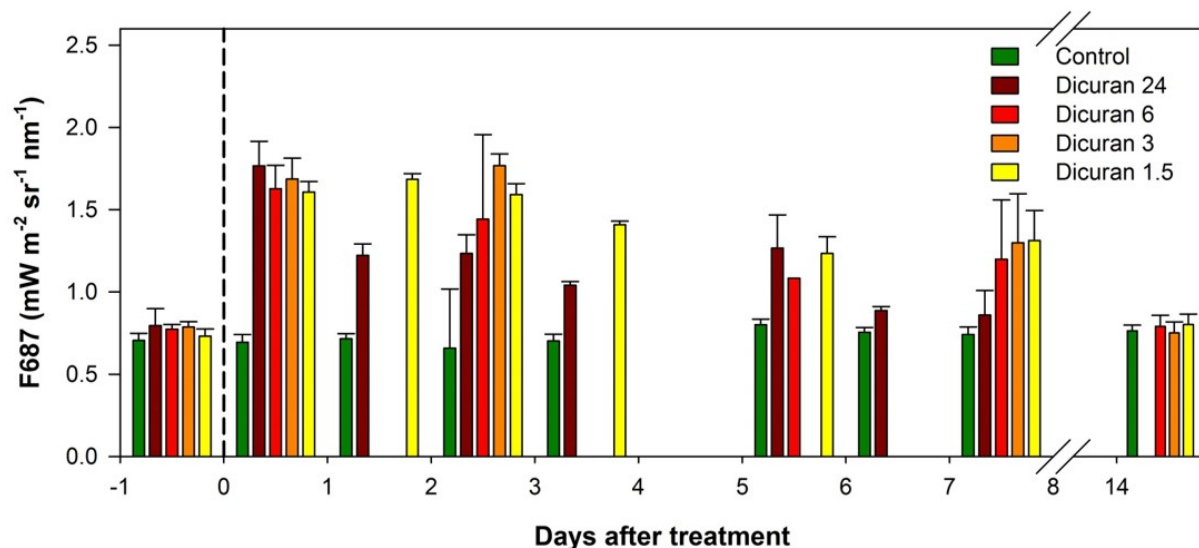
**Figure 79 Temporal courses of fluorescence at 687 nm ($F_{687}$) normalized by day of different treatment. The treatment covered different doses of Dicuran: 24 ml, 6 ml, 3 ml, and 1.5 ml. Data are derived from TOC ground measurements.**



**Figure 80: Temporal courses of fluorescence at 760 nm ($F_{760}$) normalized by day of different treatment. The treatment covered different doses of Dicuran: 24 ml, 6 ml, 3 ml, and 1.5 ml. Data are derived from TOC ground measurements.**
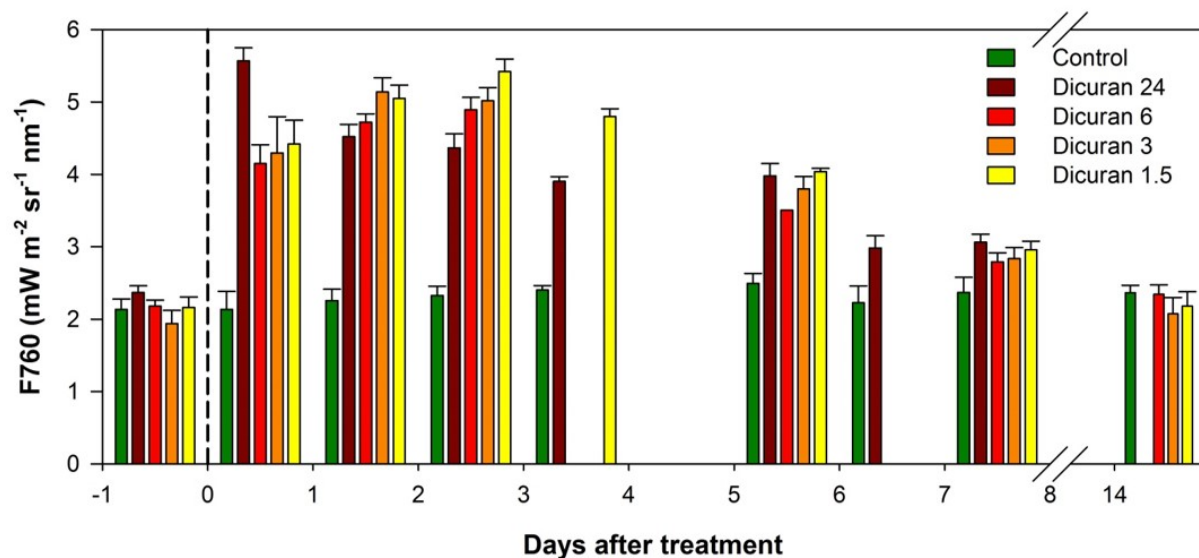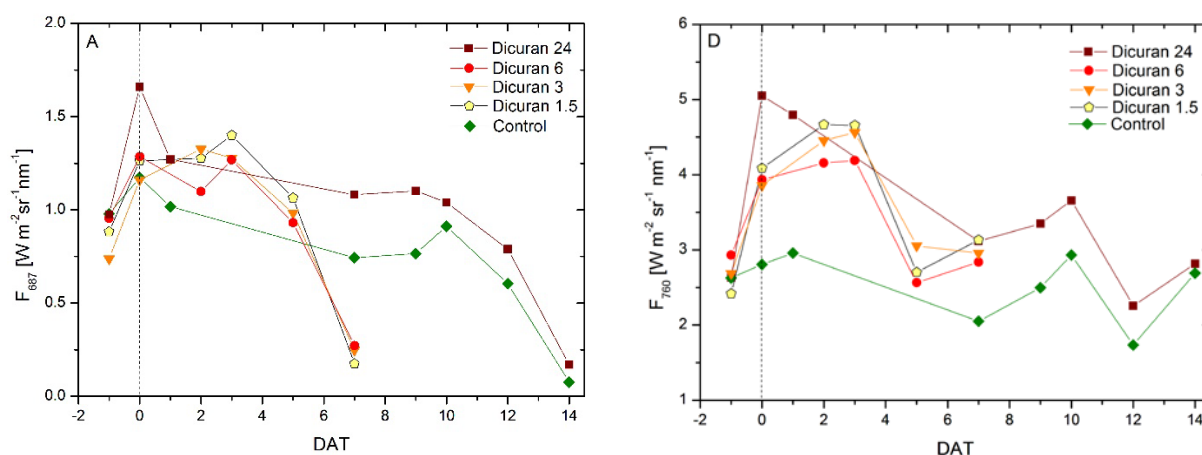
**Figure 81: Temporal courses of fluorescence at 687 nm (F$_{687}$, A) and at 760 nm (F$_{760}$, B) normalized by day of different treatment. The treatment covered different doses of Dicuran: 24 ml, 6 ml, 3 ml, and 1.5 ml. Data are derived from *HyPlant* measurements.**

**Effect on gas exchange**

Gross Primary Productivity (GPP) is presented as the difference between GPP of the control plots and GPP of the treated plots, normalized by the day of different treatment (Figure 82). The GPP data showed an immediate decrease at all doses. The GPP of the three low-dose treatments gradually recovered and reached initial values 6 to 7 days after treatment (Figure 82 A–C). In the high-dose treatment (Dicuran 24; Figure 82 D), the GPP dropped further, indicating a permanently destroyed photosynthetic apparatus that was not able to recover from the treatment, and no new chlorophyll synthesizing could compensate for the destruction caused by the high dose of Dicuran.
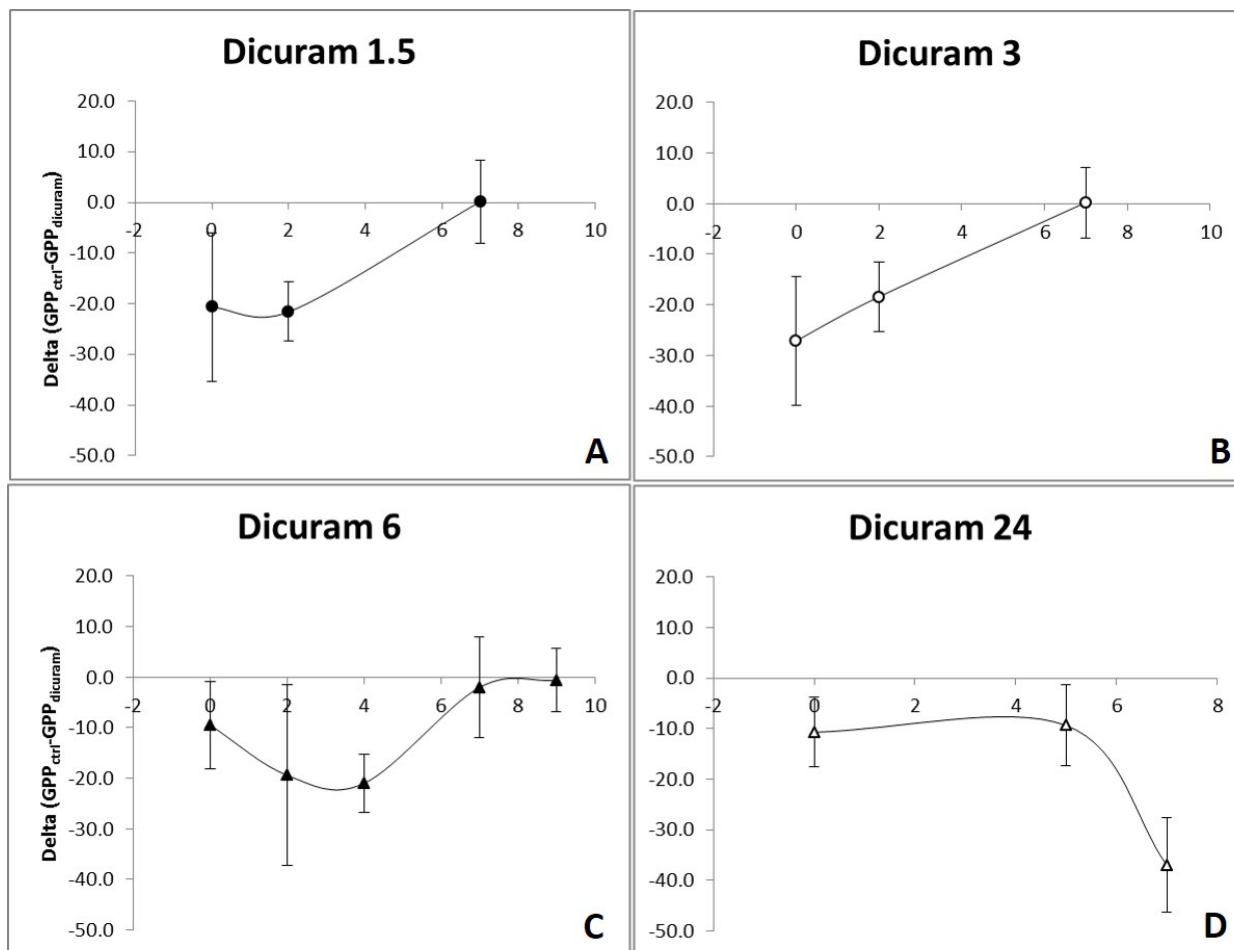
**Figure 82: Gross Primary Productivity normalized by day of different treatment. The GPP is presented as delta GPP, the difference between GPP of the control plot and GPP of the treated plot. The treatment covered different doses of Dicuran: 1.5 ml (A), 3 ml (B), 6 ml(C), and 24 ml (D).**

**Effect on Temperature**

The difference from absolute temperature values from treated plot and control plots are presented in Figure 83. The plot treated with the high Dicuran dose showed an increase of the temperature of 0.8 K for the day after the treatment and further increased up to 1.5 K seven days after the treatment. Than the temperature decreased again by 0.5 K. The lower doses treatment showed an increase of the temperature up to 1.1 K and 0.7 K respectively. No measurements were taken for further days in lower doses. Therefore, it is not possible to evaluate whether the temperature would decrease in a similar way as for the high dose treatment.
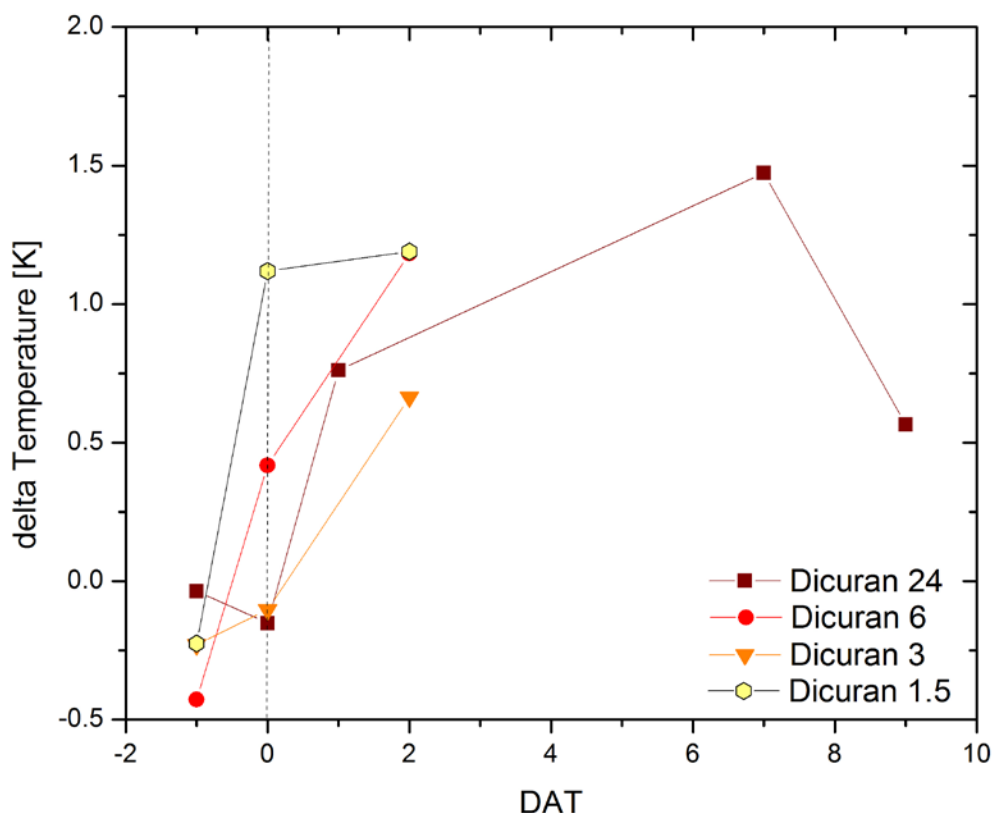


**Figure 83: Temporal courses of the canopy temperature normalized by day of different treatment. Values represent the difference in Temperature in Kelvin [K] between each treated plot and the control plots. The treatment covered different doses of Dicuran: 24 ml, 6 ml, 3 ml, and 1.5 ml. Data are derived from TASI measurements.**

## 6.4 Synopsis of the results – an overview on the main effect of the four treatments

In this chapter, we provide a synopsis and overview of the main results from the four physiological treatments.

2. For the Kaolin-treated plots, surface reflectance was greatly increased and significant change in most vegetation indices were observed. Values of $F_{687}$ were greatly reduced after the Kaolin treatment by more than 50% (Figure 59 C, Table 26).

3. The Vapor Gard treated plots show no difference in surface reflectance and greenness-related vegetation indices. However, more negative PRI values could be detected for the plots treated with Vapor Gard (Figure 59, B; Table 26). Red-fluorescence ($F_{687}$) was mainly unaffected by Vapor Gard (Figure 68 and Figure 59 C,). Far-red fluorescence ($F_{760}$) (Figure 68, Figure 59 D; Table 26) showed only a small reduction one day after the treatment but no conclusive results for the following days after treatment.

4. The Paraquat treatment must be discussed with care as it triggered a rapid pigment breakdown followed by plant death within 1½ days. Six hours after the treatment, a clear destruction of chlorophyll molecules was already visible (reduction of the NDVI by 17%). This destruction continued rapidly, and 30 hours after the application, NDVI was only 50% of the initial value (Table 26). The reduction in chlorophyll also caused decrease of $F_{760}$ with the same proportionality, an 18% reduction after 6 hours, and 51% after 30 hours (Table 26). Fluorescence at 687 nm ($F_{687}$) shows a slightly different temporal dynamic. $F_{687}$ values increased by 8% 6 hours after the treatment and showed a reduction of 76% 30 hours after the treatment. Thus, the rapid chlorophyll breakdown dominated the observations, masking potential physiological effects.

5. The high-dose treatment of Dicuran (24ml) resulted in an immediate increase of both fluorescence peaks ($F_{760}$ and $F_{687}$), while pigment levels remained unaffected. $F_{760}$ showed almost double values 6 hours after the treatment and still 80% higher values 30 hours after the treatment. The treatment effect was slightly less pronounced in the $F_{687}$, with an increase of 69% 6 hours after the treatment and still 30% higher $F_{687}$ values 30 hours after the application (Table 26). The PRI increased immediately after the treatment; however no changed in NDVI were detected the first 30 hours after the Dicuran 24 treatment.

**Table 26: Fluorescence ($F_{687}$ and $F_{760}$) in [mW/m²/sr/nm], NDVI, and PRI values of the different treated and control plots on 11–13 June. Kaolin and Vapor Gard treatments were compared with the control plots. For Paraquat and Dicuran, relative differences were calculated comparing the untreated plots on 11 June with the treated plots on 12 and 13 June. Comparisons with the control plots, however, would yield very similar results. No percentage differences were given for PRI because its range is clearly defined; therefore, no relative differences can be expressed.**

| | Treatment | 11 June | 12 June | 13 June |
|---|---|---|---|---|
| | | | | |
| **$F_{687}$** | Control | 0.98 ± 0.07 | 1.17 ± 0.09 | 1.02 ± 0.02 |
| | (1) Kaolin | 0.38 ± 0.10 [+1 day] | 0.48 ± 0.14 [+2 days] | 0.38 ± 0.07 [+3 days] |
| | (2) Vapor Gard | 0.97 ± 0.05 [+1 day] | 1.10 ± 0.14 [+2 days] | 0.93 ± 0.01 [+3 days] |
| | (3) Paraquat | 0.99 (**100%**) | 1.07 (**108%**) [+6 hours] | 0.24 (**24%**)[+30 hours] |
| | (4) Dicuran 24 | 0.98 (**100%**) | 1.66 (**169%**) [+6 hours] | 1.27 (**130%**) [+30 hours] |
| | | | | |
| **$F_{760}$** | Control | 2.63 ± 0.20 | 2.81 ± 0.08 | 2.95 ± 0.19 |
| | (1) Kaolin | n.a. | n.a. | n.a. |
| | (2) Vapor Gard | 2.49 ± 0.16 [+1 day] | 3.06 ± 0.18 [+2 days] | 2.72 ±0.13 [+3 days] |
| | (3) Paraquat | 2.41 (**100%**) | 1.97 (**82%**) [+6 hours] | 1.18 (**49%**) [+30 hours] |
| | (4) Dicuran 24 | 2.63 (**100%**) | 5.05 (**192%**) [+6 hours] | 4.80 (**182%**) [+30 hours] |
| | | | | |
| **NDVI** | Control | 0.88 ± 0.01 | 0.86 ± 0.01 | 0.88 ± 0.01 |
| | (1) Kaolin | 0.67 ± 0.02 **(76%)** | 0.65 ± 0.02 **(76%)** | 0.70 ± 0.03 **(80%)** |
| | (2) Vapor Gard | 0.89 ± 0.00 | 0.87 ± 0.01 | 0.88 ± 0.01 |
| | (3) Paraquat | **0.87 (100%)** | **0.73 (83%)** | **0.45 (51%)** |
| | (4) Dicuran 24 | 0.90 | 0.86 | 0.88 |
| | | | | |
| **PRI** | Control | -0.035 ± 0.006 | -0.027 ± 0.006 | -0.038 ± 0.006 |
| | (1) Kaolin | n.a. | n.a. | n.a. |
| | (2) Vapor Gard | -0.046 ± 0.002 | -0.037 ± 0.004 | -0.049 ± 0.004 |
| | (3) Paraquat | -0.043 | -0.051 | -0.092 |
| | (4) Dicuran 24 | -0.036 | -0.006 | -0.022 |

# 7 Discussion – revisiting the results and the hypothesis

## 7.1 Reduction of effective PAR – Kaolin treatment

Because the application of Kaolin clearly increased reflectance at the leaf surfaces, it can be assumed that effective PAR at the photosystems was reduced. The Kaolin agent is non-toxic, and we could confirm that there were no signs of pigment degradation.

A reduction of the effective PAR at the photosystems should linearly reduce the fluorescence emission of both peaks, which can only be confirmed for the red fluorescence ($F_{687}$). Fluorescence at 760 nm cannot be interpreted due to its high sensitivity to reflectance changes and brightness correction of the retrieval.

*Hypothesis 1a [fluorescence of both peaks should be reduced as a result of the reduced effective PAR]*

⇨ *can only be confirmed for the red fluorescence peak*

PRI greatly increased after the Kaolin treatment. However, PRI cannot be interpreted for this treatment because Kaolin had on green reflectance. Therefore, the reference wavelength at 570 nm was strongly affected. Thus, the increase of PRI is most likely related to the changes in surface reflectance and cannot be interpreted relative to the degree of non-photochemical energy dissipation.

*Hypothesis 1b [Additionally, PRI should be reduced, indicating the lower high-light stress]*

⇨ *can neither be confirmed nor rejected because the PRI is not reflecting NPQ changes due to its great sensitivity to reflectance changes*

## 7.2  Reduction of stomatal conductance – Vapor Gard treatment

The application of Vapor Gard had an effect on canopy gas exchange. Thus, our treatment could be interpreted as comparable to mild drought conditions, where stomata limit leaf level $CO_2$ and $H_2O$ exchange. The decrease (more negative values) of PRI may indicate an activation of non-photochemical quenching mechanisms due to the stomatal limitation. The red-fluorescence was mainly not affected by Vapor Gard, while the far-red fluorescence showed only a slight reduction only the day after treatment. However, the differences are weak and statistically not significant. Nevertheless, the direction of this response and the decrease of the two fluorescence peaks is in line what was found previously (Damm *et al.* 2010, Schickling *et al.* 2016, Ac *et al.* 2015). We could, however, not confirm nor reject the view that the red fluorescence peak is more sensitive to the mild stomatal limitation of photosynthesis as our treatment and the response in fluorescence were too weak to provide conclusive data here.

*Hypothesis 2 [stomatal closure will decrease fluorescence emission. Greater decrease is expected in the red fluorescence emission]*

⇨ *Slight decrease of far-red fluorescence can be confirmed even though the stronger effect of the fluorescence emission cannot be confirmed because of the subtle response to the mild stress*

## 7.3  Block of electron transport at photosystem I – Paraquat treatment

The application of Paraquat did not show the expected results because the mode of action of this agent was much stronger than expected. Paraquat resulted in the fast and uncontrolled destruction of photosynthetic pigments. We assume that this pigment breakdown was accompanied by a destruction of the photosystems and the photosynthetic machinery as a whole. Destruction started within hours of the application and plants were white and dead 1 day after the treatment. Thus, we can only interpret the results of this treatment to better understand the link between total amount of chlorophyll and sun-induced fluorescence. Unfortunately no physiological meaning can be attached to the fluorescence or PRI values, and we are not able to discuss our hypothesis of stress-related downregulation here.

*Hypothesis 3 [Paraquat causes an immediate and strong increase of the far-red fluorescence after the application and in a longer time frame (hours to days), undefined changes in red and far-red fluorescence and the PRI because of the destruction of the photosynthetic machinery]*

⇨ *can neither be confirmed nor rejected because the dose of Paraquat was too high and the mode of action too severe. We were not able to resolve the different time dynamics as hypothesised.*

## 7.4 Block of electron transport at photosystem II – Dicuran treatment

The application of Dicuran showed the expected results. The data are very clear, and the different temporal dynamics of the recovery phase give good insight into the contribution of the different components to the fluorescence parameters and the PRI. A reduction of the electron transport at photosystem II due to the Dicuran treatment resulted in a more than twofold increase emission of the red and far-red fluorescence emission, which was coupled with a decrease of the $CO_2$ uptake rate. The application of different Dicuran doses resulted in a (non-linear) increase of the absolute fluorescence signal. However, fluorescence measurements from the ground could reveal that experimental plots treated with lower doses recovered faster than plots treated with higher doses. The initial increase of PRI after the treatment for all doses, which may be linked to the functional blocking of electron transport by Dicuran. However, the gradual decrease in PRI for the following days is caused by the sensitivity of PRI to decreasing chlorophyll content.

*Hypothesis 4 [Dicuran causes greatly an immediate and strong increases of the red and far-red fluorescence emission. The effect should be reversible and initial fluorescence values should be obtained after a few days.]*

⇨ *can be fully confirmed. The dose response characteristics of the recovery underlines the validity of the results.*

# 8 Recommendation on how to include fluorescence into models

## 8.1 Conceptual considerations for including fluorescence into models

Forward modelling of photosynthesis requires the knowledge of all regulatory steps. The FLEX mission concept is designed to provide all elements to conceive of such models.

We use the conceptual model that is presented in the FLEX report for mission selection and that was used in different publications (Figure 84; Drusch *et al.* 2016). In this model we can clearly separate two steps: ① A light absorption and light reaction driven part, that is mainly governed by the biophysical properties of the canopy and the efficiency of the photosynthetic electron transport and ② a biochemical part, that is mainly driven by the efficiency of carbon fixation, i.e. the efficiency of the biochemical fixing of the enzyme RUBISCO (Figure 84).
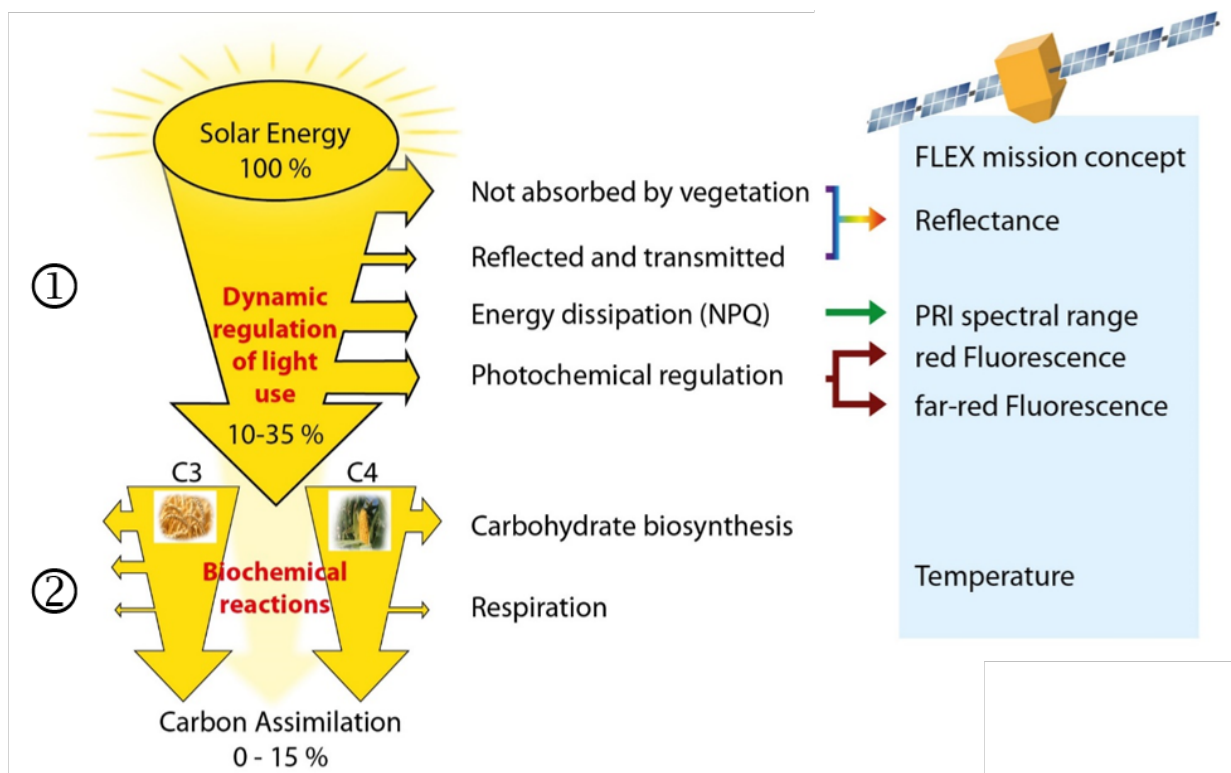


**Figure 84: Conceptual model on how to translate FLEX measurements into a forward model of photosynthetic electron transport rate (ETR) and carbon assimilation.**

In the following, we will propose a conceptual framework to show how FLEX measurements can be used to create such a forward model. Forward modelling of canopy electron transport rate (① in Figure 84) should be feasible using the level 1 products of the FLEX satellite mission, while for modelling canopy $CO_2$ uptake rates (② in Figure 84) additional information such as empirical look-up tables will be required.

Alternatively, model inversions of SCOPE may be used to calculate canopy photosynthetic electron transport rate and CO2 uptake rates. For a review on model inversion we refer to the relevant chapters of the FLEX/S3 Tandem Mission Photosynthesis Study [RD-3]

## 8.2 How to model canopy photosynthetic electron transport rate (ETR)

We propose a forward modelling of canopy electron transport rate that is analogous to the well-established calculation of PAM leaf electron transport rate (ETR).

In active Pulse Amplitude Modulation (PAM) approaches, in which leaf-electron transport rate is calculated according to eq. (22) and (23).

$$ETR = APAR \cdot \frac{\Delta F}{F_{m'}} \cdot 0.5 \qquad (22)$$

or by replacing ΔF by $F_{m}$'-F:

$$ETR = APAR \cdot \frac{F_{m'} - F}{F_{m'}} \cdot 0.5 \qquad (23)$$

In this concept, APAR is an estimate of the total absorbed photosynthetic active radiation, $\frac{\Delta F}{F_{m'}}$ describes the efficiency of electron transport at photosystem II, and the factor 0.5 assumes an equal distribution of energy between photosystem I and II.

For FLEX, we propose to use a similar concept to forward model canopy electron transport rate ($ETR_{canopy}$). For this, the following recommendations can be given based on the results of this study and taking the results from other studies into account.

FLEX canopy electron transport rate may be calculated according to eq. (24)

$$ETR_{canopy} = APAR_{chl} \cdot \varepsilon \cdot \theta \qquad (24)$$

Where $APAR_{chl}$ is the radiation that is absorbed in green, photosynthetically active plant tissue, the efficiency term ε describes the integrated canopy effective quantum efficiency at photosystem II and $\theta$ accounts for the distribution of energy between photosystem I and II, i.e. accounts for the balancing of energy between the two photosystems in linear electron transport.

These three parameters may vary depending on the functional status of the vegetation and its adaptation to the environmental conditions. The ranges of these parameters are as follows.

$$0 < APAR_{chl} < 0.84 \cdot PAR$$

$$0 < \varepsilon < 0.83$$

$$0.15 < \Theta < 0.5$$

Alternatively, ETR may be calculated as the product of absorbed photosynthetic active radiation in the green and light use efficiency (LUE), where LUE is calculated from NPQ, from the de-epoxidation state, fluorescence emission efficiency, and temperature following published relationships (e.g., Vilfan *et al.* submitted; Van der Tol *et al.* 2014).

### 8.2.1  Quantifying APAR$_{chl}$ from FLEX data

Several concepts exist to derive APAR from reflectance data (e.g. Myneni *et al.* 1997). For the FLEX mission concept, we aim to have an accurate measurement of APAR that is absorbed in photosynthetically active chlorophyll. Here the Enhanced Vegetation Index (EVI) was described by several authors as a good estimate for canopy chlorophyll content. Alternatively, a continuum removal approach may be used to quantify leaf chlorophyll content (Malenovský *et al.* 2013). This approach used the wavelength window between 650 and 720 nm and computes the 'Area under continuum removed curve Normalized to the Chlorophyll absorption Band depth between 650 and 720 nm' (ANCB$_{650-720}$). Thus, several approaches exist that exploit solely the broadband spectrometer data of the FLEX instrument, and we may want to identify the most stable approach across ecosystems for the product development of the FLEX mission.

These reflectance-based estimates of APAR$_{chl}$ may be further improved by additionally using fluorescence intensities to better constrain the estimate the APAR$_{chl}$. Far-red fluorescence was proposed several times as a good estimate of canopy APAR$_{chl}$ because deeper layer canopy elements also contribute to the F$_{740}$ signal.

In the frame of this campaign, the Kaolin experiment (chapter 6.3.2) was designed to provide experimental data on the link between effective PAR and F$_{740}$. Unfortunately, at the time of the campaign the iFLD method was used, which is still too sensitive to changes in reflectance and thus the F$_{740}$ data cannot be interpreted quantitatively. The Kaolin treatment reduced effective PAR by 26%, and reanalysing the data in the future with the established spectral fitting method may be promising.

### 8.2.2  Quantifying effective quantum efficiency at photosystem II from FLEX data

Quantifying the effective photosynthetic efficiency of light reactions is a core element of the FLEX satellite mission. The efficiency term is generally named LUE, $\mathcal{E}$, or $\frac{F_m'-F}{F_m'}$ , and needs to be determined from the fluorescence data. The campaign activity presented here provides valuable data that can be used to propose a transfer function to effective photosynthetic efficiency. We deliberately propose to determine the efficiency at photosystem II, i.e. at the very beginning of the photosynthetic electron transport so that the balance between photosystem II and photosystem I will be accounted for by the $\Theta$ term (see eq. 17 and chapter 8.2.3).

Taking the analogy with the PAM approach, effective photosynthetic efficiency can be determined by the ratio between maximum fluorescence ($F_m'$) and steady-state fluorescence (F). With FLEX, we will only be able to measure F. In this campaign activity, the application of DCMU caused a great increase in the fluorescence emission, and by taking the analogy to leaf-level measurements, DCMU should induce maximum fluorescence values ($F_m'$). Thus, in our experimental set-up we could measure $F_m'$ in the hours after DCMU application.

For example, the increase of the fluorescence signal to 180% can be interpreted as $F_m' = 1.8 \cdot F$. If we use these values, then effective quantum efficiency ($\frac{F_m'-F}{F_m'}$) would be 0.44. This value is in the right range, thus, this approach is promising to better constrain light-use-efficiency derived from the FLEX mission.

### 8.2.3 Quantifying the balance between photosystem II and photosystem I (Θ) from FLEX data

Energy may be unevenly distributed between photosystem II and photosystem I, but the energy balance between the two photosystems is actively regulated by the plants. Main physiological regulatory steps are

- State 1 / state 2 transition (i.e. a dislocation of the light-harvesting complexes between photosystem II and photosystem I)
- Constitutional non-photochemical energy dissipation (that occurs at overwintering plants and which is associated to sustained de-epoxidation of the xanthophyll pool pigments)
- Dynamic non-photochemical energy dissipation (that happens on the shorter time scales of minutes and seconds and that is used to dissipate excessive energy during stress)
- Cyclic electron transport at photosystem I (that dissipates energy at PS I and reduces the linear energy flow at the end of the electron transport chain of light reaction)

All these functional regulatory mechanisms can only precisely determined in the laboratory, and a direct quantification of these subtle changes are out of reach for the FLEX satellite mission. There is no remote sensing approach available to determine state 1 / state 2 transition or cyclic electron transport. Non-photochemical energy dissipation may be measured by the slight reflectance changes that occur around 530 nm. These changes are the basis for the PRI is the only reflectance-based measure that can be used to assess constitutional (seasonal), non-photochemical energy dissipation during cold acclimation in evergreens. This causes substantial variations in PRI, while diurnal and stress related effects are rather small and currently cannot be measured reliably by satellite based PRI measurements (Wong and Gamon 2014).

However, all these functional changes mentioned above result in an imbalance of the energy distribution between the two photosystems. Optimal photosynthetic electron transport is maintained if energy is distributed equally, i.e. as long as Θ = 0.5. In reality Θ < 0.5 and may reach values as low as 0.15 in some algae (Grzymski *et al*. 1997). As it is impossible to measure Θ directly, we propose to also explore the option of empirical LUT that can be used to read out empirical values for Θ. Such LUTs may be function of: (i) the plant functional type; (ii) the measured PRI; and (iii) a meteorological parameter that describes the environmental conditions, such as canopy temperature (derived from Sentinel-3).

## 8.3 How to use FLEX products to model canopy $CO_2$ uptake rate or GPP

Translating photosynthetic electron transport rate in light reactions to $CO_2$ uptake rates is challenging and not straight forward. The reasons for the complexity to quantitatively translate electron force in light reaction of photosynthesis to carbon uptake rates can be related to three functional processes.

- Electrons that are transported through light reactions of photosynthesis are used to build NADPH and a proton gradient across the thylakoid membrane. However, several alternative pathways and regulatory shunts exist. Thus, the stochoimetry between the NADPH molecules that are produced and the strength of the proton gradient is variable and regulated. I.e., the molecules of NADPH that are produced per electron transported in light reactions is variable and cannot be quantified precisely by remote sensing, even though sun-induced fluorescence will help to constrain the estimate.

- The proton gradient is used to drive a complex enzyme, the ATPase that uses the proton gradient to produce ATP, the second energetic unit that is needed to fix $CO_2$. The amount of protons needed to build one molecule ATP is variable and changes between 3 - 7 protons per ATP produced. Thus, this so-called coupling factor changes and is actively regulated.

- Biochemical fixation of $CO_2$ is done in the so-called Calvin Cycle, which is a complex loop of enzymatic reactions that are energized by ATP and NADPH. In theory 2 molecules of NADPH and 3 molecules of ATP are needed to fix one molecule of $CO_2$. In reality however this reaction depends on the leaf-internal $CO_2$ concentration ($c_i$). At low $c_i$ photorespiration may happen that in turn triggers a complex and energy demanding recycle reaction. Thus, in reality the amount of ATP and NADPH molecules that are needed to fix one molecule $CO_2$ are higher than the theoretical minimum.

- Last but not least there is the fundamental difference in carbon fixation in C3 and C4 plants. C4 plants, such as corn minimize photorespiration by an adapted leaf anatomy and a leaf-internal $CO_2$ concentration mechanism. C4 plants can thus achieve higher $CO_2$ fixation efficiencies can C3 plants especially in dry habitats, where leaf-internal $CO_2$ concentrations are likely to be low because of stomatal limitations.

There are various plant-physiological text books and scientific papers available on these physiological mechanisms and their regulation (we recommend Zhu *et al.* 2010 as a good review article or the excellent text book 'Plant Ecology' from Schulze).

As a bottom line the amount of electrons that need to be transported in light reaction of photosynthesis to fix one molecule of $CO_2$ varies widely. Theoretically, at least seven electrons need to be transported at photosystem II to fix one $CO_2$ molecule. In nature this 'coupling factor' is always higher and typically ranges between 10 and 30, even though even more extreme values are not seldom.

As outlines above the main environmental factors that determine this coupling factors are

- plant species or plant functional type. In reality we will generally deal with diverse plant ecosystems in each FLEX pixels, which composition should be also considered

- surface and soil temperature as ATPase and the enzymes of the Calvin Cycle are greatly temperature dependent

- evapo-tranpiratory demand, which is mainly determined by air temperature and relative humidity. This is one of the main environmental factors influencing stomatal opening, which in turn determines leaf internal $CO_2$ concentration and thus the degree of photorespiration.

Despite decade of scientific research no mechanistic transfer functions can be given here that can be used across different vegetation types. Thus, different carbon models have normally established empirical approaches to derive photosynthetic $CO_2$ uptake rate from remote sensing data (refer to chapter 4.3 in the FLEX photosynthesis study [RD-3], which gives a good overview on the different carbon models and their approach). Especially the MODIS approach (MODIS product 17) may be revisited to explore its potential to be modified and used in the FLEX product definition. This approach uses vegetation type specific transfer functions that use minimum temperatures and relative humidity estimates to constrain $CO_2$ uptake rate from the maximum potential $CO_2$ uptake rate. This MODIS product takes various data sources and thus is considered a level 4 product. For the FLEX satellite mission we should however be better than the MODIS product as FLEX can give reliable estimates of photosynthetic electron transport rate.

# 9 Recommendations for future activities

Based on the results presented in this report and the considerations made in the chapter above we want to make five recommendations for future campaign and science activities. These recommendations will help to close some knowledge gaps and will help to develop better lvl 2 products for the FLEX mission.

### 1) Develop and validate an approach to quantify the degree of non-photochemical energy dissipation overcoming the difficulties to use the PRI across plant functional types

In this study, we confirmed that PRI is a problematic parameter to measure the degree of non-photochemical energy dissipation as it is greatly affected by leaf and canopy structure. The PRI as it is calculated at the moment (i.e. simple 2 wavelength index) is greatly influenced by leaf and canopy reflectance and structure. This often overrides the subtle physiological changes.

Therefore, we propose to (i) further evaluate alternative measurement approaches of NPQ as outlines in the FLEX photosynthesis study and (ii) to start the development of a forward modelling approach to determine the degree of non-photochemical energy dissipation.

### 2) Better understand the functional meaning of variability in the two fluorescence peaks

The two fluorescence peaks clearly react differently to functional changes in photosynthetic electron transport rate. Here we also provide experimental evidence for the importance of measuring both peaks with the FLEX mission as both peak react differently to changes in APAR on the one hand and changes in photosynthetic efficiency ($\varepsilon$) and $\Theta$ on the other. However, we clearly need to better understand the different information content of the two peaks of canopy fluorescence. There is additional information coded in the two peaks than we can reflect with our current conceptual model and this knowledge is needed to develop a robust forward model for photosynthetic rates across vegetation types that have different structure.

### 3) Develop a forward model for $APAR_{chl}$

Light penetration into the canopy as well as the reabsorption of the two-peak fluorescence signal is complex, and the simple concept, that leaf and canopy chlorophyll content just effects the far-red peak leaving the red peak unaffected, does not hold true. Our results from this campaign point towards a more complicated relationship, and we would recommend further investigating these structure/function relations by (i) reanalysing existing data and (ii) experimental validation of the forward model.

The goal of future activities should be to propose a forward model for the $APAR_{chl}$ lvl 2 product of FLEX. $APAR_{chl}$ describes the total amount of 'photosynthetic active radiation that is absorbed in the canopy'. In addition a rough estimate on the vertical stratification, i.e. in with depth / leaf layer is absorbed how much light. Leaf angle distribution and vertical gradients of chlorophyll concentration may be second order effect, however, also this needs to be shown.

### 4) Develop a forward model for canopy electron transport rate using FLEX measurements

As shown in this report sun-induced fluorescence together with high performance reflectance measurements open a promising way to calculate canopy electron transport rate. However, a mechanistic forward model that is additionally validated across vegetation types is still missing. A forward model may be proposed based on the existing data, however, this model will rely on experimental data that are acquired on very few vegetation types, mainly agricultural monocultures. Thus, such a model needs to be tested and validated across structurally and functionally diverse vegetation types.

We also propose to further investigate option to obtain maximum fluorescence from natural canopies to get an estimate of effective photosynthetic efficiency ($\varepsilon$) from sun-induced, i.e. steady-state measurements. Options to derive maximum fluorescence may include measurements under extreme stress, ground application of DCMU on further experimental field sites and transfer to plant functional classes or mechanistic modelling. Such data of maximum fluorescence may be used as look-up table for FLEX product definition.

Similar approaches may be used to derive the $\Theta$ factor. This factor may be constraint by measurements of NPQ and the two fluorescence peaks. However, we are still at the beginning of our understanding here and more detailed considerations (potentially in the frame of a science study that reanalysis existing data) may be needed.

### 5) Develop a forward model for canopy $CO_2$ uptake rate using FLEX measurements and an empirical look-up-table

While canopy electron transport rate most likely still can be calculated in a forward mode (including radiative transfer modelling) the calculation of $CO_2$ uptake rates is highly species / vegetation type dependent and additionally temperature and relative humidity (or VPD) need to be taken into account. We propose to develop a look-up table (LUT) of 'ETR-GPP coupling factors'. These factors describe the conversion between ETR and GPP [electrons transported in light reaction / $CO_2$ fixed]. Such a LUT should cover the most important factors, which are according to our current knowledge: (i) plant functional type, (ii) surface temperature and (iii) vapour pressure difference (VPD). We propose to develop such a LUT as open source so that it can be further populated / refined in the course of the FLEX satellite mission.

# References

Ac, A.; Malenovsky, Z.; Olejnickova, J.; Galle, A.; Rascher, U.; Mohammed, G. (2015). Meta-analysis assessing potential of steady-state chlorophyll fluorescence for remote sensing detection of plant water, temperature and nitrogen stress. *Remote Sensing of Environment*, 168, 420–436.

Alonso L, Gomez-Chova L, Vila-Frances J, Amoros-Lopez J, Guanter L, Calpe J, Moreno J. (2008). Improved Fraunhofer Line Discrimination Method for Vegetation Fluorescence Quantification. *IEEE Geoscience and Remote Sensing Letters,* 5, 620–624.

Asrar G., Fuchs M., Kanemasu E.T., Hatfield J.L. (1984). Estimating absorbed photosynthetic radiation and leaf-area index from spectral reflectance in wheat. *Agronomy Journal,* 76, 300–306.

Berk, A.; Anderson, G. P.; Acharya, P. K.; Bernstein, L. S.; Muratov, L.; Lee, J.; Fox, M. J.; Adler-Golden, S. M.; Chetwynd, J. H.; Hoke, M. L.; Lockwood, R. B.; Cooley, T. W.; Gardner, J. A. (2005). MODTRAN5: A reformulated atmospheric band model with auxiliary species and practical multiple scattering options. *Proceedings of the Society of Photo-Optical Instrumentation Engineer*, 5655, 662–667.

Chojnicki BH, Michalak M, Acosta M, Juszczak R, Augustin J, Droesler M, Olejnik J (2010). Measurements of carbon dioxide fluxes by chamber method at Rzecin wetland ecosystem in Poland. *Polish Journal of Environmental Studies*, 19(2), 283–291.

Cogliati S, Rossini M, Julitta T, Meroni M, Schickling A, Burkart A, Pinto F, Rascher U, Colombo R. (2015). Continuous and long-term measurements of reflectance and sun-induced chlorophyll fluorescence by using novel automated field spectroscopy systems. *Remote Sensing of Environment,* 164, 270–281.

Conrad R, *et al.* (1993). Changes in yield of in-vivo fluorescence of chlorophyll a as a tool for selective herbicide monitoring. (Translated from English) *J. Appl. Phycol.* 5(5):505–516 (in English).

Damm A, Guanter L, Laurent VCE, Schaepman ME, Schickling A, Rascher U. (2014). FLD-based retrieval of sun-induced chlorophyll fluorescence from medium spectral resolution airborne spectroscopy data. *Remote Sensing of Environment*, 147, 256–266.

Damm A, Guanter L, Verhoef W, Schläpfer D, Garbari S, Schaepman ME. (2015). Impact of varying irradiance on vegetation indices and chlorophyll fluorescence derived from spectroscopy data. *Remote Sensing of Environment*, 156, 202–215.

Damm, A.; Elbers, J.; Erler, A.; Gioli, B.; Hamdi, K.; Hutjes, R.; Kosvancova, M.; Meroni, M.; Miglietta, F.; Moersch, A.; Moreno, J.; Schickling, A.; Sonnenschein, R.; Udelhoven, T.; Van der Linden, S.; Hostert, P.; Rascher, U. (2010). Remote sensing of sun-induced fluorescence to improve modeling of diurnal courses of gross primary production (GPP). *Global Change Biology,* 16, 171–186.

Dash J. & Curran P.J. (2007). Evaluation of the MERIS terrestrial chlorophyll index (MTCI). *Advances in Space Research*, 39, 100–104.

Davidson EA, Savage K, Verchot LV, Navarro R (2002). Minimizing artefacts and biases in chamber-based measurements of soil respiration. *Agriculture and Forest Meteorology,* 113, 21–37.

Dawson T.P. & Curran P.J. (1998). A new technique for interpolating the reflectance red edge position, *International Journal of Remote Sensing, 19*, 2133–2139.

Drusch, M.; Moreno, J.; Bello, U. D.; Franco, R.; Goulas, Y.; Huth, A.; Kraft, S.; Middleton, E. M.; Miglietta, F.; Mohammed, G.; Nedbal, L.; Rascher, U.; Schüttemeyer, D.; Verhoef, W. (2017). The FLuorescence EXplorer Mission Concept – ESA´s Earth Explorer 8. *IEEE Transactions on Geoscience and Remote Sensing*, 55, 1273–1284.

Frankart C, Eullaffroy P, Vernet G (2003). Comparative effects of four herbicides on non-photochemical fluorescence quenching in Lemna minor. *Environ. Exp. Bot.*, 49(2), 159–168.

Gamon JA, Peñuelas J, Field CB (1992). A narrow-waveband spectral index that tracks diurnal changes in photosynthetic efficiency. *Remote Sensing of Environment,* 41(1), 35–44.

Gamon, J. A., L. Serrano, and J. S. Surfus (1997). The photochemical reflectance index: an optical indicator of photosynthetic radiation use efficiency across species, functional types, and nutrient levels,.*Oecologia*, *112*(4), 492–501.

Gitelson, A., & M. Merzlyak, (1994). Spectral Reflectance Changes Associated with Autumn Senescence of Aesculus Hippocastanum L. and Acer Platanoides L. Leaves, *Journal of Plant Physiology*, 143, 286–292.

Grzymski J, Johnsen G and Sakshug E (1997). The significance of intracellular self-shading on the bio-optical properties of brown, red and green macroalgae. *J Phycol,* 33, 408–414.

Guanter L, Frankenberg C, Dudhia A, Lewis PE, Gomez-Dans J, Kuze A, Suto H, Grainger RG. (2012). Retrieval and global assessment of terrestrial chlorophyll fluorescence from GOSAT space measurements. *Remote Sensing of Environment,* 121, 236–251.

Guanter, L.; Rossini, M.; Colombo, R.; Meroni, M.; Frankenberg, C.; Lee, J. E.; Joiner, J. (2013). Using field spectroscopy to assess the potential of statistical approaches for the retrieval of sun-induced chlorophyll fluorescence from ground and space. *Remote Sensing of Environment*, 133, 52–61.

Haboudane D., Miller J.R., Tremblay N., Zarco-Tejada P.J., Dextraze L. (2002). Integrated narrow-band vegetation indices for prediction of crop chlorophyll content for application to precision agriculture, *Remote Sensing of Environment,* 81, 416–426.

Hoffman M., Jurisch N., Albiac Borazz E., Hagemann U., Droesler M., Sommer M., Augustin J. (2015). Automated modeling of CO2 fluxes based on periodic closed chamber measurements: A standardized conceptual and practical approach. *Agriculture and Forest Meteorology,* 200, 30–45.

Huete A.R., Didan K., Miura T., Rodriguez E.P., Gao X., Ferreira L.G. (2002). Overview of the radiometric and biophysical performance of the MODIS vegetation indices. *Remote Sensing of Environment, 83*, 195–213; Special Issue on The Moderate Resolution Imaging Spectroradiometer (MODIS): a new generation of Land Surface Monitoring].

Juszczak R, Humphreys E, Acosta M, Michalak-Galczewska M, Kayzer D, Olejnik J (2013). Ecosystem respiration in a heterogeneous temperate peatland and its sensitivity to peat temperature and water table depth. Plant and Soil, 366(1-2), 505–520.

Juszczak R., Acosta M., Olejnik J. (2012). Comparison of daytime and nighttime Ecosystem Respiration measured by the closed chamber technique on a temperate mire in Poland. *Polish Journal of Environmental Studies*, Vol. 21, 643–658.

LI-COR Application Note 129. The importance of water vapor measurements and corrections. LI-COR inc. 4421 Superior Street, Lincoln, Nebrasca, USA.

Lindberg, J. D. & Smith M. S. (1974). Visible and near infrared absorption coefficients of kaolinite and elated clays. *American Mineralogist*, 59, 274–279.

Maier SW, Günther KP, Stellmes M. (2003). Sun-Induced Fluorescence: A New Tool for Precision Farming. In: MCDONALD, M., SCHEPERS, J., TARTLY, L., VAN TOAI, T. & MAJOR, D. (eds.) Digital Imaging and Spectral Techniques: Applications to Precision Agriculture and Crop Physiology. ASA Special Publication.

Malenovský Z, Homolová L, Zurita-Milla R, Lukeš P, Kaplan V, Hanuš J, Gastellu-Etchegorry J-P, Schaepman ME. (2013). Retrieval of spruce leaf chlorophyll content from airborne image data using continuum removal and radiative transfer. *Remote Sensing of Environment*, 131, 85–102.

Meroni M, Busetto L, Colombo R, Guanter L, Moreno J, Verhoef W. (2010). Performance of Spectral Fitting Methods for vegetation fluorescence quantification. *Remote Sensing of Environment*, 114, 363–374.

Meroni M, Colombo R. (2006). Leaf level detection of solar induced chlorophyll fluorescence by means of a subnanometer resolution spectroradiometer. *Remote Sensing of Environment,* 103, 438–448.

Meroni M, *et al.* (2011). The hyperspectral irradiometer, a new instrument for long-term and unattended field spectroscopy measurements. *Review of Scientific Instruments* 82.

Meroni M, Rossini M, Guanter L, Alonso L, Rascher U, Colombo R, Moreno J. (2009). Remote sensing of solar-induced chlorophyll fluorescence: Review of methods and applications. *Remote Sensing of Environment*, 113, 2037–2051.

Myneni RB, Nemani RR, Running SW. (1997). Estimation of global leaf area index and absorbed par using radiative transfer models. *IEEE Transactions on Geoscience and Remote Sensing*, 35, 1380–1393.

Peñuelas J., Filella I., Biel C., Serrano L., Savé R. (1993). The reflectance at the 950–970 nm region as an indicator of plant water status. *International Journal of Remote Sensing,* 14, 1887–1905.

Pérez-Priego O., López-Ballesteros A., Sánchez-Cañete E.P., Serrano-Ortiz P., Kutzbach L., Domingo F., Eugster W., Kowalski A. (2015). Analysing uncertainties in the calculation of fluxes using whole-plant chambers: random and systematic errors. *Plant and Soil* , 393(1), 229–244.

Plascyk, J. A. (1975). MK II Fraunhofer Line Discriminator (FLD-II) for airborne and orbital remote-sensing of solar-stimulated luminescence. *Optical Engineering,* 14**,** 339–346.

Rascher U, *et al. (*2009). CEFLES2: the remote sensing component to quantify photosynthetic efficiency from the leaf to the region by measuring sun-induced fluorescence in the oxygen absorption bands. *Biogeosciences J1 - BG*, 6, 1181–1198.

Rouse J.W.J., Haas R.H., Schell J.A., Deering D.W. (1973). Monitoring vegetation systems in the Great Plains with ERTS. *Third ERTS Symposium, NASA* SP-351, 309–317.

Ruban AV, Rees D, Pascal AA, Horton P (1992). Mechanism of ΔpH-dependent dissipation of absorbed excitation energy by photosynthetic membranes. II. The relationship between LHCII aggregation in vitro and qE in isolated thylakoids. *Biochimica et Biophysica Acta – Bioenergetics,* 1102(1), 39–44.

Ruban AV, Wentworth M, Horton P (2001). Kinetic Analysis of Nonphotochemical Quenching of Chlorophyll Fluorescence. 1. Isolated Chloroplasts†. *Biochemistry*, 40(33), 9896–9901.

Schickling, A.; Matveeva, M.; Damm, A.; Schween, J.; Wahner, A.; Graf, A.; Crewell, S.; Rascher, U. (2016). Combining Sun-Induced Chlorophyll Fluorescence and Photochemical Reflectance Index Improves Diurnal Modeling of Gross Primary Productivity. *Remote Sensing*, 8, 574.

Schulze, E.D., Beck, E., Müller-Hohenstein K.(2005). Plant Ecology, Springer, ISBN 978-3-540-20833-4, 702 p.

Sims, D., & J. Gamon (2002). Relationships Between Leaf Pigment Content and Spectral Reflectance Across a Wide Range of Species, Leaf Structures and Developmental Stages, *Remote Sensing of Environment*, 81, 337–354.

Tucker C.J. (1979). Red and Photographic Infrared Linear Combinations for Monitoring Vegetation. *Remote Sensing of Environment,* 8, 127–150.

van der Tol C., Berry J. A. , Campbell P.K. E., Rascher U. (2014). Models of fluorescence and photosynthesis for interpreting measurements of solar-induced chlorophyll fluorescence. Journal of Geophysical Research-Biogeosciences, 119, 2312–2327.

van der Tol, C.; Verhoef, W.; Timmermans, J.; Verhoef, A.; Su, Z. (2009). An integrated model of soil–canopy spectral radiances, photosynthesis, fluorescence, temperature and energy balance. *Biogeosciences*, 6, 3109–3129.

Vilfan N, Van der Tol C, Yang P, Verhoef W. (submitted to *Remote Sens. Environ.*). A model for leaf dynamic xanthophyll reflectance.

Wong CYS & Gamon JA. (2015). Three causes of variation in the photochemical reflectance index (PRI) in evergreen conifers. *New Phytologist,* 206, 187–195.

Wu, C., Huang, W., Yang, Q., Xie, Q. (2015). Improved estimation of light use efficiency by removal of canopy structural effect from the photochemical reflectance index (PRI). *Agriculture Ecosystems & Environment*, 199, 333–338.

Young, S. J., Johnson, B. R., Hackwell, J. A. (2002). An in-scene method for atmospheric compensation of thermal hyperspectral data. *Journal of Geophysical Research: Atmospheres*, 107, ACH 14-11-ACH 14-20.

Zhu X-G, Long SP, Ort DR. (2010). Improving Photosynthetic Efficiency for Greater Yield. Annual Review of Plant Biology, 61, 235–261.

# APPENDIX: Relationship between tree height/age and fluorescence

The relationship between tree height/age was initially investigated on the Bílý Kříž dataset from 9 September 2012. The first results indicated that the non-linear relationship between fluorescence and tree age which might be separated in a juvenile and mature stage (Figure 85).
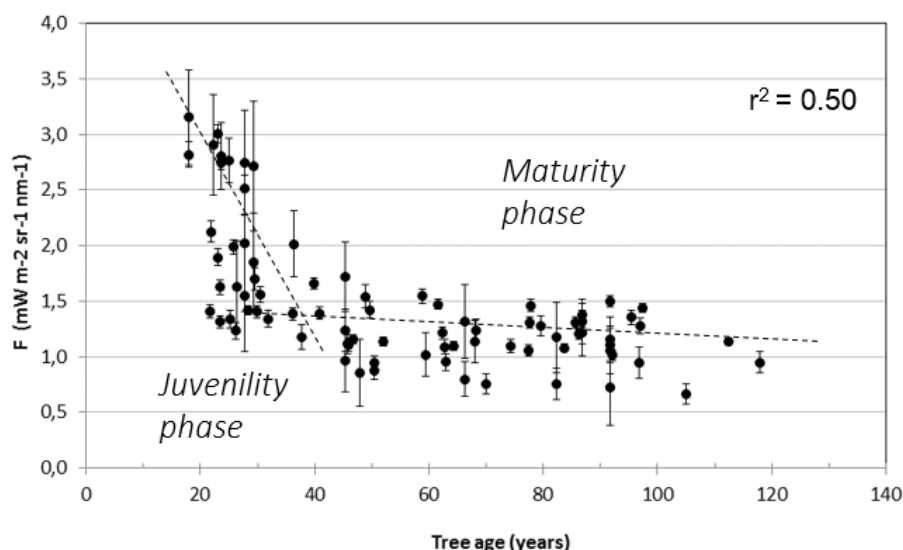


**Figure 85: Fluorescence (F) vs. tree age in years. Relationship was established on a flight line recorded on 9 September, 2012. Fluorescence was derived using the SVD method.**

It was proposed to further analyse this data with additional datasets recorded over Bílý Kříž in 2014 (see chapter 5.3 and 6.1.6). Unfortunately, the insufficient, geometric precision of the *HyPlant* data in this year (see chapter 4.1.2.4) made the investigation of the relationship between tree age and fluorescence impossible (inaccuracy in spatially registering the digital surface model and fluorescence data). The further investigation of the relationship was done on the FLEX-US dataset, even though it was not an objective in the FLEX-US study. The main results will be summarized in the following.

The further analysis of the relationship between tree age and fluorescence emission was conducted on a managed loblolly pine forest of the Parker Track forest. An overview of the data acquisition and derived fluorescence maps of the FLEX-US 2013 campaign is given in RD-8.
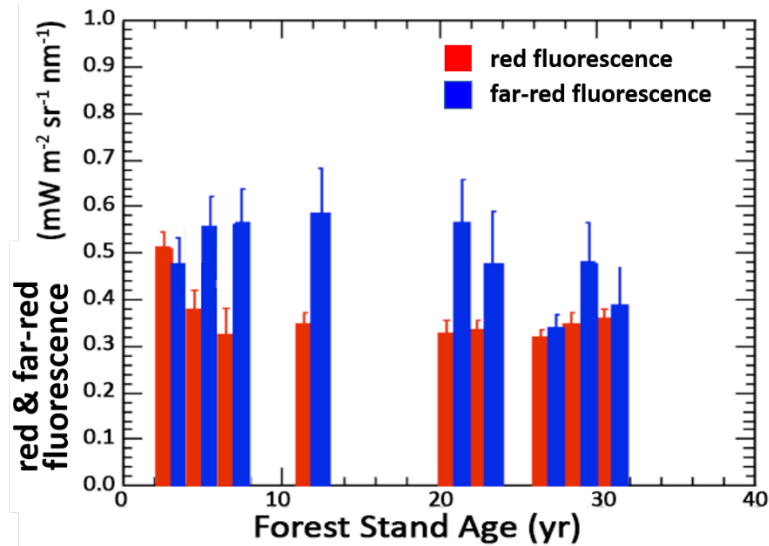
**Figure 86: The canopy height (forest stand age in years) and fluorescence information were obtained for the loblolly pine stands by age class, across the Parker Tract site: red and far-red fluorescence (mW m-2 sr-1 nm-1), derived from *HyPlant's* FLUO module vs. stand age; means and standard errors are shown for bar charts, N = 30.**

It could be shown that red fluorescence decreased with stand age, while far-red fluorescence remained almost constant (Figure 86). This decline with ageing is interpreted as an effect of age dependent photosynthetic limitation or as a decline of stomatal conductance due to hydraulic limitations and opens a promising path how fluorescence measurements can be used for forest age mapping. Further analyses will be published in Colombo *et al.* (in preparation).